Russian Chemical Reviews **75** (8) 637 – 670 (2006) © 2006 Russian Academy of Sciences and Turpion Ltd

DOI 10.1070/RC2006v075n08ABEH003623

Discreteness of nanostructures and critical dimensions of nanoclusters

I P Suzdalev, P I Suzdalev

Contents

I. Introduction 637
II. Critical dimensions of nanoclusters and nanostructures 638
III. Critical characteristics and properties of nanoclusters and nanostructures 652

Abstract. Theoretical models and experimental data related to the formulation of the discreteness concept for nanoclusters and nanostructures are analysed. The discreteness is shown to be due to the existence of critical sizes of nanoclusters determined by the magic numbers of atoms and thermodynamic parameters. Such nanoclusters exhibit the highest stability in the formation of nanostructures and specific properties. The bibliography includes 116 references.

I. Introduction

There are a few types of discreteness of matter, *e.g.*, discreteness on the atomic level, the elementary particle level and the atomic-molecular level. For instance, the atomic-molecular structure is discrete on the atomic level (of the order of 10^{-1} nm). This manifests itself in individual electronic, optical, magnetic properties of matter on this level of discreteness and in, *e.g.*, the form of X-ray diffraction, electron diffraction and in the onset of co-operative mechanical, thermal, optical, electronic and magnetic properties in the formation of condensed state. The structure and properties of matter on various levels of discreteness have been a subject of atomic physics and quantum chemistry, physics and chemistry of condensed state and physical chemistry. Discreteness of matter on a lower, elementary particle level (of the order of 10^{-6} nm) has been studied by nuclear physicists and chemists.

There is yet another level of discreteness of matter. Some features of the supramolecular structures and nanoclusters of size 1 – 100 nm also indicate the formation of the most stable clusters (nanoparticles) of particular sizes, which can be treated as manifestation of specific discreteness level.

In addition to the spatial discreteness level in heterogeneous nanostructures involving nanopores, nanotemplates, nanoclusters, *etc.*, discreteness governed by the physicochemical properties of matter emerges. On the one hand, this is a consequence of the microscopic approach and the effect of the atomic or electronic structure of matter on the formation and properties of nanoclusters of size 1 – 10 nm on going from the local energy levels to the band structure. On the other hand, the laws of thermodynamics and the effect of the surface dictate the formation of stable nanoclusters of the most probable sizes from 1 to 50 nm and thus the appearance of nanostructures with discrete nanocluster size distributions. (Of course, the case in point are the most probable cluster sizes against the background of overall continuous nanocluster size distribution in nanostructures.) Nanostructures built of the critical-size nanoclusters possess novel co-operative properties.[1–6]

The aim of this review is to elucidate the discreteness and conditions for formation of critical-size nanoclusters and to consider the properties of such nanoclusters as well as nanostructures, nanomaterials and nanodevices based on them. It should be noted that the functions characterising the state of clusters are determined by not only the cluster size, but also the presence of defects, by the electronic, magnetic and other factors which were ignored in our models.

The review consists of two main parts. The first part is devoted to the formation of critical-size nanoclusters and nanostructures based on them in various media. In the second part we will consider the properties of such nanostructures and nanomaterials.

The first part concerns the mechanisms of nanocluster formation in the gas, liquid and solid phases. The formation of critical-size nanoclusters in the gas phase is considered using the thermodynamic (pressure and temperature dependences) and microscopic (with inclusion of triatomic collisions and the effect of the magic number of atoms in filling the electron shells) approaches and the close packing principle. For the liquid phase (solutions and colloidal systems) we consider the formation of molecular clusters, colloidal clusters and critical-size nanoclusters in a nanopore or a reverse micelle based on the thermodynamic approach and the principle of close packing of atoms.

The formation of mesoporous silica and alumina is also associated with the existence of nanoparticles of characteristic discrete sizes. Solid-phase reaction studies revealed not only the formation of critical-size nanoclusters with the primary structure, but also the existence of aggregates of the critical-size clusters, namely, superclusters that form hierarchical secondary or ternary structures. Using the thermodynamic approach, it is possible to determine the critical cluster sizes corresponding to the onset of sintering and the formation of a nanostructure.

The second part is devoted to those properties of nanostructures that are due to discreteness. We will consider the thermal properties related to the existence of critical cluster sizes at which melting begins and transition to the solid – liquid state occurs. Then, we will discuss the mechanical properties. At certain critical value of the defect concentration, nanoclusters can behave as superhard of superplastic materials. These properties can be controlled by varying the cluster surface area. The conducting and optical properties of nanoclusters and nanostructures are due to

I P Suzdalev, P I Suzdalev N N Semenov Institute of Chemical Physics, Russian Academy of Sciences, ul. Kosygina 4, 119991 Moscow, Russian Federation. Fax (7-495) 137 83 18, tel. (7-495) 939 71 01, e-mail: suzdalev@chph.ras.ru (I P Suzdalev), tel. (7-495) 930 21 01 (P I Suzdalev)

Received 13 January 2006
Uspekhi Khimii **75** (8) 715 – 752 (2006); translated by A M Raevskiy

the existence of the critical cluster size for one-electron transfer and the critical sizes governed by the occurrence of a plasmon (in the case of optical absorption in metals) or a polaron (in the case of semiconductor luminescence). Laser emission is also related to the maximum and minimum sizes of semiconductor clusters. The electromagnetic properties including the giant magnetoresistance are determined by the critical size of superparamagnetic clusters, the magnetic field magnitude and the ratio of the cluster size to the mean free path of an electron (in the case of electron conduction). Tunnelling magnetisation parameters are characterised by the critical values of external magnetic field. Finally, magnetic phase transitions in clusters can be governed by the critical cluster sizes.

With allowance for specific properties of nanoclusters, nanostructures can be considered as a specific form of matter that is discrete on the cluster (or supramolecular) level.

II. Critical dimensions of nanoclusters and nanostructures

1. Critical sizes of nanoclusters in the gas phase

a. Critical cluster size and nucleation

The metal, oxide, carbon, noble gas and small-molecule (*e.g.*, water) clusters are formed by condensation in atomic beams or vapours. Clustering studies are carried out using the dynamic approach with account of triatomis collisions (in particular, the molecular dynamics or Monte Carlo methods) or the thermodynamic approach.

The formation of a cluster can take a time exceeding 10^{-13} s; the process depends mainly on the kinetic energy of the cluster; however, even the times of the order of 10^{-9} s (*i.e.*, characteristic of a single computer operation) are too short to study the whole history of cluster formation.[7] The finite size of a stable cluster can be estimated using the thermodynamic approach by minimising the changes in the Gibbs free energy depending on the size of the cluster formed upon the gas – liquid phase transition

$$n\,\mathrm{A(gas},\, P) = \mathrm{A}_n\,\mathrm{(liquid\ cluster)}.$$

In this case one has [8]

$$\Delta G = 4\pi r^2\alpha - \frac{4}{3}\pi r^3 nRT \ln\frac{P_r}{P_\infty}, \qquad (1)$$

where r is the radius of the cluster, α is the surface tension of the cluster, R is the gas constant, n is the number of atoms in the cluster, P_r is the gas pressure above the cluster surface and P_∞ is the pressure above the flat surface. Supersaturation in the system is given by the ratio

$$\Phi = \frac{P_r}{P_\infty}.$$

Clustering occurs at

$$\Phi_{\mathrm{cr}} = \frac{P_{\mathrm{cr}}}{P_\infty}.$$

The smallest critical size (a smaller cluster is unstable due to thermal fluctuations) can be determined from the equation

$$r_{\mathrm{cr}} = \frac{2\alpha m}{\rho k T \ln \Phi_{\mathrm{cr}}}, \qquad (2)$$

where m is the atomic or molecular mass, ρ is the cluster density and k is the Boltzmann constant.

The critical characteristic size (diameter) of a water cluster d_{cr} equals 1.6 nm at $\Phi = 4$, which corresponds to about 90 molecules.[8] The thermodynamic approach gives larger sizes of, *e.g.*, stable alkali metal or aluminium clusters comprising the magic numbers of atoms or noble gas clusters. The size of thermodynamically stable alkali metal clusters can be estimated from Eqn (2). With allowance for the molecular mass, density and surface tension (it is ten times higher than the surface tension for water) differences, an alkali metal cluster should be an order of magnitude larger than the water cluster and comprise thousands of atoms. However, the most stable clusters with the magic-number-determined sizes only comprise about tens of atoms (see below).

b. Critical nanocluster sizes governed by the electronic and atomic structure

Isolated (ligand-free) clusters are studied using atomic beam methods with supersonic sources. Here, atoms are produced by evaporation of substances on raising the temperature of the environment or by laser ablation from the surface of a solid. A cluster is formed due to the pressure drop and sharp cooling of the environment. Clusters are separated by sizes (masses) in, *e.g.*, time-of-flight mass spectrometers.

Alkali metal nanoclusters. The alkali metal clusters have a simple electronic structure, namely, each atom has one s-electron in addition to the filled electron shells. Such s^1-clusters are formed in atomic and molecular beams in high vacuum. They are ligand-free, being convenient objects for studying the electronic properties of nanoscale structures (size 1 – 2 nm). As for molecules, here the key measurable and interpretable parameters are the ionisation energy, electron affinity, dissociation energy and optical absorption of clusters. By studying these characteristics it is possible to construct models for description of the cluster properties.

Ionisation of s^1*-clusters*. The ionisation energy (or potential), E_{i}, of a cluster is minimum in the following process

$$\mathrm{X}_n + h\nu \longrightarrow \mathrm{X}_n^+ + \mathrm{e}^-. \qquad (3)$$

The E_{i} value is determined by varying the energy of a laser or some other ionisation source. The formation of charged clusters of particular sizes can be detected using mass spectrometers. The ionisation potential decreases with an increase in the cluster size.[9] This correlation can be explained using the classical model of a metal drop and the metallic shell (quantum) model. The latter model gives the magic numbers of the metal atoms that form clusters characterised by the higher ionisation potentials and stability.

The classical model correctly predicts the trends in the change in the cluster size, but it seems to be inaccurate in the case of small clusters for which the quantum size effects were established. Here, the shell model is more appropriate, which considers the motion of an s^1-electron in the effective potential produced by other electrons and ions in the cluster.

In the shell model, which is also called the 'jellium model', the cluster-forming ions produce an averaged positive background for the motion of an electron. The shell model for a cluster is constructed similarly to the shell model for an atom. Solving the one-electron Schrödinger equation in the potential field gives the energy levels (eigenvalues of the electron energy). As a result, the energy levels of the clusters with one free electron should be characterised by the principal quantum number N, the number of radial wave functions $(N-1)$ and the angular momentum l with a degeneration degree of $2(2l+1)$. This model [10,11] predicts the closed-shell electronic structure for 1s-, 1p-, 1d-, 2s-, 1f-, 2p-, 1g-, *etc*., clusters comprising $n = 2(2l+1) = 2, 8, 18, 20, 34, 40, 58$, *etc*., atoms (or having the same numbers of free electrons). These numbers are called the magic numbers.

Ionisation energy measurements for clusters of various sizes provide a method of direct investigation of the cluster shell structure; the filled electron shells should correspond to the highest stability and ionisation energy.

The ionisation energies of potassium, sodium and silver clusters of various size are presented in Fig. 1. The E_{i} show clearly seen oscillations for the even (higher E_{i} values) and odd (lower E_{i} values) atom numbers in the clusters and maxima at $n = 8$ and 20, which confirms the shell structure of these clusters. The shell structure is most pronounced for silver clusters due to strong electron coupling and, correspondingly, higher potential for the

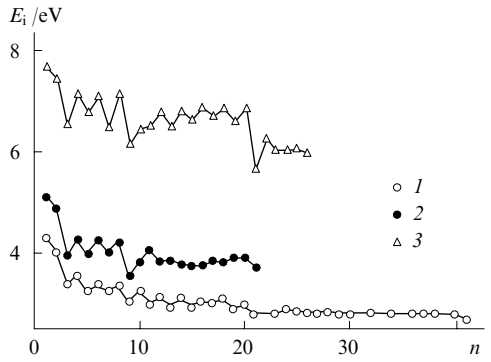


Figure 1. Ionisation energies of potassium (*1*), sodium (*2*) and silver (*3*) nanoclusters.[9]

motion of electrons (deeper potential well), which leads to greater separation of the energy levels.

Fragmentation of s^1*-clusters*. Once excited by, *e.g.*, laser radiation, clusters can undergo fragmentation into either isolated atoms or smaller clusters by the evaporation or fission mechanisms (similarly to transformations in atomic nucleus); in this case, the drop model is applicable. Additionally, the cluster dissociation can proceed by the monomolecular mechanism or be accompanied by cascade transformations. The stability of a cluster composed of n atoms is governed by the redistribution of the energy absorbed over a total of $(3n-6)$ vibrational degrees of freedom followed by fixation of a particular cluster breakdown channel and the excited-state lifetimes. The results of cluster stability studies using both the metallic drop model and the shell model indicate a common trend, namely, an increase in the binding energy with an increase in the cluster size.

Monomolecular dissociation studies of singly charged clusters also revealed discrete magic numbers of the atoms in the cluster. For instance, the dissociation energy decreases for the Na_n^+ and K_n^+ clusters comprising $n = 9$ and 21 atoms, which corresponds to 8 and 20 electrons in the filled electron shells, respectively. Clusters containing an even number of electrons are highly stable, which is indicative of electron pairing effects. These effects are more characteristic of Na_n^+ rather than K_n^+, because for sodium the potential well in the electron field is deeper than for potassium and, hence, the energy differences between the sodium energy levels are larger (greater level – level separation).

Monomolecular dissociation of doubly charged cluster ions is a more complex process compared to the dissociation of singly charged nanoclusters, because it includes not only evaporation, but also fission of clusters. Two possible dissociation mechanisms involve retention of two charges on one fragment

$$X_n^{++} \longrightarrow X_{n-p}^{++} + X_p ,$$

or acquisition of one charge on each fragment

$$X_n^{++} \longrightarrow X_{n-q}^{+} + X_q^{+} . \qquad (4)$$

If one cluster fragment remains doubly charged, the potential energy surface has no potential barrier. If both fragments become charged, repulsion between them produces a Coulomb barrier. The fragments are separated upon formation of a transition state. This process is often called the Coulomb fission.

Signals of small doubly charged clusters X_n^{++} are often indistinguishable in the mass spectra; signals of the critical-size clusters (n_C) suitable for Coulomb fission are observed.[12] Usually, it is assumed that small doubly charged clusters of size less than n_C are unstable because the repulsive energy of the positively charged fragments exceeds the binding energy in the cluster. Therefore, the critical cluster size is governed by the dynamics of monomolecular dissociation. In the case of large neutral clusters ($n > 30$), evaporation dominates the Coulomb fission. For clusters of intermediate sizes ($26 < n < 30$), evaporation and fission 'coexist'. This points that the height of the Coulomb barrier approximately equals the binding energy. For small clusters ($n < 24$) the Coulomb barrier becomes higher than the binding energy and the doubly charged clusters can no longer exist. The critical sizes of the doubly charged clusters of the first-row elements are as follow:[9]

Element	Na	K	Cs	Au	Ag
n_C	24	17	19	3	5

Aluminium clusters. Aluminium clusters are of interest as models with free electron gas that consists of s^2- and p^1-electrons and provides a metallic type of conductivity. Aluminium is widely used as structural material; this makes corresponding reactivity studies topical. Similarly to the alkali metal clusters, the state of aluminium clusters is characterised by the ionisation energy, dissociation energy, polarisation and reactivity that is determined in the reactions with other molecules. Answering the question of applicability of the electron shell model ('jellium model') to aluminium clusters requires analysis of all these characteristics.

Ionisation energy of aluminium clusters. Figure 2 presents the results of ionisation energy calculations for Al_n (n from 2 to 70) clusters from the following equation

$$E_i(r,z) = E_{i\infty} + \left(z + \frac{3}{8}\right)\frac{e^2}{r} , \qquad (5)$$

where $E_i(r,z)$ and $E_{i\infty}$ are the ionisation energies of the cluster of radius r and charge z and the flat metallic surface, respectively, and e is the electron charge. The open circles denote experimental data and the dashed line shows the prediction of the metallic spherical drop model.

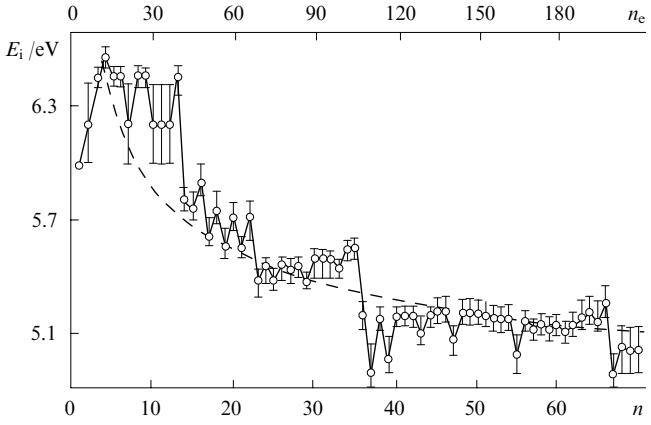


Figure 2. Ionisation energies of Al_n clusters obtained after photoionisation.[13]

The clusters with $n = 7, 14, 23, 36$ and 67 are characterised by abrupt changes in E_i. According to the electron shell model, closed shells are formed at the electron numbers equal to 20, 40, 58, 70, 92, 138 and 198. A decrease in E_i should be expected for the clusters with one or two extra electrons (in addition to the filled shell), *i.e.*, at the electron numbers 21, 42, *etc*. Taking account of the fact that the aluminium atom has s^2p^1 valence electrons leads to agreement between the experimental data and the predictions of the shell model, because the number of free electrons for aluminium clusters is $3n$. However, no agreement is obtained for larger clusters ($n > 20$).

Yet another feature of aluminium clusters compared to the alkali metal clusters consists in considerable deviation of the calculated ionisation energy (work function of an electron in a metallic sphere) from the experimental values for small clusters

(see Fig. 2). This can be explained by different effect of the conduction band in the alkali metal and aluminium clusters with an increase in the cluster size. The ionisation energies of alkali metal clusters with half-filled s-bands decrease as the cluster size increases. For the s^2p^1-clusters, the p-band top initially decreases with an increase in the cluster size (ionisation energy increases) and then increases similarly to the situation for the alkali metal clusters. Agreement with the predictions of the classical drop model approximately begins with a 25-atom cluster.

Dissociation of aluminium clusters. Aluminium clusters mainly dissociate by evaporation rather than fission, namely, monomolecular dissociation with evaporation of aluminium atoms or ions occurs. In this case one can expect an increase in the binding energy per atom with an increase in the cluster size.

A dissociation study [14] showed that the Al_n clusters with $n = 7$ and 14 are more stable than clusters with neighbouring n values. The mass spectra exhibit clearly seen signals of the stable clusters Al_7^+ and Al_{14}^+. The magic numbers $n = 7$ and 14 differ from those found for the alkali metal clusters, but agree with the shell model. Indeed, depending on the type of the potential for the motion of electrons, at $n = 8$, 18, 20, 34, 40, 58, 68 and 92 the set of closed shells includes 1p, 1d, 2s, 1f, 2p, 1g, 2d and 3s for the 'rectangular well' potential or $n = 8$, 20, 40, 70 for the harmonic oscillator potential. The aluminium atom has a valence of three and therefore the Al_7^+ cluster has twenty valence electrons, namely, $7 \times 3 - 1$ (with allowance for the cluster charge). This gives the first magic number, 7. Analogously, the closed shell of Al_{14}^+ cluster has forty-one valence electrons. Of course, the aluminium cluster has a more complex configuration compared to alkali metals because the interaction of the s- and p-valence electrons occurs.

The electron shell scheme also describes the oxidised aluminium clusters with O=O or O=Al bonds that reduce the number of valence electrons in the cluster by two. For instance, the cluster $Al_{15}O_2^+$ is more stable than other oxidised aluminium clusters. Here, the number of valence electrons in the closed electron shell is $3 \times 15 - 1$ (with allowance for the cluster charge) $- 4$ (two electrons per oxygen atom) = 40. The dissociation energy increases as the cluster size increases

Reactivity of aluminium clusters. The interaction of aluminium clusters with hydrogen or oxygen molecules is an important cluster characteristic. Studies of these reactions can be useful in order to relate the shape of a cluster to its reactivity. The majority of experimental data point that the activation barriers to the reactions involving clusters are higher than the corresponding parameters for bulk material.[14]

Now we will consider the best studied reactions of aluminium clusters with oxygen as examples. Reactions of neutral clusters result in Al_nO_2. Aluminium atoms or dimers react rapidly; the reactivity initially decreases with an increase in the cluster size and then increases. Reactions of positively charged clusters comprised of at most seven Al_2O^+ particles with oxygen produce Al_nO^+ cations as the major product. Possible reactions of larger clusters are shown below:

$$Al_n^+ + O_2 \longrightarrow Al_{n-4}^+ + 2\,Al_2O, \tag{6}$$

$$Al_n^+ + O_2 \longrightarrow Al_{n-5}^+ + 2\,Al_2O + Al. \tag{7}$$

Here, the activation barriers are of the order of a few tenths of an electronvolt at $n = 3-25$.

Bulk aluminium is readily (almost barrierlessly) oxidised, *i.e.*, clusters are less reactive than bulk material. Reactions of negatively charged clusters with an excess of oxygen lead to stable products in the form of 13-, 23- and 37-atom clusters. This indicates that the shell structure of clusters affects their reactivities, namely, Al_{13}^-, Al_{23}^- and Al_{37}^- have 40, 70 and 112 valence electrons respectively that form closed electron shells in the harmonic oscillator potential. The shape of a cluster is also related to its reactivity. For instance, calculations of Al_7^+ cluster predict a distorted octahedral configuration in which all atoms are equidistant from the centre of mass in such a fashion that they seemingly are on the surface of a sphere. This cluster is characterised by a closed spherical electron shell with 20 valence electrons. The next closed-shell structure is an icosahedral cluster Al_{13}^-. A feature of this stable structure is a large energy difference between the filled and unfilled orbitals, which ensures a low reactivity of this system.

Mercury clusters. Mercury clusters provide a unique possibility of studying an insulator–conductor transition. The mercury atom has a closed electron shell ($[Xe]4f^{14}5d^{10}6s^2$) and can be considered as a building block for forming the van der Waals bonds. At the same time, bulk mercury is a metal. Transition from the van der Waals to the metal bonds is accompanied by an increase in the cluster size and in the latter case the metal atom has a $[Xe]4f^{14}5d^{10}6s^{1.4}6p^{0.6}$ configuration.

Similarly to alkali metals, silver and aluminium, the ionisation energy serves the key indicator of the properties of mercury. In Fig. 3 the results of ionisation energy measurements for Hg_n clusters (n from 1 to 43) are plotted *vs.* $1/r$.

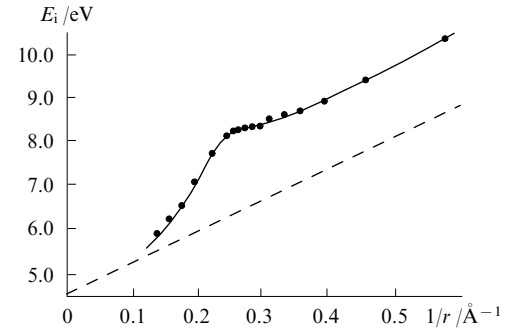


Figure 3. Ionisation energies of clusters Hg_n plotted *vs.* inverse cluster radius.[15]
Dashed line corresponds to the relation for bulk material $[E_i(n \to \infty) \approx \varphi + (e^2/r)]$.

Mercury clusters with $n \leqslant 13$ are characterised by a decrease in E_i with increasing the cluster size. But in this case the E_i energies are appreciably different from the values predicted by the spherical metallic drop model. Moreover, extrapolation of the ionisation energy to $n \to \infty$ gives a value of 6.5 eV, which much exceeds the work function of an electron in bulk material (4.49 eV). At $n > 13$, the $E_{i\,n}$ sharply decreases and the experimental data approach the results obtained by the spherical metallic drop model.

The ionisation energy was determined from the results of Hartree–Fock MO energy calculations,[16]

$$E_{i\,n} = E_n(v_t - 1) - E_n(v_t), \tag{8}$$

where $E_n(v_t)$ is the total electronic energy of an n-atom cluster with v_t valence electrons. It was found that

$$E_{i\,n} = -\varepsilon_{HOS}(n) + \frac{e^2}{2r}, \tag{9}$$

where $\varepsilon_{HOS}(n)$ is the energy of the highest occupied shell. The existence of a critical cluster size (n_c) is assumed, *e.g.*, $n_c = 13$; at $n < 13$, the electron is localised on the atom, whereas at $n_c > 13$, it is delocalised. Thus, an increase in the cluster size is accompanied by an abrupt transition from insulator to conductor. The first term in Eqn (9) describes the changes in the ionisation energy due to the changes in the electronic structure for different cluster sizes and the second term describes the electrostatic contribution after shift of the energy levels upon ionisation $v_t \to (v_t - 1)$. At $n < n_c$, the atom emits electrons (Fig. 4) and thus the energy of the highest occupied level approaches the energy of the atom, whereas at $n > n_c$ electrons are delocalised and the $\varepsilon_{HOS}(n)$ value should be treated as the energy of the highest occupied MO (HOMO).[16]

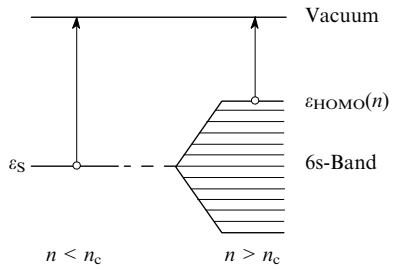


Figure 4. Scheme describing ionisation for localised ($n < n_c$) and delocalised $n > n_c$ electronic states of Hg_n clusters.

Carbon clusters. A distinctive feature of carbon clusters consists in strong atom–atom interactions. Clustering of carbon atoms occurs much easier compared to all other elements, which is substantiated by, *e.g.*, the formation of carbon black in thermolysis of any carbon-containing structures. Carbon is one of the most abundant elements in the Universe (it ranks fourth after hydrogen, helium and oxygen). Additionally, this is the first stable element produced by thermonuclear fusion. Red giant stars emit a huge amount of carbon to interstellar space, and interstellar dust probably consists of carbon clusters. The clusters in question are also of interest as objects for basic research. In laboratories, they are produced by laser vaporisation or arc evaporation of carbon followed by mass separation using mass spectrometers. The mass spectrum obtained has a bimodal character, namely, one mode corresponds to small clusters (number of atoms $n < 24$) and the other mode ($n > 24$) corresponds to fullerenes.

Small carbon clusters. The mass spectra of small carbon clusters show a period of four carbon atoms, which manifests itself in the even–odd oscillations of the line intensities of the clusters synthesised.[17–20] The magic numbers of the carbon atoms can be readily determined from the spectra (C_n, n = 7, 15, 19 and 23). Such mass spectra are obtained after ionisation of the neutral clusters synthesised by the laser vaporisation method by exposure to UV light. Photoinduced fragmentation studies showed that the process mainly results in neutral clusters C_3. Larger particles can undergo fragmentation into C_5 clusters.

According to quantum-chemical calculations, neutral carbon clusters should have a chain structure up to nine atoms long, which then transforms into a ring. Taking into account the fact that a covalently bonded cluster tends to reduce the number of free bonds, the cluster shape is governed by the following factors: an increase in the number of carbon–carbon bonds in the cluster (although each succeeding bond is weaker then the preceding one), a change in the number of free bonds and production of strain upon formation of the ring-type structure. The C_3 cluster is considered linear.[21] The formation of a carbon ring structure is accompanied by disappearance of free carbon bonds and production of additional strain in the cluster.

Ring-type structures are characteristic of larger clusters. The chain-to-ring transition should occur at n = 10; the even-numbered clusters tend to form rings at low temperatures.[22]

The predicted (calculated) stabilities of particular forms of carbon clusters and transitions from chain to ring-type structures were also observed in the experiments involving the photoelectron spectra of negatively charged clusters.[23]

Signals of C_3 clusters were detected in the optical spectra of comets. The signals of C_3 and C_5 clusters were observed in the spectra of interstellar space in the vicinity of some stars; vibrational spectroscopy data confirm the chain structure of the clusters.

The shapes of larger carbon clusters are calculated based on a certain quantum-mechanical model, *e.g.*, the Hartree–Fock model or the density of states approximation.[24] According to calculations, three isomers of C_{20} cluster can exist, namely, a ring-type, a bowl-shaped and a fullerene-like structure (Fig. 5).

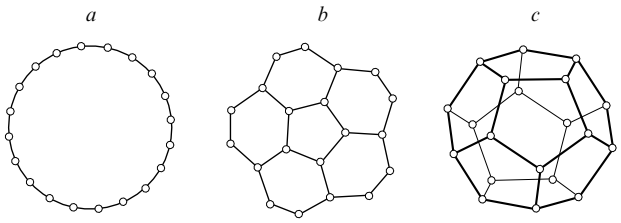


Figure 5. Ring-type (*a*), bowl-shaped (*b*) and fullerene-like (*c*) isomers of C_{20}.

In principle, the smallest fullerene is a dodecahedron comprising twenty carbon atoms that form twelve pentagonal faces. The laser ablation experiments result only in ring-type clusters. Besides, calculations predict the existence of a bowl-shaped cluster with a graphite-like structure and a minimum number of free bonds. Yet another stable structure is a tetrahedral structure C_{28}. According to calculations, the C_{28} cluster behaves as a superatom with an efective valence of four and high reactivity to both encapsulation of metal atoms and *exo*-attachment of other atoms. Experiments with this cluster revealed the possibility of encapsulating an uranium atom; this structure is denoted by $U@C_{28}$.[24] Additionally, the scandium, titanium, zirconium, and hafnium atoms can be encapsulated inside the C_{28}. The existence of exohedral polymers of the $C_{28}H_4$ type was predicted.[25]

Fullerenes. The first representatives of large carbon clusters, namely, fullerenes were discovered by Kroto, Smalley and Curl in 1985. Investigations were initiated by Kroto who used laser vaporisation and mass spectroscopy for production and study of small carbon clusters. He paid attention to a single spectral peak, which appeared under particular conditions for production of carbon clusters. This peak corresponded to the C_{60} cluster, which was called fullerene.[26, 27]

In the structure of C_{60} (Fig. 6), pentagons are embedded into hexagonal graphite sheets for which sp^2-hybridisation is allowed. As a result, a hollow structure is formed, which has no free bonds and is stabilised through π-bonds. Equivalence of all atoms, unstrained character and the possibility of isolating all pentagons make the 5/6-ring structure of the C_{60} cluster unique. The next (in size) stable fullerene is C_{70}.

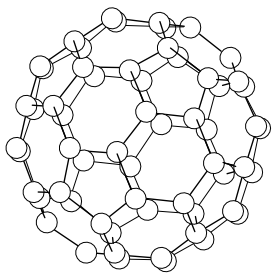


Figure 6. Structure of C_{60} cluster.

Formation of fullerenes. The first question that should be answered is as to how stable ordered structures are formed under high-temperature laser vaporisation and chaotic plasma conditions? Probably, graphite species removed by laser form hollow structures, but it is also not impossible that the fullerene formation mechanism is similar to the mechanism of carbon black formation. The kinetic models for growth of clusters from carbon atoms and cluster radicals present in plasma were elaborated.[28]

The most energetically favourable shape of small cluster radicals is a linear chain. Such chains interact with one another, grow in plasma up to 20–30 atoms long and then undergo

spontaneous transformations to polycyclic aromatic rings or graphite sheets. These structures are preferred because the average coordination number of the carbon atom increases, but they also contain numerous free bonds. It is the decrease in the number of free bonds that makes the growth of such structures energetically favourable. If the density of carbon atoms is high, clusters will have reactive termini whose curvature is appropriate the most energetically favourable arrangement of transient states including matching of the edges of rolled sheets and formation of fullerenes of size up to the size of macroscopic carbon black particles. Such a random plasma process also permits formation of larger fullerenes, *e.g.*, C_{180}, C_{240} or C_{540}, which can theoretically be stable.

Effective studies of the structure and properties of C_{60} and heavier fullerenes became possible after the elaboration and improvement of the method for production of sufficient amounts of fullerenes by Kratschmer *et al.*[29] An arc discharge using graphite electrodes in helium atmosphere produces carbon black, which is then dissolved in benzene or toluene. Crystallisation of the solution gives gramme amounts of C_{60}/C_{70} mixture in a 3 : 1 ratio and heavier fullerenes (2%).[30]

Fagmentation of fullerenes. As mentioned above, fragmentation of small carbon clusters involves detachment of C_3 clusters. Fragmentation of fullerenes occurs by detachment of C_2 fragments owing to stability of the even-numbered clusters.[31, 32]

Based on the kinetic energies of products, the following estimates of the binding energy of C_2 with C_{58}^+, C_{60}^+ and C_{62}^+ were obtained: 4.6 eV for C_{58}^+, C_{60}^+ and only 3 eV for C_{62}^+ (see Ref. 33).

The C_n^+ shell comprising five-membered rings loses a C_2 unit and transforms to the C_{n-2} shell. The fused five-membered rings transform to six-membered ones and two six-membered rings above and below these five-membered rings transform to five-membered rings. As a result, the total number of five-membered rings remains unchanged, as required for a closed shell upon the loss of a six-membered ring. This mechanism implies a fast surface reorganisation in order to join two five-membered rings.

The ionisation energies and the electron affinity energies of fullerenes (starting with C_{60}) do not show large-amplitude oscillations as in the case of metal clusters. This is probably due to rather large sizes of the former ($n = 60$).[34]

Generally, the experimental data are in agreement with the spherical metal model, that is, an increase in the fullerene size causes a decrease in the ionisation energies and an increase in the electron affinity energies (E_A) that approach the calculated value of 5.37 eV. The average electronegativity $(E_i + E_A)/2 = 5.2 \pm 0.2$ eV obtained from experimental data agrees with the results of calculations. The slopes of the plots of E_i and E_A *vs.* cluster size decrease on going to heavier fullerenes. One should expect deviations from the spherical drop model for those fullerenes (especially, heavy ones) whose shape differs from a sphere.

Taking account of symmetrical closed structure of fullerenes, an impression may be formed of these compounds as low-reactive species. However, this is not the case. Fullerenes react with, *e.g.*, metals and fluorine to form a variety of derivatives that can be classified into different structural types. These are endohedral fullerenes containing one or a few metal atoms inside the fullerene cage, exohedral fullerenes with functional groups attached from the outside of the fullerene cage and substitution fullerenes in which one or several carbon atoms of the fullerene cage are replaced by some metal atom(s).[6]

Noble gas clusters. Noble gas atoms have spherically symmetric electron shells. This is the reason for specific properties of the noble gas clusters. Here, clustering is due to the van der Waals forces that are responsible for the formation of molecular crystals at low temperatures (except helium atoms).

The interaction between two noble gas atoms separated by a distance R can be described by the Lennard-Jones potential

$$V_{LJ}(R) = \varepsilon\left[\left(\frac{R}{R_0}\right)^{-12} - 2\left(\frac{R}{R_0}\right)^{-6}\right], \qquad (10)$$

where ε is the depth of the potential well in the field in which atoms move, with a minimum at the distance R_0. This interaction can be treated as a contact of soft, weakly attracting spheres. The first term in Eqn (10) corresponds to repulsion between the filled orbitals and can be described by the Morse exponential potential. The second term corresponds to attraction of induced dipoles. The first excited electron state lies between 10 (for Xe) and 20 eV (for He); therefore, crystals formed from noble gas atoms are colourless and transparent.

The ground state of neutral noble gas clusters was simulated using the potential of pair interactions.[35]

Figure 7 presents the most stable configurations of clusters of various size obtained from calculations. The cluster structures correspond to an isosceles triangle ($n = 3$), a tetrahedron ($n = 4$) and a trigonal bipyramid ($n = 5$). At $n = 7$, five-fold (pentagonal) symmetry arises, which is not observed for infinite crystal lattices. The most stable icosahedral structures begin with $n = 13$. Further increase in the cluster size leads to stable structures with $n = 55$, 147, 309, 561, ... The number of the nearest neighbours of an atom in icosahedron is larger than for all other crystal lattice symmetries. This is the reason for enhanced stability of icosahedral structures. Thus, the noble gas clusters obey the principle of close packing of atoms. As a consequence, the most stable clusters are formed and the magic numbers of atoms arise, namely, $n = 13$, 55, 147, 561, ...

Transition metal clusters. In contrast to the clusters considered above, transition metal clusters have a more complex electronic structure because it is formed by d- or f-electrons. The stability and reactivity of such clusters are governed by two series of magic numbers. One of them is related to the electron shell (as for alkali metal clusters) and the other is associated with the geometric factor (close packing), as for the noble gas clusters. Additionally, the ability of atoms to be in different oxidation states is of

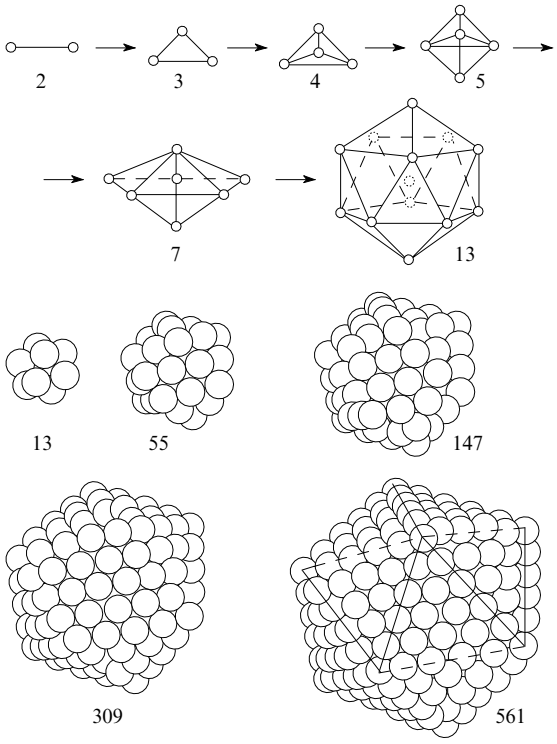


Figure 7. Model structures of noble gas clusters of different sizes. Shown are the numbers of atoms in the structures.

particular value for the transition metals clusters. This factor is responsible for large deviations of the cluster structure from the shell model and difficulties in prediction of the critical sizes of stable clusters using the microscopic approach.

2. Critical sizes of liquid-phase clusters

The formation of liquid-phase nanoclusters (from liquid phase, solutions or melts) can be considered using the thermodynamic or microscopic approach. Both approachs give the critical nucleation and stabilisation sizes for clusters with sizes of a few nanometres. Additionally, by applying the microscopic approach in studies of clustering from solutions and cluster stabilisation by ligands, it is possible to find the most stable clusters comprising the magic numbers of atoms that manifest themselves to the greatest extent in the formation of molecular clusters.

a. Thermodynamics of cluster nucleation

Clusters nucleated from the liquid phase (in, *e.g.*, formation of micellar colloids) have a minimum critical size that is determined by the reagent concentrations, presence of stabilising ligands, surfactants, *etc*. In contrast to nucleation in an infinite volume, cluster nucleation in the closed volume of a nanopore or reverse micelle (see, *e.g.*, Ref. 36) leads to formation of clusters of minimum and maximum critical sizes. Such processes proceed faster than in the macroscopic space and the cluster size is controlled by the size of the closed volume. The minimum size of a nanocluster formed in a closed pore as a result of nucleation from solution or melt can be determined from the equation

$$n_{\min} = \frac{32\alpha^3}{3\rho^2\Delta\mu^3}, \tag{11}$$

where α is the density of the surface energy of the cluster, ρ is the density of the cluster and $\Delta\mu$ is the change in the chemical potential in the cluster formation. The maximum size can be determined from the relation

$$n_{\max} \approx \frac{n_0\Delta\mu}{2+\Delta\mu}, \tag{12}$$

where n_0 is the number of atoms in the nanopore, involved in clustering (*i.e.*, the nanocluster size should increase with an increase in the nanopore size). At the same time the minimum critical size of a nucleus in the pore is governed by the thermodynamics of nucleation and by the initial concentration of the cluster-forming atoms in the pore space. As the pore size increases, a number of smaller clusters are formed. The rate of nucleation in the nanopore increases owing to a decrease in the potential barrier to nucleation (ΔG) caused by the effect of the pore wall (heterogeneity factor $K < 1$)

$$\Delta G = \frac{16\pi\alpha^3 K}{3\rho^2\Delta\mu^2}. \tag{13}$$

Thus, isolated nanoclusters of the critical sizes from one to a few nanometres [36] depending on the nanopore size and initial reagent concentration can form in porous materials with pore sizes of up to 10 nm.

b. Colloidal clusters and nanosystems

Colloidal nanosystems comprise metal and metal oxide sols, conventional and reverse micelles, microemulsions, nanoclusters in micelles and colloidal crystals.

Sols and sol formation. Metal sols are prepared in solutions after reduction reactions. In 1857 (see Ref. 37), Faraday obtained a red gold sol with cluster sizes from 2 to 50 nm by the reaction

$$AuCl_3 + 3\,H_2O + P \longrightarrow Au + P(OH)_3 + 3\,HCl. \tag{14}$$

Later on, Zsigmondy (see Ref. 37) synthesised monodisperse gold sols with variable cluster sizes by reducing gold salts with hydrogen peroxide and formaldehyde

$$2\,HAuCl_4 + 3\,H_2O_2 \longrightarrow 2\,Au + 8\,HCl + 3\,O_2, \tag{15}$$

$$2\,HAuCl_4 + 3\,HCHO + 11\,KOH \longrightarrow \longrightarrow 2\,Au + 3\,HCOOK + 8\,KCl + 8\,H_2O. \tag{16}$$

The reduction involves two stages, (i) nucleation and (ii) growth of the new phase. By controlling the second stage it is possible to form a yellow (size 20 nm), red (40 nm) and blue (100 nm) gold sols.

Oxide sols are formed in the condensation reactions. An example is provided by the widely used hydrolysis of inorganic metal salts

$$FeCl_3 + 3\,H_2O \rightleftharpoons Fe(OH)_3 + 3\,HCl. \tag{17}$$

Such sols can exist in the liquid phase for long without precipitation or coagulation due to involvement in Brownian motion of molecules in the solution, weak cluster–cluster interactions, charge repulsion and passivation of the surface. The size of sols formed is determined by the reaction conditions, the nature of the solvent and stabiliser, reaction duration and temperature and to a great extent by the supersaturation of solutions.[37, 38]

The formation of nanoclusters is related to nucleation (homogeneous or heterogeneous) from solution. An increase in the nanocluster sizes to the maximum critical values [see Eqns (11) and (12)] and the prevention of coagulation are controlled by the surface tension that can be varied by passivating the surface. The range of possible passivators includes thiols, triphenylphosphine and its derivatives, phenanthroline, *etc*., and various surfactants. In particular, the gold nanoclusters in the sol, prepared by reactions (14)–(16) and passivated by alkanethiols represented metal nanoclusters coated with a dense thiol monolayer. The monolayer self-assembles, which is accompanied by a change in the alkyl chain length in alkanethiols and in the thiol/metal ratio and affects the size of the metal nanocluster.

Colloidal gold clusters thus formed are octahedral or icosahedral single crystals with the face-centered cubic lattice.[39] This substantiates the fact that the formation and stabilisation of nanoclusters of the critical sizes obey the close packing principle (similarly to noble gases and molecular clusters). Silver, palladium and platinum sols were also obtained.

Drying silicon hydroxide sols and metal hydroxides or alkoholates causes the formation of gel structures, *e.g.*, the known silica gel $n\,SiO_2 \cdot m\,H_2O$ or alkoxides $Zr(OPr^i)_4$, $Ti(OBu^i)_4$, $Al(OPr^i)_3$. The sol–gel technique is employed for the preparation of nanomaterials and nanoceramics used in optical, electronic and magnetic devices and for the synthesis of catalysts. Gels are then used as matrices for preparation of nanomaterials, *e.g.*, catalysts coated with metal oxide clusters.

Micelles. Micelles are formed using surfactants that can adsorb on the interface thus reducing the interfacial tension. A surfactant molecule consists of a hydrophobic part and a polar group. The hydrophobic part includes hydrocarbon radicals C_nH_{2n+1}, C_nH_{2n-1}, $C_nH_{2n+1}C_6H_4$, *etc*., containing at least eight carbon atoms. Depending on the nature of the hydrophilic group, surfactants are classified into cationic (containing primary, secondary, tertiary amines and quaternary ammonium bases), anionic (containing carboxyl, sulfoester, sulfonic acid groups, *etc*.) and non-ionogenic. The action of surfactants in aqueous solutions is based on structuring of the water molecules surrounding the nonpolar hydrocarbon radicals of the surfactants, which should cause a decrease in the entropy of the system. Since any system tends to a maximum entropy, at a certain critical micelle concentration (CMC) the water molecules and surfactant ions form associates that are called micelles (according to McBen's definition [37]). Thus, micelles are also characterised by a critical size governed by the structuring of water and the surface tension.

Micelle formation causes a portion of structured water to release; this is accompanied by an increase in the entropy and a decrease in the free energy of the system. The presence of micelles in solution can be determined from the dependences of the surface tension, conductivity, density, viscosity, light scattering and other characteristics on the surfactant concentration. The CMC value

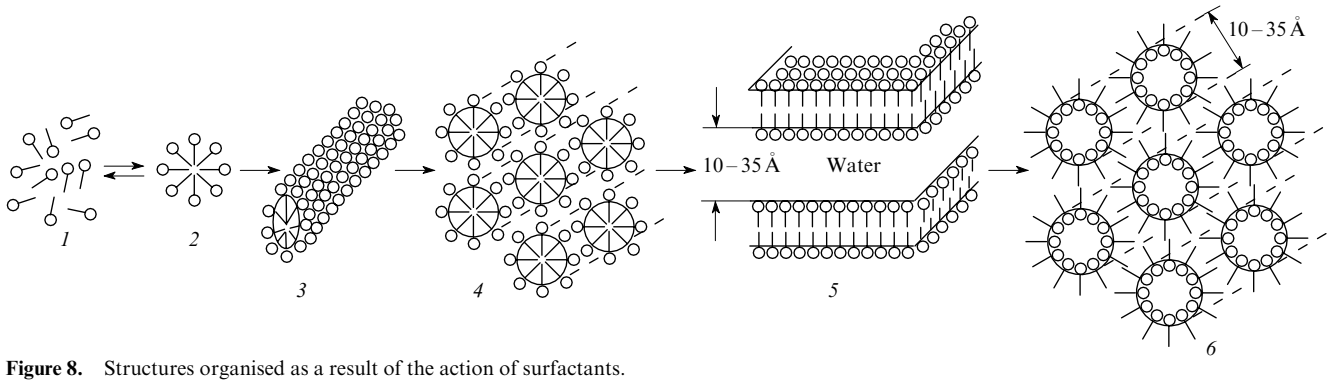


Figure 8. Structures organised as a result of the action of surfactants.
Surfactant monomers (*1*), micelle (*2*), cylindrical micelle (*3*), hexagonally packed cylindrical micelles (*4*), lamellar micelle (*5*) and hexagonally packed reverse micelles containing water molecules (*6*).

depends on the nature of the surfactant, the length of the hydrocarbon radical, the electrolyte and the pH value of the solution. The longer the hydrocarbon radical and the lower the polarity of the polar group the lower the CMC.

At the surfactant concentrations close to CMC, micelles represent spherical particles in which the polar groups contact water and the hydrophobic radicals form a nonpolar nucleus inside the micelles. There are various types of micelles, such as spherical, cylindrical, hexagonally packed and lamellar ones (Fig. 8).

Thus, micellar systems can exist in the form of one-, two- and three-dimensional nanostructures comprising tens to hundreds of molecules.

The molecules of the same surfactant can form different types of micelles in polar (*e.g.*, water) and in nonpolar solvents. Here, micelle formation at the surfactant concentrations higher than the CMC is due to the interaction between the polar groups of the surfactant. Hydrophobic (fatty) fragments of the surfactant molecules are directed outside the micelle and the polar groups are inside. As a result, a nanoreservoir is formed within the micelle, which can be filled with, *e.g.*, water. Such micelles are termed reverse micelles (see Fig. 8). Conventional and reverse micelles can be treated as oil nanodroplets in water and water nanodroplets in oil, respectively.

A valuable property of micelles is the ability to solubilise (*i.e.*, considerably enhance the solubility) hydrocarbons in aqueous micellar solutions or in solutions of reverse micelles in polar liquids. Solubilisation causes the formation of stable isotropic systems called microemulsions. The properties of substances significantly change upon solubilisation in micelles; as a consequence, the rates of chemical reactions also change. This phenomenon is called micellar catalysis. It is widely used in chemistry, biology, medicine and various technological processes.

The properties of microemulsions are to a great extent determined by the size and shape of the components of the dispersed phase and by the properties of the interfacial adsorption layers formed by the surfactant molecules. Microemulsions are characterised by high mobility and large interface surface area and can serve a medium for carrying out many chemical syntheses, *e.g.*, the syntheses of metal, oxide and metal chalcogenide nanoclusters.

Clusterisation in microemulsions. In a microemulsion system the dispersed droplets constantly collide, coalesce and split again, which results in the continuous exchange of their contents. The exchange occurring by collisions of nanodroplets or micelles is controlled by diffusion. It is governed by the interaction between the surfactant adsorption layers and by the flexibility of the interface. Reverse micelles and reverse emulsions are widely used for the synthesis of nanoclusters; here, the inner volume of the reverse micelle serves as a nanoreactor. This is achieved by mixing two identical reverse microemulsion systems, aqueous phases containing, *e.g.*, substances A and B that can react to give a poorly soluble compound C. Coalescence of micelles is accompanied by exchange of A and B and thus formation of the new compound C (Fig. 9).

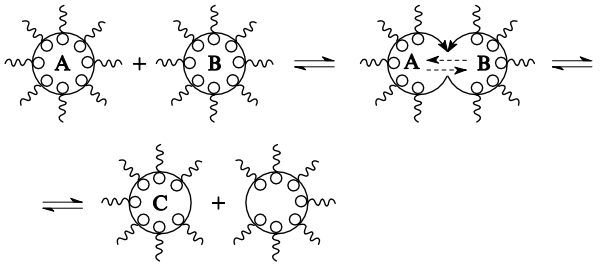


Figure 9. Scheme of reactions in reverse micelles.

Metal clusters can also be prepared by introducing a reducing agent (hydrogen or hydrazine) into a microemulsion containing a metal salt or by passing CO_2 or H_2S through emulsion. This procedure was used to obtain platinum, palladium, rhodium and iridium nanoclusters with the nanoparticle size 3–5 nm and bimetallic platinum/palladium clusters. Metal and semiconductor nanoclusters (*e.g.*, CdS, CdSe, CdTe, SnO_2, TiO_2, Fe_2O_3, MoS_2, HgS, InAs, GaP, GaAs, BiI_3, SiO_2, high-temperature ceramics, *etc.*) were prepared by the synthesis in reverse micelles.[36, 37]

The course of the nanocluster formation in microemulsions is affected by various factors. First of all, this is the aqueous phase/surfactant ratio in the nanosystem

$$W = \frac{[H_2O]}{[\text{Surfactant}]}. \qquad (18)$$

This is followed by the structure and properties of the solibulised aqueous phase, the microemulsion dynamics, the average reactant concentration in the aqueous phase and the nature of the surfactant. The sizes of the clusters formed in the cavity of a reverse micelle can be controlled by varying the size of the micelle. A linear dependence of the cluster size on W in the formation of CdS clusters was established.[40] A similar dependence was obtained in a study of the nucleation of metal oxides in nanopores.[36]

The size of a cluster synthesised in reverse micelle depends on the nature of the surfactant. For instance, the nanosystem stabilised with sodium di(2-ethylhexyl)sulfosuccinate (AOT) was characterised by a smaller cluster size compared to the system stabilised with polyethylene glycol *p*-(*tert*-octyl)phenyl ether with $n = 10$ (Triton X-100).

Synthesis in reverse micelles offers considerable prospects for the preparation of nanoclusters of various chemical composition and shape. In particular, copper clusters of various shape can be obtained using water micelles stabilised with $Cu(AOT)_2$ and

Na(AOT) in isooctane. They are mixed with a microemulsion of Na(AOT)-stabilised sodium borohydride. Mixing of the microemulsions leads to reduction of copper, the size of the copper cluster being dependent on W.[41]

At $W < 4$, the system contains only spherical droplets whose size is proportional to W. In the range from 1 to 12 nm the cluster diameter (d) obeys a linear relation $d \sim aW$. As the water content increases ($4 < W < 5.5$), micelles lose their spherical shape. As a result, spherical nanoclusters (d = 8, 2 and 12 nm) and cylindrical clusters 12 and 18.5 nm long are formed in the microemulsion system. Further increase in W ($5.5 < W < 11$) is accompanied by the formation of a continuous phase containing spherical nanoclusters (d = 6.7–9.5 nm) and rod-like nanoclusters of diameter 9.5 nm and length 22.6 nm. At $W > 11$, a lamellar structure built of rods of diameter 10–30 nm and length 300–1500 nm is formed. The synthesis of asymmetrical (rod-like, disk-shaped and ellipsoidal) clusters is of great scientific and practical interest. Using reverse micelles and emulsions, it is possible to prepare nanocomposites of the core–shell type.[42]

Formation of micelles based on block copolymers. A block copolymer includes blocks characterised by strongly different solubilities. In particular, a diblock copolymer containing a hydrophilic and a hydrophobic component can form both simple spherical micelles and complex lamellar or two-phase structures in water. However, the block-copolymer-based micelles differ from the micelles prepared using simple surfactants by greater critical radii (from 7 to 15 nm) and higher stability.[43] A general scheme of preparation of such micelles is shown in Fig. 10.

Spherical micelles formed in a block-selective solvent consist of a core including an insoluble segment and a shell formed from the soluble block. Structural stabilisation of micelles occurs through polymerisation or cross-linking of the molecular fragments of the core or the shell and formation of the core- or shell-linked micelles, respectively. If the nanosystem is formed in the solid phase, the nature and size of aggregates depends on the relative size of each block and the molecular mass of the block copolymer. If a diblock copolymer has a short soluble block and a long insoluble block, twisted truncated micelles, vesicles, cylindrical elongated or flattened aggregates are formed; otherwise, spherical aggregates called star-like micelles are formed. In lyotropic systems it is possible to vary the solvent. For instance, an increase in the concentration of the block-selective solvent with respect to the concentration of the solvent affecting both blocks causes the formation of vesicles and cylinders.

Thus, the lyotropic system provides additional opportunities for controlling the formation of nanoscale objects.

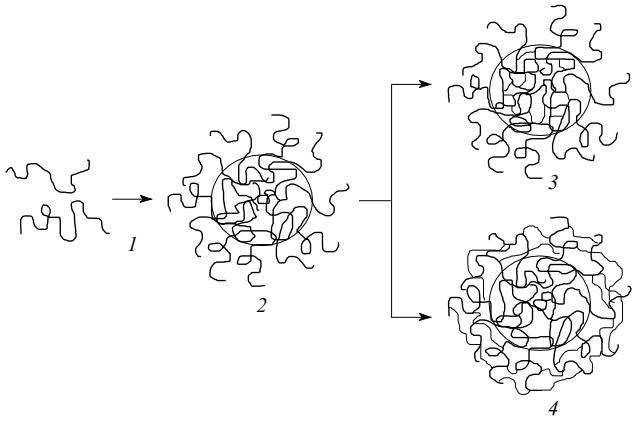


Figure 10. Scheme of micelle formation involving block copolymers. Dissolution of monomeric block copolymers in block selective sorbent (*1*), formation of micellar aggregate (*2*), formation of cross-links in the block copolymer core (*3*) and formation of cross-links in the block copolymer shell (*4*).

Organisation and self-organisation of colloidal structures. Self-organisation and evolution of a colloidal nanosystem is due to the presence of a well-developed surface and thermodynamic instability of colloidal clusters. The excess free energy resulting from the existence of an interface between the dispersed phase and the dispersive medium stimulates various processes resulting in a decrease in the Helmholtz free energy (F). Ignoring the chemical potential, one can write

$$dF = -TdS + d(\alpha s), \tag{19}$$

where α is the surface tension and s is the surface area of the phase boundary. The thermodynamic condition $dF < 0$ can be met by reducing the interface surface area $\alpha ds < 0$ or the interface energy $sd\alpha < 0$; this is accompanied by a change in the entropy of the system. As the interface surface area decreases, the average cluster size increases and the colloid can undergo phase separation into two phases, solid and liquid. Coalescence of clusters is precluded by the energy barrier originating from electrostatic repulsion (E_{el}). For instance, if $E_{el} \gg kT$, the system is stable against aggregation and no larger particles are formed. At $E_{el} \ll kT$, each intercluster collision will lead to aggregation with the rate limited by the diffusion rate in the dispersive medium.

As the concentration of the electrolyte decreases, the coagulation rate decreases (slow coagulation). Coagulation of sols produces aggregates the fractal dimension of which depends on the type of coagulation. The fractal dimension of the aggregates obtained under slow coagulation exceeds that of the aggregates obtained under fast coagulation conditions, which indicates a better organisation in the former case. Long-range cluster–cluster interaction causes the formation of macroscopic ensembles that exhibit the phase stability. Such ordered objects were called periodic colloidal structures.[44]

Surfactant solutions are appropriate for not only self-organisation of molecules in micelles, but also organisation of ordered nanostructures built of the metal and metal oxide clusters prepared by micellar technique. In particular, chemical reactions involving conventional and reverse micelles are widely used for the synthesis of colloidal clusters of 1 to 10 nm size. For instance, Ag_2S clusters are prepared using microemulsions containing two types of reverse micelles, with Na_2S and Ag–surfactant. Collisions, coalescence and exchange of the contents of the aqueous phases lead to formation of Ag_2S clusters whose size is controlled by the micelle size. The cluster size increases from 3 to 5.8 nm in the range mentioned above as the size of the reverse micelle increases,[45] which is consistent with the model of nucleation in a closed pore.

To release the nanoclusters from the micelle, the latter is destroyed by thiols, the resulting clusters are dissolved in appropriate solvents (*e.g.*, benzene), the solution is filtered and then the solvent is evaporated. This procedure allows one to prepare monodisperse nanoclusters of size up to 10 nm passivated by thiols (*e.g.*, dodecanethiol). Then, ordered nanostructures (colloidal crystals) are formed from these clusters immobilised on certain supports. Two- and three-dimensional colloidal crystals were synthesised from metallic gold, cobalt and silver clusters as well as from the metal oxide and metal chalcogenide clusters.[36] Alkanethiols, alkylphosphines and dithiols are used as nanocluster surface passivators.

Figure 11 presents photomicrographs of the Ag_2S nanostructure formed from passivated nanoclusters of size 5.8 nm. Like a conventional crystal, it can contain dislocations and defects. Two-dimensional nanostructures are close-packed monolayers and three-dimensional structures have a face-centred cubic lattice. The clusters assemble into crystals under the action of weak van der Waals interactions similarly to crystallisation of molecular clusters or noble gas clusters. Apparently, weak intercluster interactions are necessary for the formation of ordered nanostructures.

Yet another important condition for organisation of ordered cluster crystals is undoubtedly the monodisperse character of

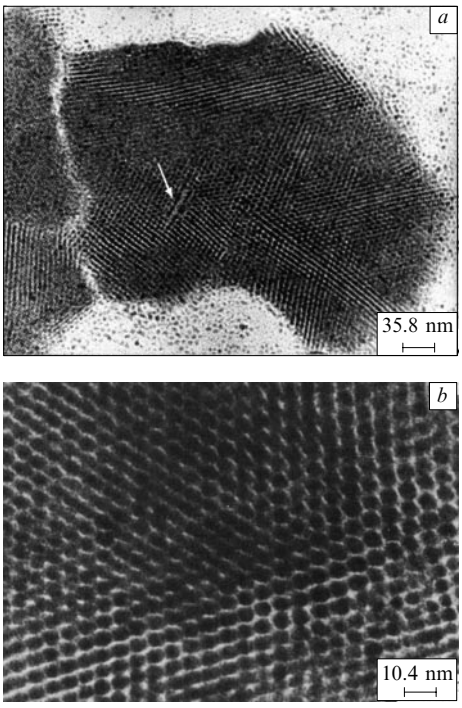


Figure 11. Ag_2S nanostructure micrographs obtained at different magnification.[45]
White arrow points to a defect in the crystal structure of colloidal crystal.

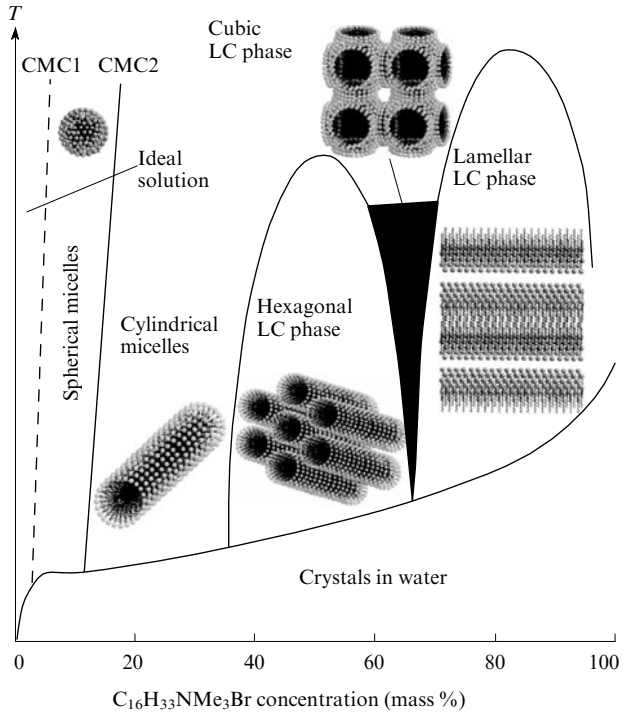


Figure 12. Phase diagram for the $H_2O-C_{16}H_{33}NMe_3Br$ system with two critical micelle concentrations (CMC1 and CMC2).

clusters. Colloidal clusters are used as key elements in nanoelectronics and nanooptics, as well as nanomagnets; because of this, requirements for the strength and stability of such structures become more stringent. Here, it would be more appropriate to work with covalent bonds and covalent crystals. However, the latter cannot be obtained by the methods employed in the crystallisation of colloidal nanocrystals (namely, by coating a substrate followed by evaporation). Ordered nanostructures with monodisperse nanopore or nanofibre size are prepared by template methods using micelles (templates) that set the size of the nanosystem. In this connection the formation of mesoporous silica and alumina is a characteristic manifestation of discrete critical sizes.

Mesoporous silica. Mesoporous silica is prepared by polycondensation of silicon compounds, *e.g.*, tetramethoxysilane or tetraethoxysilane (TEOS) in the presence of surfactant molecules that form a micelle and play the role of a template.[46] In particular, this procedure is used for fabrication of the family of molecular sieves M41S.[47] Hydrolysis of TEOS causes the formation of silicas on the surface of surfactant micelles. An example of the material for the micelle and template is provided by cetyltrimethylammonium bromide $C_{16}H_{33}NMe_3Br$. The phase diagram of the water – $C_{16}H_{33}NMe_3Br$ system is shown in Fig. 12.

Bifunctional $C_{16}H_{33}NMe_3Br$ molecules are amphiphilic, *i.e.*, they contain hydrophilic groups and hydrophobic tails that are directed to the centre of the micelle. The shape of micelles and the degree of micelle formation depend on the surfactant concentration. At high concentrations, the surfactant molecules aggregate to form liquid-crystalline (LC) phases with temperature-dependent structures. Removal of organic micelle template results in mesoporous silica with monodisperse pore size. The pore size can be varied by varying the hydrocarbon chain length in the surfactant molecule. For instance, the pore size in the nanosystem synthesised using $C_nH_{2n+1}NMe_3Br$ (where $n = 8$, 10, 12, 14, 18) as template increases by 0.45 nm as the n value changes by 2.

Silica-based nanostructures also include critical-size particles determined by the principles of close (hexagonal or cubic) packing. With block copolymers as templates, the pore size increases; using triblock copolymers, one can prepare pores 5 – 30 nm in diameter and nanostructures with hexagonal packing.

Mesoporous silicon films deposited from the mesophase (prepared similarly) to bulk material are of the greatest interest. In such films, mesopores represent channels aligned with the substrate surface due to minimisation of the film – substrate interaction energy. For instance, the widely used MCM-41 films have the (100) orientation; they can be prepared on the (110)-oriented silicon substrates.

Porous alumina. Anodic oxidation of high-purity alumina foil produces monodisperse alumina that self-assembles into a nanostructure with nanopores of size from 15 to 100 nm depending on the voltage applied (30 to 150 V).[48] Alumina membranes thus obtained serve as templates for fabricating, *e.g.*, nanowires. The fact that porous alumina is formed in various electrolytes has long been known,[49] however fabrication of material with controllable monodisperse nanopore size distribution and assembling templates began only recently. Electrolytic anodic oxidation of alumina surface followed by etching leads to the formation of an ordered hexagonal system of nanopores (channels).

Electrolytic anodisation is schematically shown in Fig. 13. The first stage of oxidation proceeds in an acidic medium and results in the formation of Al_2O_3 nanoclusters that form a discrete ordered structure on polished aluminium surface. The 'bottom' clusters merge with organised pore network of the same size in metallic aluminium. After etching of the oxide clusters the aluminium surface is covered with a hexagonally patterned network of pores with monodisperse size distribution. In the second stage of electrolytic oxidation the hexagonal pattern of the surface acts as a template for the growth of an oxide nanostructure that includes cylindrical nanopores with walls 10 – 30 nm thick and nanopores of size ranging from > 10 to 20 nm the surface of which is coated with alumina. The next stage involves removal of aluminium by, *e.g.*, mercury chloride. This results in an Al_2O_3 membrane with a honeycomb structure and closed channels that can be opened chemically or by using an ion beam. SEM images of such a membrane are presented in Fig. 14. The images show a

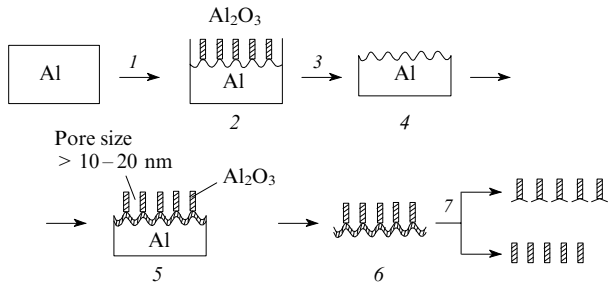


Figure 13. Scheme of fabrication of porous aluminium.[49]
Purification of aluminium (*1*), first stage of anodic oxidation (*2*), etching (*3*), hexagonal organisation of surface pores (*4*), second stage of anodic oxidation involving formation of Al_2O_3 (*5*), surface etching (*6*) and pore opening by ion beam and chemical treatment (*7*).

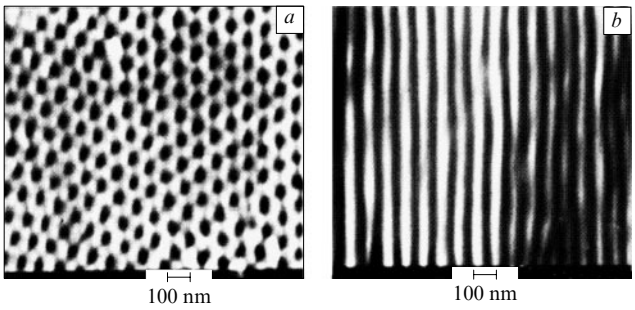


Figure 14. SEM images of Al_2O_3 coplanar (*a*) and normal to (*b*) the membrane surface.[48]

patterned structure with monodisperse pores (channels). Deviations of geometric parameters from specified values can be due to structural defects.

c. Molecular clusters

Initially, ligand-stabilised molecular clusters have been the subject of studies in the fields of coordination and structural chemistry. At the same time unusual structure and properties of these species, originating from the presence of a core of metal atoms, gave an impetus to the development of a separate field of science, cluster chemistry, possessing its own computational, synthetic and other methods of investigation. Interest in this type of clusters increased in connection with the development of nanochemistry and nanotechnology, which permit preparation of nanomaterials and fabrication of nanodevices based on molecular clusters. In this Section we will consider the structure and properties of molecular clusters of size 1–3 nm. Molecular clusters with metal cores and clusters based on metal oxides will be described separately.

Molecular metal clusters. The core of a molecular cluster is formed in accordance with the packing pattern of metal complexes and the principle of closest packing of atoms.[50]

The largest molecular clusters are synthesised based on noble metals, palladium and platinum. The formation of their cores obeys the principle of closest packing of atoms.[51, 52]

The number of atoms in a nanocluster constructed in the form of regular 12-vertex polyhedron (cuboctahedron, icosahedron or anticuboctahedron) can be calculated from the expression

$$n = \frac{1}{3}(10N^3 + 15N^2 + 11N + 3), \qquad (20)$$

where N is the number of layers around the central atom. Thus, the smallest close-packed core contains 13 atoms, that is, one central atom and 12 atoms in the first layer. Relation (20) gives a set of 'magic' numbers of atoms n = 13, 55, 147, 309, 561, 923, 1415, 2057, 2869, *etc.* corresponding to the most stable cores of metal clusters (similarly to the noble gas clusters). Indeed, the following clusters are known: 13-atom (single-layer) clusters $[Au_{13}(diphos)_6](NO_3)_4$ (diphos is $Ph_2PCH_2CH_2PPh_2$) and $[Rh_{13}(CO)_{24}H_3]^{2-}$ with icosahedral and cuboctahedral cores, respectively (see, *e.g.*, Ref. 36); 55-atom (two-layer) clusters $Au_{55}(PPh_3)_{12}Cl_6$, $Rh_{55}(PPh_3)_{12}Cl_6$, $Pt_{55}(AsBu_3)_{12}$, $Ru_{55}.(PBu_3)_{12}Cl_{20}$ with cuboctahedral cores; a 309-atom (four-layer) cluster $Pt_{309}(phen')O_{30\pm10}$ [phen′ is the sodium salt of 4,7-bis(phenylsulfate)-1,10-phenanthroline] with a cuboctahedral core; a 561-atom (five-layer) cluster $Pd_{561}phen_{60}(OAc)_{180}$ (phen is phenanthroline) with an icosahedral core; a 1415-atom (seven-layer) cluster $Pd_{1415}(phen)_{60}O_{\sim1100}$ and a 2057-atom (eight-layer) $Pd_{2057}(phen)_{84}O_{\sim1600}$ cluster. The structure of the $Pd_{561}(phen)_{60}.(OAc)_{180}$ cluster is schematically shown in Fig. 15.[53]

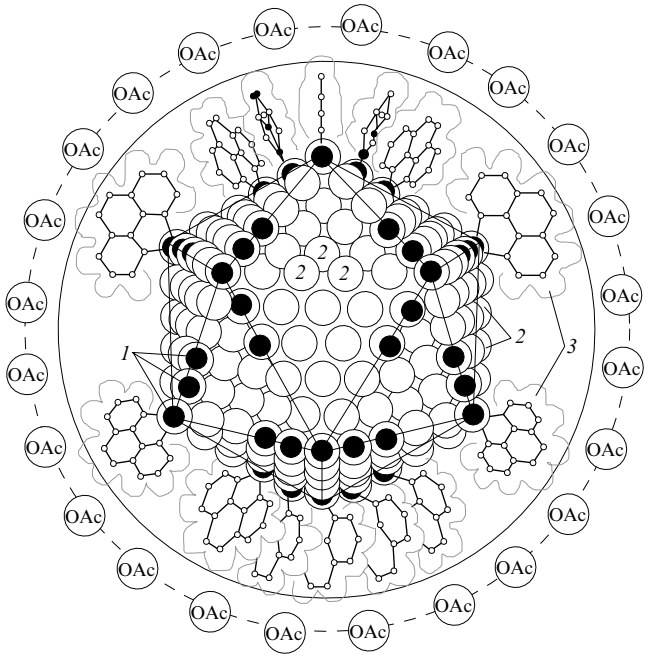


Figure 15. Structure of giant cluster $Pd_{561}(phen)_{60}(OAc)_{180}$.[53]
(*1*) Surface palladium atoms bonded to bidentate phen ligands; (*2*) surface palladium atoms nonbonded to phen ligands; (*3*) phen ligands.

Molecular clusters based on metal oxides. The cores of molecular clusters based on metal oxides are built of $\{MO_x\}$ polyhedral units, where M stands for the metal in high oxidation state. Polyhedra can interact with one another and thus form clusters comprising tens and hundreds of metal atoms. Large clusters are known for tungsten, vanadium and molybdenum oxides, the last-named being the largest.[54, 55] Most molybdates possess a mixed valence and form basic units, $\{Mo_8\}$ and $\{Mo_{17}\}$, which are then used for constructing larger clusters. An important feature of such clusters is the presence of the large fragments $\{Mo_{17}\}$. By linking them through various electrophilic groups, *e.g.*, $\{MoO_2\}^{2+}$, one can obtain very large clusters. Using other electrophilic ions, such as Fe^{III} or V^{IV}, it is possible to form giant-size cluster fragments with the $\{Mo_{57}M_6\}$ metal core (M is iron or vanadium in different oxidation states), which can act as giant building blocks. In particular, a compound $\{(NH_4)_{12}[Mo^{VI}_{45}Mo^{V}_{6}(MoNO)_6Fe^{III}_6Fe^{II}_{1.5}.(OH)_3(H_2O)_{30}]\cdot 64\,H_2O\}_n$ was obtained. It contains the cluster fragment $\{Mo_{57}Fe^{III}_6\}$, which is similar to the structures considered above.

Using the basic cluster blocks, one can continue the cluster buildup.[54] For instance, cluster anions $[Mo_{154}(NO)_{14}O_{448}.H_{14}(H_2O)_{70}]^{28-}$ were obtained. This giant ring-type anion consists of 140 octahedral bipyramids $\{MoO_6\}$ and 14 pentagonal

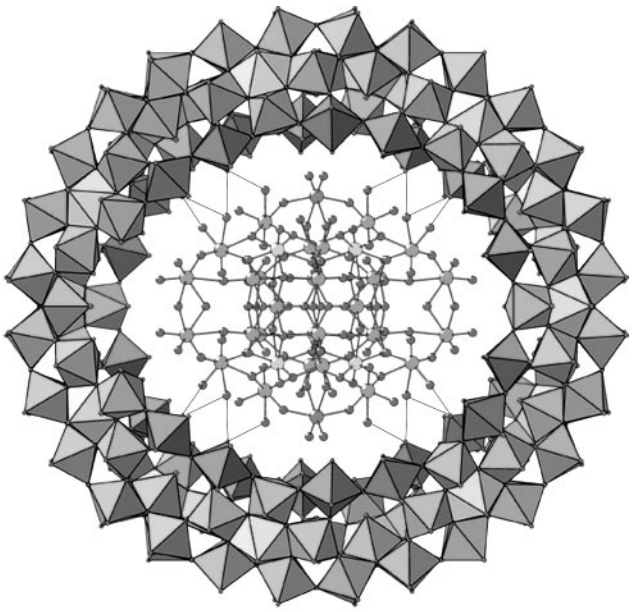


Figure 16. Structure of supramolecular system $\{Mo_{36}@Mo_{148}\}$ in polyhedral representation.[56]
Light and dark octahedra denote $\{Mo_6\}$ and $\{Mo_8\}$ units, and pairs of $\{Mo_2\}$ units are given in gray.

bipyramids $\{Mo(NO)O_6\}$. The equatorial diameter of the central cavity is $\sim$2 nm. This anion can be treated as an assembly composed of 14 subunits. Each subunit is a $\{Mo_8\}$ fragment with the $\{Mo(NO)O_6\}$ pentagonal pyramid at the centre. The $\{Mo(NO)O_6\}$ unit shares vertices and edges with seven $\{MoO_6\}$ octahedra. Chains built of ring-type clusters can serve as 'hosts' for smaller 'guest' clusters, *e.g.*, a $\{Mo_{36}\}$ cluster (Fig. 16). In this supramolecular nanocluster system $\{Mo_{36}@Mo_{148}\}$ the 'host' and the 'guest' are linked through 16 hydrogen bonds and four Na^+ cations arranged between the 'host' and the 'guest'.

Giant ring-type clusters based on metal oxides possess some features differing them from the metal clusters. First of all, this is the presence of nanometre-sized cavities and the possibility of varying the nanoscale supramolecular organisation, well-developed hydrophilic surface suitable for sorption of various substances, *e.g.*, activated charcoal, and replacement of the H_2O ligands by other molecules, which is accompanied by changes in the properties of the nanostructure. Finally, such systems are appropriate for modelling many catalytic reactions, because the composition of the surface of the cluster involved in the reaction is known with certainty.

Another group of molecular clusters based on metal oxides includes highly symmetric clusters (keplerates) with one central point[56] and layered structure. For example, giant spherical molecular clusters are built of 12-vertex icosahedra and pentagonal fragments.

The pentagonal fragments $\{(Mo)Mo_5\}$ consist of the central pyramid MoO_7 which shares edges with five MoO_6 octahedra. In the presence of binuclear linkers $\{Mo_2^{V}O_4\}^{2+}$, an icosahedral molecular system is formed, which comprises 12 pentagons and 30 linkers. If the $\{Mo_2^{V}O_4\}^{2+}$ groups have acetate ions as bridging ligands, a spherical cluster of composition $[Mo_{72}^{VI}Mo_{60}^{V}O_{372}.(AcO)_{30}(H_2O)_{72}]^{42-}$ is formed. Here, the central molybdenum atoms in the $\{(Mo)Mo_5\}$ fragments occupy 12 vertices of an icosahedron and the $\{Mo_2^{V}O_4\}^{2+}$ groups form 30 edges of this polyhedron. Such clusters form polymer networks and serve as building blocks for constructing even larger aggregates. These blocks are sufficiently flexible and can change the shape upon minor changes of corresponding boundary conditions during the synthesis; they can adjust the size and shape to one another. A giant oxomolybdate cluster composed of 386 metal atoms $\{Mo_{368}\}$ and 1880 non-metal atoms (ignoring hydrogen atoms) was synthesised.[57] The cluster similar in size to haemoglobin molecule was obtained by linking 64 $\{Mo_1\}$ fragments, 32 $\{Mo_2\}$ fragments and 40 $\{Mo(Mo_5)\}$ fragments. The formation of this cluster is accompanied by symmetry violation. The cluster structure includes a giant mixed-valence cluster anion (Fig. 17) $[H_x\{Mo(Mo_5)\}'_8\{Mo(Mo_5)\}''_{32}\{Mo_2\}'_{16}\{Mo_2\}''_8\{Mo_2\}'''_8\{Mo_1\}_{164}]^{48-}$, where $\{Mo(Mo_5)_8\} \equiv \{Mo_6O_{21}(H_2O)_6\}$, $\{Mo(Mo_5)'' \equiv \{Mo_6.O_{21}(H_2O)_3(SO_4)\}$, $\{Mo_2\}' \equiv \{Mo_2O_3(H_2O)_2\}$, $\{Mo_2\}'' \equiv \{Mo_2(O_t)_2(O_{br})_3(SO_4)\}$, $\{Mo_2\}''' \equiv \{Mo_2(O_t)_4(O_{br})(SO_4)\}$, $\{Mo_1\} \equiv \{MoO(H_2O)\}$, $x \approx 16$.

Compound $Na_{48}[H_xMo_{368}O_{1032}(H_2O)_{240}(SO_4)_{48}] \cdot ca.1000\,H_2O$ crystallises in the *I*4*mm* space group. Its unit cell contains two giant lemon-like cluster anions having an approximate symmetry D_4 with almost spherical central fragment $\{Mo_{288}O_{784}(H_2O)_{192}.(SO_4)_{32}\}$ (fragment **B**) and two 'caps' $\{Mo_{40}O_{124}(H_2O)_{24}(SO_4)_8\}$ (fragments **C**). The **B** and **C** fragments have different local symmetry, D_{4d} and C_4, respectively. The transition between two types of symmetry is shown in Fig. 17 *a*. The anion consists of 6 building blocks mentioned above that form a cavity of size 2.5×4.0 nm, which can contain up to 400 water molecules. The use of giant ring-type and spherical molecular nanoclusters allows one to go to larger clusters possessing different properties on the one hand and to 'tune' the chemical reaction to proceed at the specified centres on the other hand. The use of such systems is also quite promising for carrying out the reaction inside the giant cluster cavity.

3. Critical dimensions of clusters formed in solid-phase reactions

Solid-phase nanoclusters are main structural units of any nanostructures. Processes resulting in the formation of solid-phase nanoclusters are not rare to occur. For instance, this can be melt or solution crystallisation, sintering, various martensite transformations, crystallisation from amorphous systems, formation of magnetic and ferroelectric domains and spinodal decomposition. All these processes obey the laws of thermodynamics and are accompanied by the ordering and self-organisation phenomena.[58, 59]

The fashion of assembling a condensed nanosystem from clusters strongly depends on the procedure for cluster formation. A nanostructure can be formed from individual clusters by compaction or nanostructuring of a bulk solid. These techniques are of great importance for the design of nanomaterials based on metals, alloys, oxides, ceramics, *etc.* In addition to the nanostructure formation studies, an important research aspect involves investigation of the mechanical, thermal, electronic and magnetic properties that are responsible for the quality and field of application of many structural materials.

a. Cluster nucleation in solids

Thermal decomposition of a metal compound at temperatures above certain critical (threshold) temperature is accompanied by the formation of a mobile reactive medium in which metal oxide (*e.g.*, iron oxide) nanoclusters nucleate. The formation of clusters can be treated as nucleation from individual atoms in solution or melt within a confined volume (*e.g.*, in a pore volume). The volume can be controlled by diffusion, which prevents the concentration fluctuation of the bulk medium (due to the change in the cluster size) from travelling a distance longer than $L \sim (Dt)^{1/2}$ (D is the diffusion coefficient) during the nucleation time (t). Here, it is this distance that can be considered as the size of the cell in which the cluster is confined; the components of the bulk medium cannot escape this cell.

For a system of non-contacting clusters the dependence of the Gibbs free energy (ΔG_{fc}) on the cluster radius (r) for one cluster in the course of atomic nucleation is given by

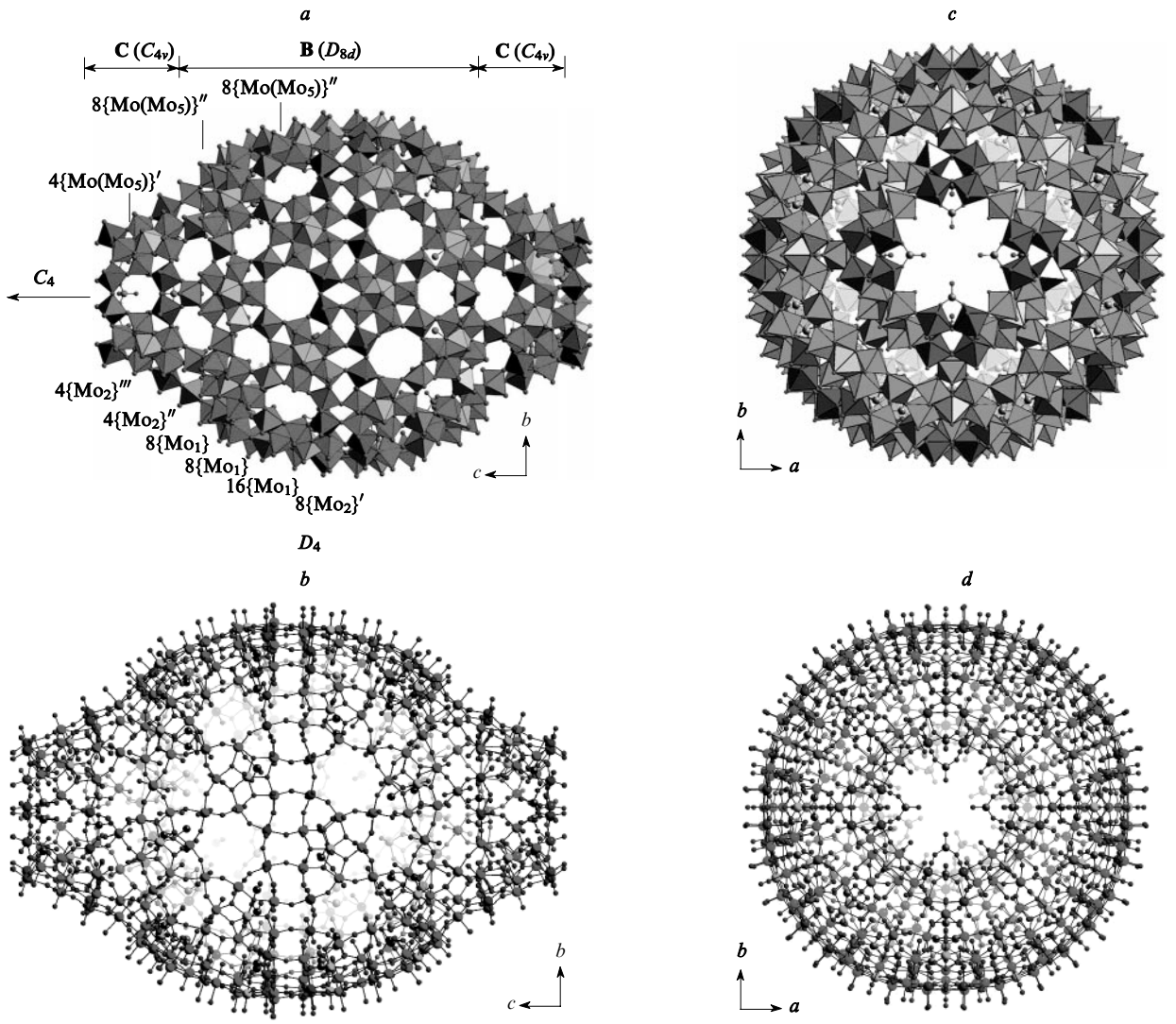


Figure 17. Structure of the $\{Mo_{368}\}$ anion in crystals in polyhedral (*a*, *c*) and ball-and-stick (*b*, *d*) representation.[57]
Shown are different building blocks and regions with different symmetry; the building blocks include $\{Mo_1\}$, $\{Mo_2\}$ and $\{Mo(Mo_5)\}$.

$$\Delta G_{fc} = 4\pi r^2 \alpha_c - \frac{4}{3}\pi r^3 \rho_c \Delta\mu_c\,, \tag{21}$$

where α_c is the density of the free surface energy of the cluster, ρ_c is the density of iron atoms in the cluster and $\Delta\mu_c$ is the change in the chemical potential of iron upon transfer of one atom from the bulk medium to the cluster structure. It should be noted that in this representation the surface energy is independent of the cluster size and fulfilment of relation (21) implies that the laws of thermodynamics are applicable up to a cluster size of 1 nm.

Let the mixture contain N atoms per cluster, let n_0 out of N atoms be the iron atoms and let $n_c = (4/3)\pi r^3\rho$ iron atoms be in the cluster structure. Then, at $N \gg n_0$ one has

$$\Delta\mu_c = \Delta\mu_c^0 + \ln\frac{n_0 - n}{N}\,. \tag{22}$$

Here $\Delta\mu_c^0$ is the change in the standard chemical potential of iron upon transition of one iron atom to the cluster structure, measured in units of kT.

Initially, clusters do not contact one another. Denoting the volume and the surface area of the non-contacting cluster by $V_{fc} = (4/3)\pi r^3$ and $S_{fc} = 4\pi r^2$, respectively, expression (21) can be rewritten in the form

$$\Delta G_{fc} = \alpha S_{fc} - \left(\Delta\mu_c^0 + \ln\frac{n_0 - n}{N}\right) V_{fc}\,. \tag{23}$$

The function ΔG_{fc} has a maximum at $r = r_{cr}$ and a minimum at $r = r_{max}$ (Fig. 18).

Relation (23) characterises the stages of cluster nucleation and growth in a weakly interacting system of non-contacting

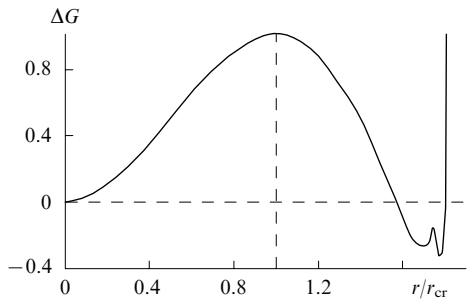


Figure 18. Change in the Gibbs free energy plotted *vs.* increase in cluster size upon nucleation and subsequent sintering for $r_t = 1.75\,r_{cr}$.

clusters. As the cluster size increases, clusters contact one another, thus initiating the sintering. The onset of sintering indicates a strong interaction between clusters. If the distance, $2r_t$, between the centres of clusters is constant, the surface area S_{sc} and the volume V_{sc} of a cluster contacting k neighbours are quite correctly given by

$$S_{sc} = 4\pi r^2 + k2\pi r(r_t - r), \tag{24}$$

$$V_{sc} = \frac{4}{3}\pi r^3 + k\frac{1}{3}\pi r(-2r^3 + 3r^2 r_t - r_t^3).$$

The change in the Gibbs free energy in the sintering stage (at $r > r_t$) is

$$\Delta G_{sc} = \alpha S_{sc} - \left(\Delta\mu^0 + \ln\frac{n_0 - n}{N}\right)\rho V_{sc}. \tag{25}$$

Thus, the profile of the change in the free energy of the system per cluster in the whole range of changes in this parameter is described by relation (23) at $r < r_t$ and by expression (25) at $r > r_t$.

Figure 18 presents the dependence $\Delta G(r/r_{cr})$ for $r_t = 1.75\,r_{cr}$ shown as an example. The curve has three minima separated by two maxima. The minimum at $r = 0$ corresponds to the initial state of the bulk medium. After passing the point r_{cr}, the system goes to the first stable state $r = r_{max}$ and corresponds to the equilibrium state of non-contacting clusters (this is possible at $r_{max} < r_t$). The third minimum corresponds to the system where clusters are sintered and each cluster has k contacts. Correspondingly, the first maximum at $r = r_{cr}$ describes the potential barrier to nucleation and the second maximum corresponds to the potential barrier to sintering. The shape of the potential barrier to sintering for $k = 6$ at different r_t values is shown in Fig. 19. At $r_t = 1.7\,r_{cr}$, sintering occurs barrierlessly; at $r_t = 1.75\,r_{cr}$, *i.e.*, at lower proportion of clusters in the system, transition to sintering involves the overcome of a potential barrier; if the proportion of clusters is even lower ($r_t = 1.8\,r_{cr}$), sintering does not occur because it requires an increase in the free energy.

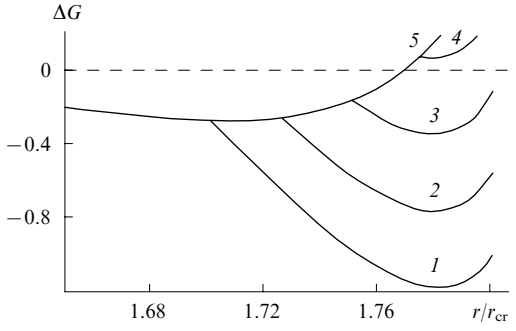


Figure 19. Change in the Gibbs free energy plotted *vs*. increase in cluster size during sintering at different r_t values.
$r_t = 1.7\,r_{cr}$ (*1*); $1.73\,r_{cr}$ (*2*); $1.75\,r_{cr}$ (*3*); $1.77\,r_{cr}$ (*4*); $1.78\,r_{cr}$ (*5*).

Thus, the formation of a nanosystem involves two main stages. The first stage is characterised by weak interaction between clusters (from nucleation to the onset of sintering), while the second stage is characterised by strong interaction between clusters (after the onset of sintering). A change in the character of intercluster interaction causes many properties of the nanosystem to change; in particular, strong intercluster interaction and sintering produce considerable interfacial stresses. They are generated in the formation of an intermediate neck due to the surface tension [60] and obey the dependence $P = \alpha/x$, where α is the surface tension and x is the neck radius in the sintering of clusters. Assuming that for iron oxide $\alpha \sim 1$ N m^{-1} and $x \sim 1$ nm, we get $P \sim 10^9$ Pa. The excess pressure is also produced in the presence of defects and dislocations at the interface and reaches a value of the order of 10^9 Pa for clusters of size ~ 10 nm. The stress and pressure in the system of strongly interacting nanoclusters are the key parameters responsible for the formation and properties of the nanostructure. Probably, solid-phase metal, oxide and chalcogenide nanoclusters can be prepared by low-temperature solid-phase reactions carried out at particular r_t and r_{max} values.

Atomic nucleation and subsequent sintering can be accompanied by cluster nucleation (aggregation of clusters). Indeed, analysis of the changes in the free energy of individual clusters nucleation (ΔG_{fa}) into an aggregate of radius R performed as above for atoms [see Eqn (21)] gives

$$\Delta G_{fa} = 4\pi R^2\alpha_a - \frac{4}{3}\pi R^3\rho_a\Delta\mu_a, \tag{26}$$

where α_a is the surface tension of the aggregate, $\Delta\mu_a$ is the chemical potential of aggregate formation and ρ_a is the density of the aggregate.

Let the mixture contain N atoms per aggregate, let n_0 out of N atoms be iron atoms and let $n_a = (4/3)\pi R^3\rho_a$ iron atoms be in the aggregate structure. Then, at $N \gg n_0$ one has

$$\Delta\mu_a = \Delta\mu_a^0 + \ln\frac{n_0 - n}{N}. \tag{27}$$

Here $\Delta\mu_a^0$ is the change in the standard chemical potential of iron upon transition of one iron atom to the aggregate structure, measured in units of kT. Assuming that, similarly to individual clusters, the cluster aggregates do not contact one another in the initial stage and denoting the volume and the surface area of the non-contacting aggregate by $V_{fa} = (4/3)R^3$ and $S_{fa} = 4\pi R^2$, respectively, expression (27) can be rewritten in the form

$$\Delta G_{fa} = \alpha_a S_{fa} - \left(\Delta\mu_a^0 + \ln\frac{n_0 - n}{N}\right)V_{fa}. \tag{28}$$

The function ΔG_{fa} has a maximum at $R = R_{cr}$ and a minimum at $R = R_{max}$ like the corresponding function for the atomic nucleation of isolated cluster (see Fig. 18). However, the r_{cr} and R_{cr} values should be significantly different. Indeed, for a solid with strong covalent bond between iron and oxygen atoms the surface tension of the iron oxide cluster should be much higher than the surface tension of cluster aggregates due to weak van der Waals forces. The surface tension for such aggregates is unknown, but we can assume that the surface tension of the iron oxide nanocluster is of the order of 1 N m^{-1} (see Refs 61 and 62) and the surface tension of the cluster aggregate lies between 0.073 N m^{-1} (water) and 0.02 N m^{-1} (see Ref. 63) typical of large saturated hydrocarbon molecules; these boundary values are due to the hydrogen and van der Waals bonds, respectively. Then, comparing Eqns (23) and (28), one can expect an increase in R_{cr} by a factor of 15 to 50 compared to r_{cr}. A similar conclusion can also be drawn from comparing the energy of the bond between iron and oxygen atoms in iron oxide cluster (~ 2 eV for the covalent bond) and the energy of the bond between noble gas atoms (~ 0.1 eV for the van der Waals interaction). The bond between the noble gas atoms can be treated as an approximation to the bond between cluster aggregates. Cluster aggregation can occur not only by nucleation. The existence of superaggregates comprising a few aggregates formed in accordance with Eqn (28) and characterised by even lower surface tension and, correspondingly, larger critical radii seems not to be impossible.

b. Design of nanoclusters and nanostructures based on iron oxide complexes

The AFM images of the nanostructures formed from iron oxide clusters, obtained at the decomposition temperature of iron oxalate ($T_d = 210$ °C) are shown in Fig. 20.

The section profiles of the AFM image of a surface area of 600×600 nm along the lines *1* and *2* revealed the formation of two types of nanostructures in the course of thermal decomposition. These are large aggregates of size ~ 300 nm and smaller

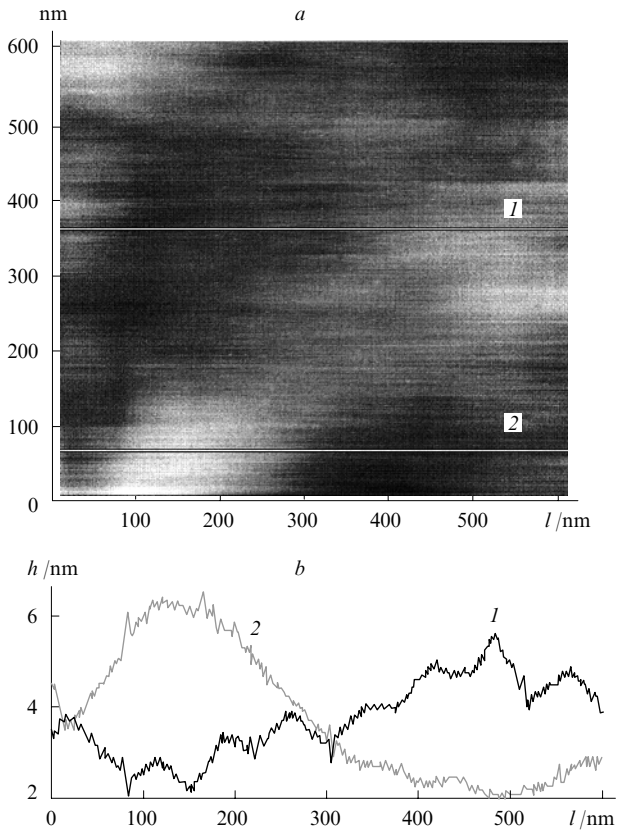


Figure 20. AFM image (*a*) of a nanostructure comprised of oxide iron nanoclusters, formed at iron oxalate decomposition temperature of 210 °C and profiles of the sections *1* and *2* (*b*).

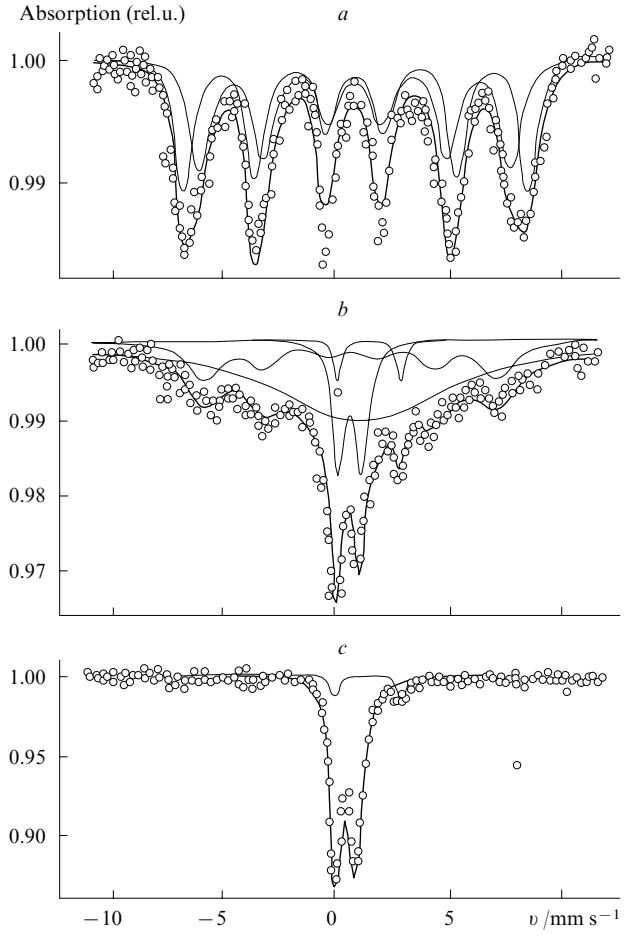


Figure 21. Mössbauer spectra of a nanostructure comprised of oxide iron nanoclusters, formed at iron oxalate decomposition temperature of 210 °C, obtained at 4.2 (*a*), 25 (*b*) and 80 K (*c*).

aggregates of size 70–80 nm. Only one type of aggregates (of size 70–80 nm) was observed in a study of the region 300×300 nm. On both scales (especially, on the 300×300 nm scale) the AFM images show modulation of the aggregate profiles (roughness), which manifests itself as peaks (a total of 25–35 peaks) indicating that aggregates are composed of smaller particles, *i.e.*, nanoclusters whose limiting size was estimated at 2–3 nm. However, the AFM technique cannot look inside the cluster aggregate and determine its structure. To this end, ^{57}Fe Mössbauer spectroscopy was employed.

The Mössbauer spectra of the same nanostructure are shown in Fig. 21. At 4.2 K, the spectrum exhibits a magnetic hyperfine structure (HFS) characteristic of γ-Fe_2O_3. This structure was obtained using the simplest model involving two systems of magnetic HFS corresponding to the surface atoms and to the atoms in the cluster interior. Raising the temperature results in the spectrum diffusion, broadening of the lines of the magnetic HFS and a decrease in the magnetic induction at the nuclear site (B_{in}). Similar spectra are characteristic of superparamagnetic nanoclusters. This makes it possible to estimate the nanocluster size, from, *e.g.*, the simplest equation of superparamagnetism

$$\tau = \tau_0 \exp \frac{KV}{kT}, \qquad (29)$$

where τ is relaxation time of the magnetic moment of the cluster, K is the magnetic anisotropy constant, V is the cluster volume and $\tau_0 = 10^{-9} - 10^{-10}$ s. The relaxation time τ was estimated using the slow relaxation model from the broadening of the components of the magnetic HFS.[64, 65] The spectra of nanoclusters measured at $T_d = 210$ °C were processed with the parameters $\Gamma = 0.62$ and 5.12 mm s^{-1} (Γ is the linewidth of the Mössbauer spectrum) determined from the spectra taken at $T = 4.2$ and 25 K, respectively. The value $\Delta\Gamma = 4.5$ mm s^{-1} at $T = 25$ K corresponds to $\tau \approx 2.2 \times 10^{-9}$ s. Then for $\tau_0 = 10^{-9}$ at $T = 25$ K and $K = (1-2) \times 10^5$ J m^{-3} (see Ref. 66) the average cluster size is 1.4 to 1.7 nm. At 78 K, the τ value decreases and the Mössbauer spectrum exhibits only a quadrupole doublet.

An AFM study of larger clusters obtained at $T_d = 235$ °C revealed no formation of superaggregates including cluster aggregates. The size of the cluster aggregates was found to be nearly the same (~ 80 nm) as that of the nanoclusters obtained at $T_d = 210$ °C. The interior of these aggregates is difficult to see, but according to Mössbauer spectroscopy data, the nanostructure obtained at $T_d = 235$ °C is characterised by a higher superparamagnetic transition temperature (100 K); the nanocluster size was estimated at $\sim 4-7$ nm.

The AFM images become radically different for sintering of nanoclusters. The AFM images and profiles of nanoclusters in the initial stage of sintering ($T_d = 265$ °C) are shown in Fig. 22. The cluster size estimated in a study of a surface area of 500×500 nm in the system of strongly interacting clusters was 30 to 50 nm. A study on a larger scale (150×150 nm) and analysis of the profile of two contacting nanoclusters gave the half-width (14 nm) and height (6.4 nm) of a protrusion of the cluster. The Mössbauer spectra of this nanocluster structure (Fig. 23) are strongly different from similar spectra of two nanostructures considered above. Despite the absence of superparamagnetic relaxation, calculations for these large clusters using expression (29) lead to $\tau \gg 10^{-8}$ s and the spectra show a doublet characteristic of the paramagnetic or superparamagnetic state of the substance up to 100 K. Processing of the Mössbauer spectra obtained at $T = 78$ K revealed two magnetic hyperfine structures corresponding to α-Fe_2O_3 and

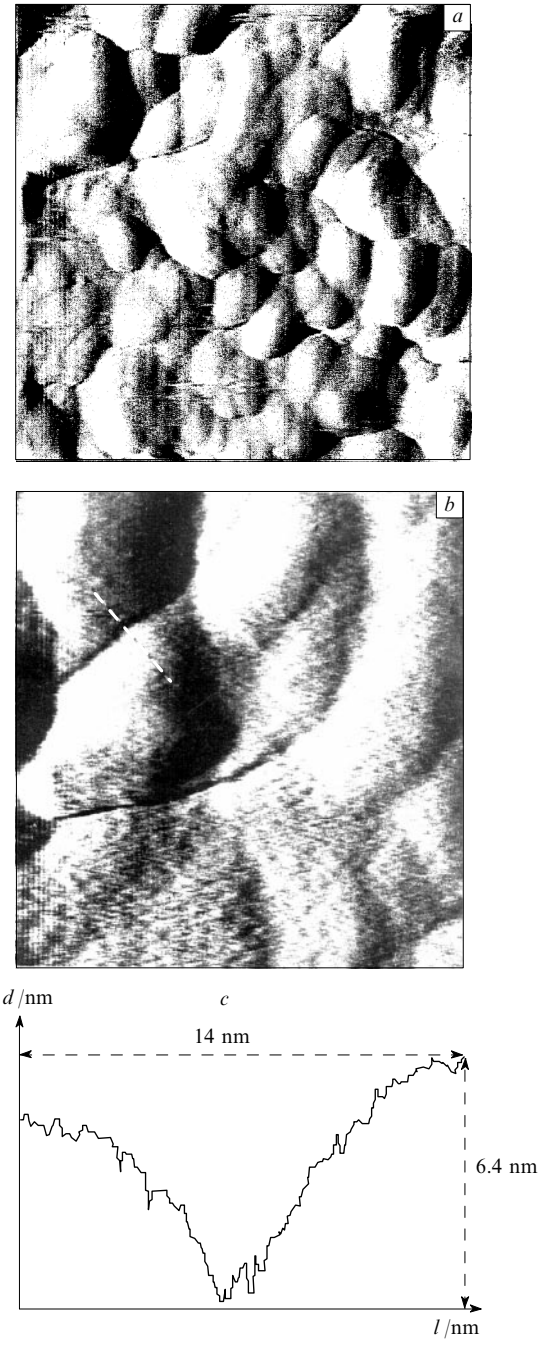


Figure 22. AFM image of a nanostructure comprised of iron oxide nanoclusters.
Scan area 500 × 500 nm (*a*); scan area 150 × 150 nm (*b*) and surface profile along the dashed line shown in Fig. 22 *b* (*c*).

γ-Fe_2O_3. At 120 K and higher temperatures (up to room temperature), the Mössbauer spectra can exhibit one system of magnetic HFS and a quadrupole doublet. A characteristic feature of the series of the Mössbauer spectra with the magnetic HFS (see Fig. 23) is transformation of the magnetic HFS to the quadrupole doublet corresponding to the paramagnetic state of the substance at temperatures much below the Curie or Néel points (T_C = 965 K, T_N = 865 K) of bulk α-Fe_2O_3 and γ-Fe_2O_3, respectively. Interpretation of this result will be given below.

The AFM images of larger nanoclusters obtained at T_d = 500 °C showed the formation of a nanostructure comprising strongly interacting nanoclusters of size ~300 nm in the sintering stage. The room-temperature Mössbauer spectra of this system correspond to bulk α-Fe_2O_3.

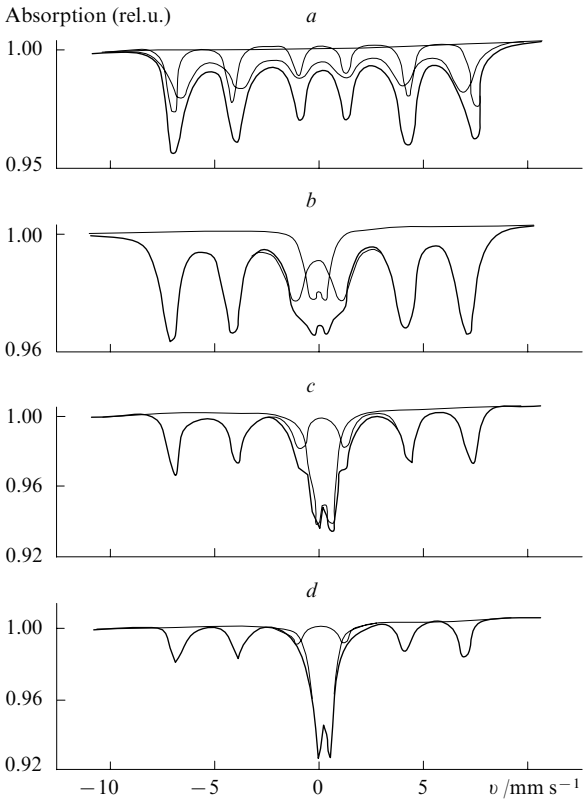


Figure 23. Mössbauer spectra of a nanostructure comprised of oxide iron nanoclusters, formed at iron oxalate decomposition temperature of 265 °C, recordeded at 77 (*a*), 120 (*b*), 160 (*c*) and 300 K (*d*).

III. Critical characteristics and properties of nanoclusters and nanostructures

1. Thermal properties

a. Thermodynamics of cluster melting

The state of a cluster can be considered using a simple thermodynamic model, which makes it possible to predict a number of unusual properties.[36, 67, 68] The free energy difference between the liquid and solid states of the cluster is given by

$$\Delta G = 4\pi r^2 \Delta\alpha + \frac{4}{3}\pi r^3 \rho \Delta\mu, \tag{30}$$

where $\Delta\alpha = \alpha_l - \alpha_s$ is the surface energy difference and $\Delta\mu = \mu_l - \mu_s$ is the chemical potential difference between the liquid and solid state of the cluster. Clearly, at melting $\Delta\alpha < 0$ and $\Delta\mu > 0$. The dependence $\Delta G = f(r)$ is shown in Fig. 24.

The critical cluster size corresponding to the solid–liquid transition ($\Delta G = 0$) is determined using the expression

$$r_{cr} = 3\frac{\Delta\alpha}{\rho\Delta\mu}. \tag{31}$$

At $r < r_{cr}$, the cluster is in the liquid state. From Eqn (31) it follows that the solid–liquid transition state cannot occur for certain matrix atoms (at $\Delta\alpha = 0$), where the cluster does not yet form. At the same time a free cluster should be characterised by the maximum $\Delta\alpha$ value. Any intercluster interactions will cause a reduction of this value and, hence, the critical cluster size, which determines the region of possible fluctuations of the solid and liquid states.

The stability of a cluster can be characterised by the changes in the pressure $\delta P = P_0 - P$ or temperature $\delta T = T_0 - T$, which

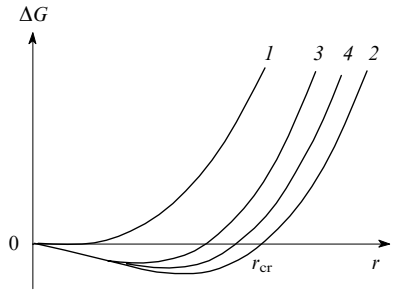


Figure 24. Change in the Gibbs free energy of an ensemble of atoms in a solid (*1*), isolated cluster (*2*) and a system of interacting clusters in the solid (*3*) and liquid (*4*) state plotted *vs.* cluster size.
Interacting clusters (*3*) and clusters treated with surfactants (*4*).

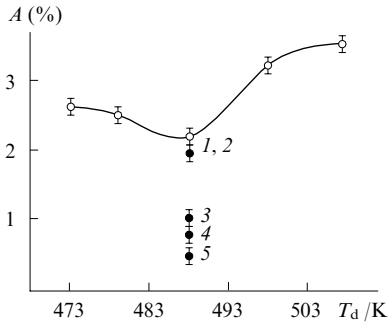


Figure 25. Mössbauer spectral area (*A*) for a nanosystem comprising iron oxide clusters formed upon decomposition of iron oxalate plotted *vs.* decomposition temperature T_d.
Open circles denote experimental data obtained in the absence, and closed circles, in the presence of surfactants: ethanol (*1*), isopropyl alcohol (*2*), Twin-65 (*3*), butanol (*4*) and sodium dodecylsulfate (*5*).

correspond to a given $\Delta\mu = f(p,T)$ value. Due to these changes the phases equilibrate at a specified cluster size (P_0 and T_0 are respectively the pressure in the medium and the melting temperature of bulk material).

Replacing the function $\Delta\mu = f(P,T)$ by its expansion in powers of δp at the point P_0 with allowance for

$$\frac{\partial\mu_l}{\partial P} = V_l,$$

$$\frac{\partial\mu_s}{\partial P} = V_s$$

(V_l and V_s are the molecular volumes of the cluster in the liquid and solid state, respectively), one gets

$$\Delta\mu \approx -(V_l - V_s)\delta P. \tag{32}$$

Using the Clapeyron – Clausius relation

$$\frac{\partial P}{\partial T} = \frac{q}{T_0}(V_l - V_s), \tag{33}$$

where q is the latent heat of phase transition, one can write

$$\Delta\mu \approx -\frac{q\delta T}{T_0}. \tag{34}$$

Substituting Eqn (34) into expression (31), one gets a hyperbolic dependence of the changes in the phase transition temperature on the cluster radius

$$\frac{\delta T}{T_0} \approx -3\frac{\Delta\alpha}{\rho q r}. \tag{35}$$

The relation (35) shows a decrease in the melting temperature with a decrease in the cluster size. Taking into account the plots presented in Fig. 24, we can suggest that at the specified temperature and pressure in the medium the initially stable cluster structure ($\Delta\mu > 0$) goes to a metastable state at $r < r_{cr}$.

A decrease in the melting temperature (down to room temperature) with a decrease in the cluster size was observed for gold, tin, CdS, *etc.* nanoclusters.[69–71] Additionally, an electron microscopy study [70] of tin films revealed separation of the melting and freezing points of the cluster and the existence of a specific solid – liquid state characterised by enhanced mobility of clusters in the intermediate temperature range.

Specific features of the melting of clusters were studied taking iron oxide nanoclusters as an example. Figure 25 presents the results of a Mössbauer spectroscopy study of iron oxide nanoclusters obtained by solid-phase thermal decomposition of iron oxalate. The temperature dependence of the spectral area obtained for the γ-iron oxide nanocluster system shows a minimum at $T_d \approx 488$ K. The T_d value is related to the average size of the iron oxide cluster, namely, an increase in the cluster size from 1–2 to 6–8 nm causes T_d to increase from 488 to 508 K.

The right branch of the spectrum shown in Fig. 25 is associated with a decrease in the spectral area (on lowering T_d) and enhancement of atomic mobility in the cluster. It should be noted that the iron oxide spectra show no 'broad component' corresponding to the motion of the whole cluster as a result of, *e.g.*, diffusion. The left branch of the $A = f(T_d)$ curve in Fig. 25 is associated with further reduction of T_d and, correspondingly, with a decrease in the cluster size up to breakdown of clusters into individual iron (Fe^{3+}) atoms, dimers and trimers (see Fig. 24, curve *1*). Therefore, the minimum in the dependence curve $A = f(T_d)$ at $T_d = 488$ K is probably due to the onset of formation of the iron oxide clusters with reduced melting temperature.

As mentioned above, the state of the cluster surface is governed by the surface energy, and intercluster interactions should cause this parameter to decrease. Intercluster interactions also affect the intercluster atomic dynamics; however, they can weaken under the action of surfactants and the spectral area also considerably decreases upon the action of surfactants. Thus, weakening of intercluster interactions leads to enhancement of the cluster mobility and to a decrease in the melting temperature. Using relation (31), one can estimate the r_{cr} value corresponding to the onset of melting of γ-iron oxide clusters and compare it with the value found from the experimental Mössbauer spectra. With the following values for γ-iron oxide: $\rho = 5.18 \times 10^6$ g m^{-3} (see Ref. 63), $\Delta\alpha \approx 1$ J m^{-2} (see Ref. 62) and $q \approx 10^{-19}$ J m^{-1} (see Ref. 63) one gets

$$r = \frac{aT_0}{\delta T}, \tag{36}$$

where $a = 0.1 - 1.0$ nm. At $T_m = 300$ K, one has $r = 0.1 - 1.2$ nm, which is in good agreement with the values 1–2 nm determined from the Mössbauer spectra.

Note also that the effect of adsorption-induced decrease in the strength of substances (Rehbinder effect), which manifests itself on the atom-molecular level owing to wetting and deformation of the surface under the action of surfactants, can be explained by the appearance of a specific solid – liquid transition state characterised by enhanced mobility of atoms.

b. Quantum-statistical model for cluster melting

The thermodynamic model for cluster melting is simple, but it provides no information concerning (i) the behaviour of the material the cluster is made of during transition from the solid to the liquid state, (ii) the predicted new solid – liquid state and (iii) the critical cluster size corresponding to the formation of this state.

Now we will consider some characteristics of the solid and liquid states. Unlike a solid, a liquid has a variable shape. The

liquid is inelastic and changes its shape under the action of weak forces. A solid exhibits an elastic response to the action of rather strong forces, but breaks down after an overload. The flow behaviour of the liquid implies the appearance of soft modes of atomic motions; most atomic vibration frequencies are much lower than the characteristic vibration frequencies of the atoms in the crystal lattice of a solid ($10^{12}-10^{13}$ s^{-1}). Applying this concept to clusters, one can expect that for a liquid cluster the density of states corresponds to lower frequencies and to lower frequencies of transitions between the states and shallow potential wells that limit such states. This allows the low-energy modes to execute slow motions that induce rearrangement and isomerisation of the liquid cluster. Yet another group of structural characteristics that differ for solids and liquids includes the angular and radial correlation functions. For solids, these functions show clearly seen peaks corresponding to the nearest and next-nearest neighbours. Liquids are characterised by a diffuse peak corresponding to the nearest neighbours and very weak peaks corresponding to more distant atoms. These criteria are also applicable to clusters when identifying the solid or liquid state. The difference between the solid and liquid states of a cluster can also be characterised by the ease of exchange in an atom or molecule with an identical species at another position of the cluster and, correspondingly, by the time taken for the process. For most materials, clusters are in the solid state at low temperatures and energies or in the liquid state at high temperatures and energies. Clusters can exist in some intermediate state ('slush') that differs from both the solid and liquid states and can be detected and studied in, *e.g.*, computer experiments.

The phase equilibrium in clusters can be studied using the thermodynamic and dynamic approaches, which depends on the characteristic times of computational procedures. In the case of static equilibrium one can employ the thermodynamic approach, namely, consider the change in the Helmholtz free energy (ΔF) of an ensemble of clusters comprising n atoms each,

$$\Delta F = \Delta E - T\Delta S, \tag{37}$$

where ΔE is the change in the internal energy upon the change in the state of the cluster material and the entropy S is calculated as follows:

$$S = kT\ln Z, \tag{38}$$

where

$$Z = \sum g_i \exp\frac{E_i}{kT} \tag{39}$$

is the partial function which sets the distribution over the states of the system and g_i describes the degeneracy of the energy level E_i. Quantum-statistical calculations of the function $Z = f(T)$ have been a subject of numerous studies. Knowing the partial function, one can determine almost all parameters of the equilibrium system with N states at a given temperature T. Since a cluster is characterised by a much smaller number n compared to a bulk solid, it is quite natural to expect that Z is calculable. For instance, knowing the vibrational and rotational energy levels of the cluster and the corresponding degeneracies, one can calculate the free energy of the cluster.

The energy distributions over the states of a solid and a liquid are significantly different. At low temperatures, the density of states for the solid is higher than for the liquid, but the situation reverses at high temperatures. The equilibrium transition from the solid to the liquid state occurs at the temperature T_{eq}. Therefore, at low temperatures the energy change ΔE is governed by the vibrational and rotational energy levels of the solid. As the temperature increases, the entropy factor (disordered motions characteristic of liquids) dominates. The T_{eq} value (or the melting point of the cluster) depends on the model for calculation of the states of the solid and liquid and on the number of states, *i.e.*, on the cluster size. At $T = T_{eq}$, both phases (solid and liquid) coexist

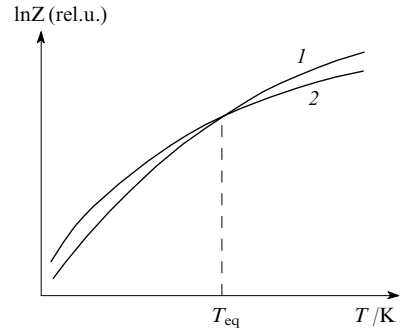


Figure 26. Partial functions (Z) of a solid (*1*) and liquid (*2*) cluster plotted *vs.* temperature.

in the system. The temperature dependence of $\ln Z$ for this model is shown in Fig. 26.

In fact, if we have a model for calculating the energy level and degeneracies, the energy and other thermodynamic parameters can be calculated as certain averaged thermodynamic characteristics that can be more reliable than those determined for individual energy levels and degeneracies.

In addition to the studies of the solid and liquid states of clusters it is of great interest to investigate the transient region and the conditions for stability of these two forms. Here, one should calculate their free energies and find minima corresponding to stable states. The free energy minimum is determined using the non-rigidity parameter of the cluster. The non-rigidity parameter (γ) can be determined, *e.g.*, phenomenologically by comparing two specified spectroscopic frequencies or on the microscopic level by establishing the degree of disorder and the density of defects. Both methods should give correct γ values for the limiting cases of rigid solid ($\gamma = 0$) and non-rigid liquid-like ($\gamma = 1$) states.[72] After introduction of this new parameter of the energy of state the partial functions and the free energies become some functions of γ.

Calculations for the solid state can be carried out using the Einstein or Debye models or the harmonic oscillator model, which lead to qualitatively correct description of the equilibrium state of the cluster. Liquid state calculations are performed in the framework of the Gartenhaus–Schwartz model,[72] which was initially proposed for the atomic nucleus. This pair interaction model applied to an n-atom cluster gives equidistant energy levels with a degree of degeneracy of $(3n-3)$. Analysis of the results obtained using this model showed that the density of cluster states changes differently as the temperature and energy increase; namely, the density of the liquid cluster states increases. Changes in the free energy $F(T,\gamma)$ with an increase in temperature should be studied taking into account the following: only low-lying levels of the solid cluster are populated at low temperatures; the free energy should be a monotonically increasing function of γ; and the free energy of the solid state is lower than that of the liquid state. However, if the temperature increases, the free energy near the non-rigid limit of variation of the parameter γ decreases due to a greater contribution of the $T\Delta S$ term in the expression for the free energy (37) owing to a large number of the available non-rigid cluster forms. In this case near the non-rigid limit the changes in γ at certain temperature are given by

$$\frac{\partial F(T,\gamma)}{\partial \gamma} = 0.$$

This temperature was termed the freezing temperature (T_f). The solid state is stable only at temperatures below T_f. At temperatures above the freezing point, the function $F(T,\gamma)$ has two minima, one near $\gamma = 0$ and the other near $\gamma = 1$. Each minimum corresponds to a locally stable form, which can be compared with, *e.g.*, a stereoisomer. The system will contain two forms in the equilibrium, a solid and a liquid, with a ratio of

$$\frac{[\text{solid form}]}{[\text{liquid form}]} = K_{eq} = \exp\left(-\frac{\Delta F}{kT}\right), \tag{40}$$

where $\Delta F = F_{liq} - F_{sol}$.

These two forms exist in a dynamic equilibrium at which the cluster spends some time in the solid or in the liquid state. At the equilibrium temperature T_{eq}, one has $\Delta F = 0$ and the ratio (40) equals unity. At temperatures between T_f and T_{eq} the solid phase dominates and at temperatures above T_{eq}, the liquid state is preferred. As the temperature increases, the energy of the system decreases until the temperature reaches T_m. Above T_m, there exists only the liquid state of the cluster and the dependence $F(T,\gamma)$ is a monotonic function which decreases as γ increases.

The free energy is plotted *vs.* γ at different temperatures including T_f and T_m in Fig. 27. With these plots, one can imagine the cases where a cluster has a particular freezing temperature (only solid forms are stable below it) and a particular melting temperature (only liquid forms are stable above it). It should be noted that the melting and freezing temperatures of the cluster are different.

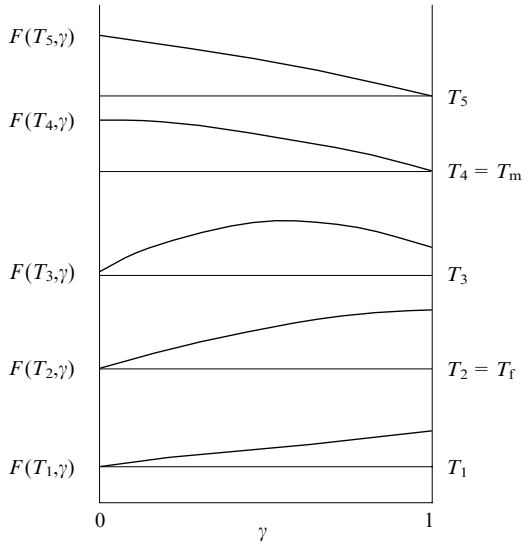


Figure 27. Free energy plotted *vs.* non-rigidity parameter γ for several temperatures.

In principle, the description given above is suitable for those clusters which can have well-distinguishable solid and liquid forms and spend in both states a considerable time sufficient to detect them. Actually, only a few clusters meet these conditions.[73] This was shown to be true for the simplest noble gas clusters Ar_7, Ar_{13}, Ar_{15} and Ar_{19}. Other clusters, namely, Ar_8 and Ar_{14} are characterised by the potential energy surfaces having the shape of a potential well with large 'clapped-out' stair-steps which preclude the formation of stable solid or liquid states. Yet another type of clusters, Ar_{17}, rapidly fluctuates between the solid and the liquid states. Here, it is impossible to discuss the existence of the solid and liquid phases because only the 'slush' state is observed.

It is also interesting to consider the temporal aspect of the existence of the solid and liquid phases in clusters and transitions between them. How much time does it take to detect a phase? Of course, the question cannot be answered within the framework of the thermodynamic approach; one has to re-consider the dynamics of the process. All characteristics should be determined by the time necessary for equilibration of the process (relaxation time) and the measurement time. If the observation times are longer than the relaxation time, it is possible to obtain a time-averaged picture of individual phases; otherwise, pictures characteristic of a given temperature with variable phase ratio are obtained. Experimental data on the melting of clusters and existence of the solid–liquid state corresponded to long observation times ($> 10^{-7}$ s). Similar data were obtained by measuring the spectral linewidths in the optical range. The lines of the probe molecules (*e.g.*, carbazole) attached to argon clusters broadened and shifted to lower frequencies, which was interpreted as melting of argon clusters.[74]

2. Defects and stresses in nanostructures

The appearance of numerous dislocations, defects and intercluster stresses in nanostructures is due to the presence of well-developed interfaces. The density of the interface boundaries (and dislocations associated with them) can be rather high, *e.g.*, $\sim 10^{19}$ cm^{-3} for a nanostructure comprised of 7 nm-clusters. Intercluster interactions or contacts between the cluster and its neighbours produce stresses and an excess pressure at the cluster boundaries. Additionally, assuming that the concentration of dislocations in a cluster is determined by the ratio of the cluster surface area to the cluster volume, the excess energy density of the cluster (ε_d) is [36]

$$\varepsilon_d = \frac{Gb^2}{4\pi(1-\nu)} \ln\frac{R}{R_0}\frac{1}{r}, \tag{41}$$

where G is the shear modulus; b is the Burgers vector characterising the magnitude of the shift of the atoms of an edge dislocations ($b = a/\sqrt{2}$, a is the lattice constant); ν is the Poisson coefficient (usually, 0.3); R is the maximum distance at which the influence of dislocations is still retained; R_0 is the minimum dislocation size; and r is the cluster size.

Thus, in this approximation the excess energy density decreases as the cluster size increases and approaches zero for bulk material. It should be noted that the applicability of this approach to small-size nanoclusters is limited by the thickness of the surface layer of the cluster (which is equal to, *e.g.*, the lattice constant a), *i.e.*, Eqn (41) can be used only for calculating the excess energy of clusters at $r > a$.

When studying the influence of defects and dislocations on the properties of nanostructures, it is interesting to consider the relation between the size of the nanosystem and the density of defects in it. Here, it is convenient to use the thermodynamic approach, which takes into account the chemical potential and the excess energy of the cluster surface. The excess energy gives rise to excess pressure, which equals 1 GPa for 1 nm-clusters. The nanocluster is considered as being surrounded by atoms from the atomic structure and defects (impurity atoms, vacancies, dislocations). It is assumed that the key source of defects is the cluster surface and that defects can be redistributed between atoms inside the cluster, at interfaces and in the intercluster medium. The chemical potential of defects confined within the cluster can be written as

$$\mu_v = \mu_v^0(P) + kT\ln c_v, \tag{42}$$

where P and c_v are respectively the pressure and the defect concentration inside the cluster and μ_v^0 is the standard chemical potential. The chemical potential of the intercluster medium is given by

$$\mu_s = \mu_s^0(P_0) + kT\ln c_s, \tag{43}$$

where P_0, c_s are respectively the pressure and the defect concentration in the intercluster medium and μ_s^0 is the standard chemical potential. At equilibrium

$$\mu_v = \mu_s, \tag{44}$$

it is assumed that the total number of defects in the nanostructure (c_0) is constant; therefore, the concentrations c_s and c_v are related to each other as follows:

$$c_s = c_0 - \frac{1}{q}c_v, \tag{45}$$

where $q(r) = (1 + R/r)^3 - 1$ (R is the thickness of a layer of the intercluster medium).

The pressure drop between the inside and outside of the cluster shifts the equilibrium in the nanosystem and one has

$$\mu_v^0(\delta P) = \mu_v^0(0) + \delta P \upsilon\,, \tag{46}$$

where υ is the defect volume, $\delta P = P - P_0 = 2\alpha/r$ (α is the average surface tension); then one gets

$$\frac{c_v}{c_0} = \left\{ \frac{1}{q(r)} + \exp\left[\frac{\Delta\mu^0(P_0) + 2\alpha\upsilon/r}{kT} \right] \right\}^{-1}. \tag{47}$$

The dependence of c_v/c_0 on the cluster size in the r/a units (a is the lattice constant) is shown in Fig. 28. Calculations were carried out assuming $a = 2\times10^{-10}$ m for the metal and 5×10^{-10} m for the oxide, $\alpha = 1$ N m, the defect volume $\upsilon \sim a^3$ and $\Delta\mu^0 = 0$. The maximum defect concentrations were found for the cluster sizes ranging from 10 to 50 nm; therefore, such clusters have the highest excess energy. The model considered can be explained with ease as follows. In $\sim$100 nm-clusters, the defect concentration is low due to the small specific surface area of these species. If the cluster size is < 10 nm, the specific surface area is large enough, but the surface pressure displaces defects from cluster volume; therefore, small clusters are defect-free objects, which was confirmed experimentally.

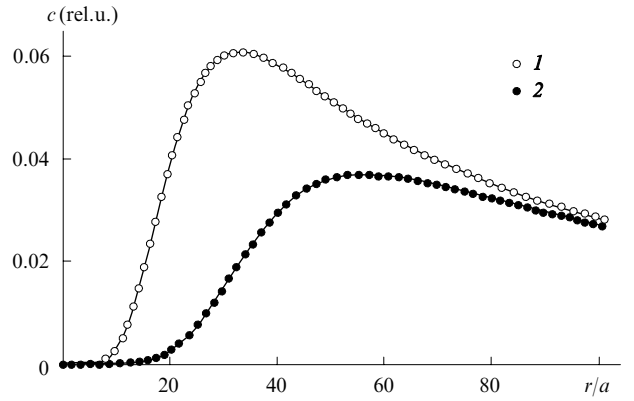


Figure 28. Defect concentration in cluster plotted *vs.* relative cluster radius for oxide (*1*) and metal (*2*) clusters.[75]

The presence of defects in nanostructures and their relation to structural transformations in nanosystems can be determined by both macroscopic methods (by, *e.g.*, measuring the diffusion rate of a tracer through a macrolayer of a chemical substance or the total magnetic susceptibility of the nanosystem) and microscopic techniques (by, *e.g.*, positron annihilation or Mössbauer spectroscopy).[76, 77]

3. Mechanical properties of nanoclusters and nanostructures

Among the mechanical properties of nanoclusters and nanostructures, high hardness and superplasticity should be pointed out. The hardness of a material characterises the resistance to plastic deformation and is measured by indenting with a harder material. The Vickers hardness (H_V), which is used in the text below for characterisation of nanomaterials, is measured from the depth of an indentation on the surface after unloading, being mainly determined by the yield point of the material σ. The grain size of a material is an important characteristic of the microhardness, which obeys the Hall – Petch law,[78, 79]

$$\sigma = \sigma_0 + kd^{-1/2}, \tag{48}$$

where σ_0 is the internal stress, which precludes the motion of a dislocation in bulk material and k is a constant. At temperatures much lower than the melting point of the material, the Vickers hardness is proportional to the yield point. Then one has

$$H_V \approx H_0 + kd^{-1/2}, \tag{49}$$

where H_0 and k are constants.

If deformation occurs by diffusive slip, at temperatures that are much lower than the melting temperature the equation for the deformation rate has the form

$$\frac{d\varepsilon}{dt} = \frac{b\sigma\upsilon RD}{k_B T d^3}, \tag{50}$$

where b is the coefficient of proportionality, σ is the stress applied, υ is the atomic volume, R is the grain boundary thickness and D is the grain boundary diffusion coefficient.[80]

By extending the action range of Eqns (48) – (50) to nanoclusters acting as grains, one case assume that the mechanical properties of nanostructures should be strongly different from those of bulk materials. A decrease in the cluster size should first of all affect the hardness of the nanostructure, which should also increase. At the same time of great importance for nanosized systems is the diffusive slip of nanocrystallites; intensification of this type of motion causes a considerable increase in the deformation rate. The stress – strain properties of a nanomaterial are determined by the relation between the yield point and the deformation rate; therefore, there should exist a critical cluster size corresponding to the maximum hardness of the nanomaterial. Yet another factor favouring an increase in the deformation rate is an increase in the diffusion coefficient with a decrease in the cluster size.

A nanostructure can be several times harder than coarse-grain materials. For instance, the hardness of metallic Ag, Cu, Pd, Se, Fe and Ni increased as the cluster size decreased to 4 – 6 nm according to the Hall – Petch law. However, if the nanocluster size is increased by annealing the same sample, the Hall – Petch law holds only for $d > 12 - 20$ nm.[81]

Superplasticity studies of metal oxides and ceramics are of great interest. Using the property of superplasticity, one can fabricate ceramic items of complex shape (*e.g.*, with internal cavities and variable curvature) with high accuracy. The superplasticity arises upon nanostructuring of materials; additionally, it increases if nanoparticles are dispersed within amorphous phase and the nanocrystalline grain boundaries are disoriented. Ceramics becomes superplastic at a grain size of less than 1 μm, and the grain size being retained with an increase in the temperature.[82]

High strength and superplasticity can be explained using the 'extremal' dependence of the defect concentration and, hence, the excess energy on the cluster size (see Fig. 28). Indeed, nanosystems composed of small clusters (size less than 10 nm, ignoring diffusion mobility) contain a low proportion of defects and dislocations and exhibit record hardness. At the same time, nanosystems built of clusters of intermediate size ($10 < d < 100$ nm) have the maximum defect concentrations, which predetermines the record plasticities. Summing up, superhard materials should be fabricated using nanosystems containing nanoclusters with $d < 10$ nm, whereas superplastic materials should be prepared involving nanosystems comprising nanoclusters with $10 < d < 100$ nm.

4. Electronic-optical properties

a. The conductivity of nanostructures

Transition from a bulk material to a nanomaterial involves separation of electron energy bands into subbands and individual electron energy levels. Transition from individual atoms and molecules to nanoclusters is accompanied by broadening of energy levels and formation of energy band structure. The appearance of discrete electron energy levels is due to limitation of the mean free path of electrons and characterises the quantum confinement effects in nanoclusters. As the cluster size decreases, the quantum confinement effects cause a decrease in the conductivity and the appearance of a Coulomb barrier to one-electron

transitions between the energy levels separated by kT and higher energies. This barrier is determined by the energy of electrostatic interaction of the tip of a tunnelling microscope used for studying the one-electron conductivity of clusters,

$$E = \frac{e^2}{2C}, \qquad (51)$$

where $C \sim r$ is capacitance of the cluster–tip system. This technique was employed to obtain stepwise $I-V$ curves for clusters of size of a few nanometres. Here, the number and height of steps increase as the cluster size and temperature decrease. Starting from certain critical size, reduction of the cluster size is accompanied by the loss of metallic properties and transition to dielectric molecular state.

One-electron transitions between clusters can be induced by, *e.g.*, thermal excitation. Using parameters of such transitions, it is possible to estimate the critical cluster size. Namely, assuming that $C = d_{cr}$ in relation (51) and the electronic transition energy $E_e \geqslant kT$, the critical cluster size equals $\sim 2-3$ nm at 300 K and ~ 200 nm at 4.2 K. The estimate of the critical cluster size at low temperatures (17 nm) is nearly an order of magnitude larger than the size of a colloidal cluster. This is due to the appearance of electron energy bands in these clusters and inapplicability of the one-electron transition model. This estimate also much exceeds the results obtained at high temperatures for mercury.

Weakening of the conducting properties is also due to the scattering of conduction electrons by the cluster surface, which is enhanced with a decrease in the cluster size and thus hampers separation of the contribution of one-electron conductivity and determination of the corresponding critical cluster size. The formation of nanostructures from nanoclusters is accompanied by retention of the factors favouring a decrease in the number of charge carriers and their scattering by the intercluster boundaries. Additionally, new factors appear, which can induce the tunnelling electron transitions between adjacent nanoclusters, appearance of charges, *etc*. Nanomaterials prepared by compaction of metal nanoclusters exhibit a noticeable decrease in conductivity compared to that of bulk materials. However, this method of fabrication of nanostructured conducting materials offers no prospects for the design of nanomaterials with controllable electrophysical properties. This requires the use of solid state chemistry and cluster chemistry methods.

The conductivity of three-, two- and one-dimensional nanostructures. Promising methods of application of nanocluster structures as conducting materials involve the assembly of different-dimension nanostructures with molecularly controlled conductivities.

Organised conducting or semiconducting structures of atomic or molecular crystals are well known. However, it is difficult to force nanoclusters to form nanocrystals under normal conditions. In the text above we have considered the possibility of organisation of (i) silver, silver sulfide, *etc*. nanocrystals obtained by reverse micellar technique or (ii) ordered nanostructures based on semiconductor nano-islands or (iii) nanowires on epitaxial surface. An efficient method of fabrication of organised three-dimensional conducting cluster structures is provided by the crystallisation of ligand-stabilised semiconductor chalcogenide clusters of particular size. An array of clusters separated by the ligand shells can be schematically represented by a sequence of potential wells containing ground-state and excited-state electron energy levels. In the ground state the valence electrons are localised. In the excited state, tunnelling through dielectric medium is possible. This shows that the conductivity can be controlled by varying the intercluster distance using different ligands (such ligands are called spacers).

As an example, we will consider the change in the conductivity (the Coulomb barrier) for Au_{55}-based molecular cluster crystals with spacers of different length (Fig. 29).[83] The crystals studied showed a noticeable decrease in the conductivity (increase in the Coulomb barrier) with elongation of the spacer. These data

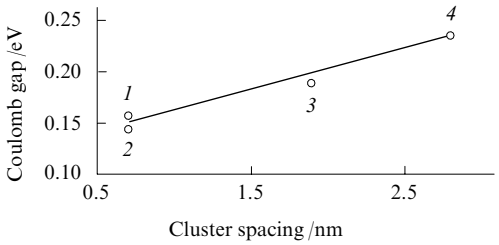
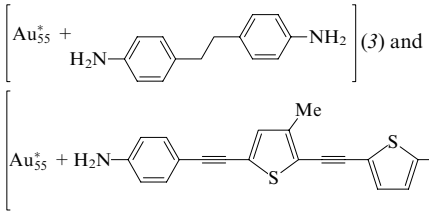


Figure 29. Correlation between cluster distance and Coulomb gap.[83] Open circles correspond to clusters (*1*, *2*) and systems (*3*, *4*):[83] $Au_{55}(PPh_3)_{12}Cl_6(Au_{55})$ (*1*), $Au_{55}(Ph_2PC_6H_4SO_3Na \cdot H_2O)_{12}Cl_6(Au^*_{55})$ (*2*),



(*3*) and

(*4*).

confirm the efficiency of the concept of directed change in the conductivity of a molecular cluster crystal by varying the spacer.

One-dimensional cluster nanostructures can play the role of quantum wires; a feasible example is provided by carbon nanotubes. A method of fabrication of quantum wires based on nanoporous anodised alumina (the preparation of the material was considered above) also seems to be quite promising. Technologically, both the pore size and the pore length can be controlled on the nanometre length scale.[84] Filling pores with clusters provides a nanowire distribution density of 10^9-10^{10} per cm^2 and separation by dielectric alumina matrix. The main problem in fabricating such nanowires, that is, breakdown during the growth, can be solved by soaking the membrane with clusters *in vacuo* or using electrophoresis. A drawback of the vacuum technique consists in evaporation of the solution containing clusters, which produces voids in the membrane channels. In the case of electrophoresis one side of the membrane contacts a metal, *e.g.*, gold or aluminium, thus acting as a cathode to which clusters move. This allows the whole channel to be filled, but breaks are also possible due to large membrane thickness. For instance, a membrane 10 μm thick with channels 10 μm long should contain at most ~ 4000 clusters of diameter 2.5 nm per channel, but this is difficult to reach. At the same time a membrane a few micrometres thick is too brittle. Exposure of a thick membrane to ion irradiation makes it thinner (up to 100 nm) and enables fabrication of continuous nanowires.[85]

b. Optical properties

Metallic nanoclusters and nanostructures. The optical properties of metal nanoclusters are due to plasmon vibrations of electrons in metals. The absorption spectra of small clusters exhibit an intense broad band that is absent in the spectra of bulk metals. This band is due to co-operative excitation of conduction electrons. Absorption in the visible region is responsible for, *e.g.*, unique colour grade of dilute colloidal sols of noble, alkali and rare-earth metals.

The nature of the plasmon peak is as follows. The electric field of incident radiation displaces the conduction electrons in the cluster relative to the charged core. The displacement is co-operative in character and all electrons move with the same phase. As a result of electron displacement, a force arises, which tends to return electrons to the equilibrium positions. As for typical oscillator, this force is proportional to the displacement; therefore, one can consider the eigenfrequency of collective electronic vibrations in the cluster. When the eigenfrequency of electrons becomes equal to the frequency of the external field, a resonance effect should be observed. Quantum mechanics treats

the collective motion of electrons in terms of excitation quanta called plasmons characterised by the energy $\hbar\omega$ and the resonance frequency ω_0 corresponding to the eigenfrequency of collective electronic vibrations (usually, 10^{14} s^{-1}).

The optical properties of colloid clusters are correctly described in the framework of the classical Mie theory,[86,87] which considers the optical properties of spherical metallic particles in a dielectric matrix. Using this theory, one can describe the optical resonance due to collective excitation of electron plasma. If the cluster size is much less than the emission wavelength (λ), the absorption line in the vicinity of resonance has a Lorentzian shape and is characterised by the position of the resonance maximum, $\hbar\omega_0$, the width Γ and the absorption section

$$\sigma = \frac{ne^2}{mc\Gamma\varepsilon_0}\left[\frac{\omega^2}{\omega^2-\omega_0^2}+(\omega\Gamma)^2\right], \tag{52}$$

where n is the electron distribution density, ε_0 is the dielectric constant, m_e is the effective mass of the conduction electron and c is the speed of light.

In case of spherical monovalent metal particles the equation for the resonance frequency has the form

$$\omega_0^2 = \frac{e^2}{4\pi\varepsilon_0 r_s^3}, \tag{53}$$

where r_s is the Wigner – Seitz radius.

The corresponding plasmon frequency for bulk metal is given by

$$\omega_p^2 = \frac{e^2}{4\pi\varepsilon_0 \upsilon}, \tag{54}$$

where $\upsilon = (4/3)\pi r_s^3$. Then the resonance frequency of a metallic sphere should be

$$\omega_0^2 = \frac{\omega_p^2}{\sqrt{3}}. \tag{55}$$

The resonance linewidth is

$$\Gamma_{r0} = 2\varepsilon_2(\omega)\left[\left(\frac{\partial\varepsilon_1}{\partial\omega}\right)^2+\left(\frac{\partial\varepsilon_2}{\partial\omega}\right)^2\right]^{-1/2}, \tag{56}$$

where $\varepsilon_1(\omega)$ and $\varepsilon_2(\omega)$ are the real and imaginary parts of the dielectric permittivity of the cluster, respectively.

It should be noted that the Mie theory predicts no size effect. Nevertheless, the results of numerous measurements show that ω_0 and Γ depend on the cluster size. For small clusters, an important role should be played by collisions between electrons and the cluster surface (mean free path of electrons is $\sim$20 nm). In this case one has

$$\Gamma_r = \Gamma_{r0} + \frac{2\omega_0^2}{\omega^3} v_F\left[\left(\frac{\partial\varepsilon_1}{\partial\omega}\right)^2+\left(\frac{\partial\varepsilon_2}{\partial\omega}\right)^2\right]^{-1/2}\frac{A}{r}, \tag{57}$$

where v_F is the velocity of an electron on the Fermi surface and A is a constant. Clearly, this relation is invalid for small cluster sizes, *i.e.*, at $r \to 0$. Indeed, the metallic state typical of bulk metal and large clusters will disappear upon localisation of electrons on particular atomic levels and upon transition from the conduction and valence bands to individual localised energy levels. In this case the concept of plasmon resonance should be replaced by the resonant electron absorption between certain electron energy levels. Following this (classical) treatment procedure, it is impossible to obtain a critical cluster size, but this parameter can be determined from experimental data.

Good agreement between the calculated and experimental resonance frequencies and spectral linewidths was reported.[88] A relatively narrow line of silver clusters is due to a simpler structure of the Ag conduction band compared to the Au and Cu conduction bands characterised by a broad interband transition above 2 eV for bulk metal. Narrow plasmon resonance lines of silver clusters suggest that they can be used in optical materials for characterisation of the interaction between the clusters and the environment and for studying the surface chemistry effects. Note that narrow spectral lines similar to the silver cluster lines were observed for the plasmon resonances of alkali metals, which was associated with the shell-type cluster structure ('jellium model') and with the fact that only s-electrons are involved in resonance (as in case of silver). However, the alkali metal clusters are extremely reactive and seem to be inappropriate for fabricating optical nanomaterials.

Figure 30 illustrates the size effects for silver clusters in argon matrix. Here, it is possible to determine the critical size for the onset of plasmon vibrations.

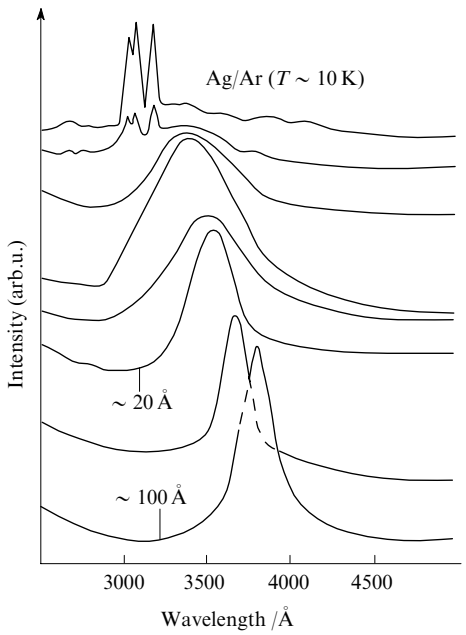


Figure 30. Absorption spectra of surface plasmons in silver clusters in argon matrix. The cluster size decreases upward.[88]

As the cluster size decreases, the resonance frequency experiences a clearly seen shift towards the short-wavelength region ('blue' shift) up to the appearance of lines corresponding to individual monomers, dimers, trimers, *etc.* and the spectral lines are broadened. The following empirical dependences for the resonance energy and the line half-width were obtained based on the analysis of experimental data:

$$\hbar\omega = 3.21 + 0.58\frac{1}{d}, \tag{58}$$

$$\Gamma = 0.04 + 0.59\frac{1}{d}, \tag{59}$$

where d is the average cluster diameter (in nanometres); here $\hbar\omega$ and Γ are given in electronvolts.

Comparison of experimental spectra showed that if the cluster size is about 1 nm and the number of silver atoms in the cluster is at most ten, a number of resonance lines is observed. The critical size of silver clusters for plasmon resonance was estimated from the characteristics of these lines at $\sim$1 nm.

Semiconductor nanostructures and nanodevices. Semiconductor clusters also exhibit noticeable size effects, namely, a shift of the absorption frequency of optical photons and an increase in the oscillator strength, which are already used in various nanomaterials and nanodevices, *e.g.*, light-emitting diodes or tunable lasers. As the cluster size decreases, the electron excitation bands are shifted to the high-energy region and the oscillator strength (absorption intensity) is concentrated on a few transitions. These

changes associated with the change in the character of transitions between the valence band and the conduction band for bulk material give rise to a line spectrum of the cluster. The transition energy is given by

$$E \approx \frac{1}{r^2},$$

where r is the cluster radius. According to this expression, the transition energy increases as the cluster size decreases. This expression can be derived from the uncertainty relation

$$\Delta p \Delta x \geqslant h$$

(p is the momentum and x is the coordinate) assuming $\Delta x = r_{cr}$.

For semiconductors, the absorption and emission of energy are related to the excitation of an electron and to the formation and decomposition of an exciton (hydrogen-like bound state of a conduction electron and a positively charged hole). The equation for the energy of exciton excitation has the form

$$E_n = \frac{h^2 n^2}{3 r^2 m_{ef}}, \qquad (60)$$

where n is an integer and m_{ef} is the effective mass of the exciton.

The dependence of the absorption coefficient of CdS colloid clusters of size from 6.4 to 48 nm on the wavelength of incident radiation is shown in Fig. 31. The change in the absorption or luminescence wavelength can be due to the change in the intercluster interactions,[89] photochromic and electrochromic effects. The dependence of the emission wavelength on the cluster size can be employed in, *e.g.*, light-emitting diodes or tunable lasers.

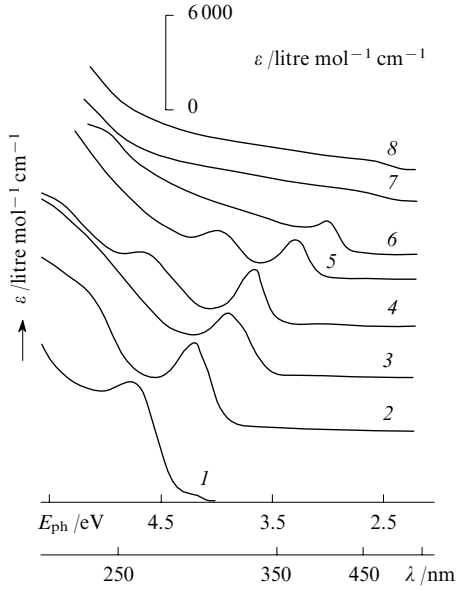


Figure 31. Optical absorption coefficients of CdS clusters of different size plotted *vs.* photon energy.[89]
Cluster size/nm: 6.4 (*1*), 7.2 (*2*), 8.0 (*3*), 9.3 (*4*), 11.6 (*5*), 19.4 (*6*), 28.0 (*7*) and 48.0 (*8*).

As an example, we will consider CdSe-based light-emitting diodes with tunable colour of the emission.[90] The light-emitting cell has the following structure. CdSe nanoclusters were distributed within a thin surface layer of a luminescent polymer (poly-*p*-phenylenevinylene), the polymer was synthesised on ITO substrate (hole conductor). CdSe nanoclusters were coated with a magnesium/aluminium film for injection of electrons into the CdSe nanoclusters. Applying a voltage to this system causes electroluminescence. The wavelength of emission can be varied by changing the cluster size.

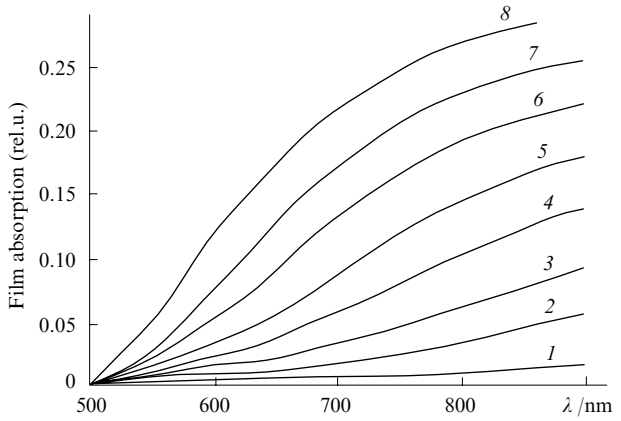


Figure 32. Electrochromic effect in nanostructured WO_3 at different voltage applied: 0 (*1*), −0.2 (*2*), −0.3 (*3*), −0.4 (*4*), −0.5 (*5*), −0.6 (*6*), −0.7 (*7*) and −0.8 V (*8*).[91]

Nanostructured tungsten oxide WO_3 as well as TiO_2/WO_3, WO_3/V_2O_5 and WO_3/MoO_3 compositions also possess electrochromic properties.[91] The light absorption in tungsten oxide films at different voltages is shown in Fig. 32. At positive potentials (0 V or higher), no absorption occurs, but an increase in the negative potential causes an increase in the IR absorption. At positive potentials, the films are blue, whereas at negative potentials (starting with −1.2 V) they turn brown.[91]

Yet another example is as follows. Using nanoclusters (quantum dots), it is possible to fabricate tunable lasers in which the wavelength of emission is varied by changing the nanocluster size. This requires fabrication of ordered nanostructures from clusters with narrow size distribution, dispersed in semiconductor solid solutions. Semiconductors can initiate population of higher electron energy states by injecting electrons and holes into nanoclusters. Transition of nanoclusters to the lowest energy state as a result of relaxation should cause emission of photons with the same wavelength, which can be focussed to produce a coherent laser beam. A scheme of a laser based on this principle is shown in Fig. 33.

The use of nanoclusters in optical devices requires meeting certain conditions related to the cluster size. The minimum critical size of a nanocluster is determined by the condition for the presence of at least one electron energy level and is characterised

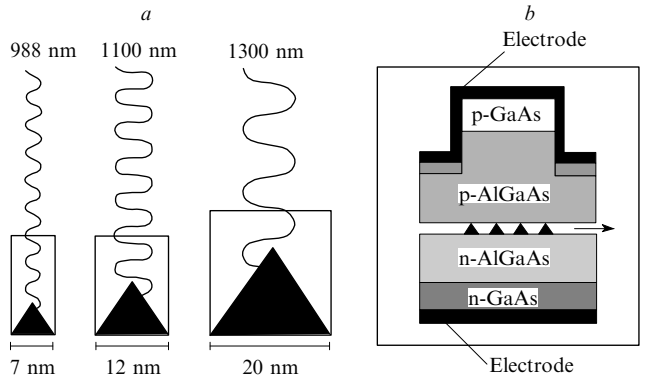


Figure 33. Scheme of laser based on InAs nanoclusters.
Change in photon wavelength with a change in the nanocluster size (*a*) and scheme of a device including InAs nanoclusters (triangles), a medium consisting of an electron injector n-AlGaAs/n-GaAs (−), hole injector p-AlGaAs/p-GaAs (+) and electrodes (*b*); an arrow shows the output of light emission.

by an energy difference ΔE_c in the conduction band, corresponding to emission in the visible region. For a rectangular potential well, the electron level exists if ΔE_c exceeds the following value

$$\Delta E_c^0 = \frac{\hbar^2}{2m_e^*}\left(\frac{\pi}{D_{min}}\right)^2 \equiv \Delta E_1, \quad (61)$$

where m_e^* is the effective mass of electron and ΔE_1 is the energy of the first level in the rectangular potential well of width D. Assuming $\Delta E_c = 0.3$ eV for related semiconductors, the nanocluster diameter should be at least 4 nm.

The maximum critical size of a nanocluster is determined taking into account the fact that the energy difference between the cluster levels becomes comparable with the thermal energy, which causes an increase in the population of higher levels

$$kT \leqslant E_2 - E_1, \quad (62)$$

where E_2 and E_1 are the energies of the first and second energy levels related to the size quantisation of the nanocluster. In practice, it is sufficient that

$$kT \leqslant E_1. \quad (63)$$

The maximum cluster sizes determined from this condition for various GaAs and InAs compositions lie between 12 and 20 nm.

Porous silicon. The properties of porous silicon differ from those of crystalline silicon. These are, *e.g.*, unusual chemical properties of the surface, biocompatibility and optical properties related to the quantum confinement effects.[92]

Porous silicon is obtained by etching the surface of crystalline silicon. The material consists of bent silicon wires of nanometre sizes. Formally, radiative transitions between the valence band and the conduction band of crystalline silicon are symmetry forbidden. Nevertheless, transitions do occur, but they are photon assisted and therefore the rate of radiative transitions is low. Because of this, silicon is not used for generation of optical signals. Porous silicon exhibits intense photoluminescence, which was initially associated with possible violation of selection rules in the nanosystem without translational symmetry. The quantum confinement effects do play the key role in the mechanism of onset of photoluminescence upon a change in the intensity ratio of radiative and nonradiative transitions. The intensity of radiative transitions somewhat increases, but the intensity of nonradiative transitions mainly decreases; in particular, the probability of three-body Auger processes associated with electron emission after absorption of light dramatically decreases compared to crystalline silicon.

Specific optical properties of porous silicon can be used for fabrication of optical sensors for, *e.g.*, detecting changes in the reflection coefficients upon adsorption of various molecules. For instance, by measuring the changes in the wavelength with a Fabry–Perot interferometer it is possible to detect small amounts of substances in air at the porous silicon–bulk silicon interface after diffusion of gas through a membrane (Fig. 34). The radiation reflected from the surface of porous silicon and the porous silicon–bulk silicon interface forms an interference spectrum. Adsorption of various molecules on the silicon membrane causes the interference fringes to shift. The magnitude of the shift can be measured in some way. The results of a sorption study of air containing 1.7% of ethanol at different thickness of porous silicon layer are shown in Fig. 35.[93]

The lowest ethanol concentration that can be determined by this sensor was 250 ppm. It is important that such devices demonstrate good reproducibility of results and can be efficiently reused and that the parameters of porous silicon can be varied over a broad range by etching, thus allowing various gas components to be detected and studied. Additionally, the interference sensor permits temporal separation of binary mixtures (*e.g.*, ethanol and acetone) in air, because the mixture components have different reflection coefficients, which depend on the diffusion and adsorption rates. This is to some extent similar to gas chromatography, however the interference sensor offers the advantage consisting in combining separation and detection.

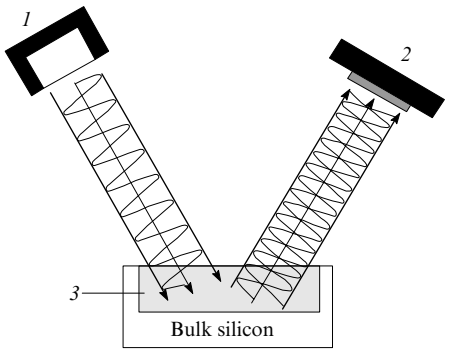


Figure 34. Scheme of a sensor involving an interferometer based porous silicon.[93]
Incident radiation (*1*), detector (*2*) and porous silicon (*2*).

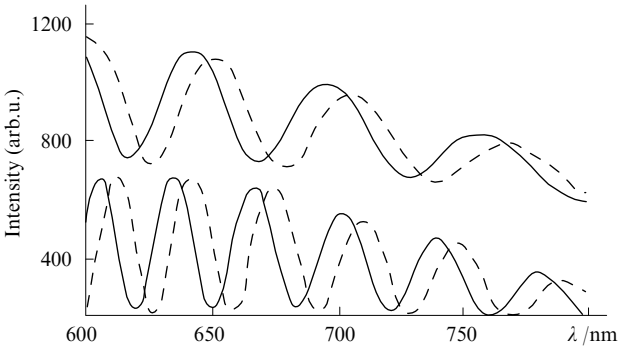


Figure 35. Reflectance spectra of porous silicon samples of different thickness before (solid line) and after (dashed line) sorption of ethanol (1.7%)–air mixture.[93]

Yet another original field of application of porous silicon consists in initiation of a local explosion in a pore.[94] The effect is probably due to the hydrogenated surface of porous silicon and to the fact that the reaction was carried out in a nanoreactor, which accelerates the process. For instance, detonation of freshly prepared porous silicon soaked with aqueous $Gd(NO_3)_3$ solution can be achieved by using a mechanical or chemical ignition system. The colour temperature of the microexplosion was estimated at 2000 K, which makes it possible to carry out a microscopic analysis of metals based on their emission spectra. It is possible to initiate microexplosions of porous silicon after condensation of oxygen in a pore. This is achieved by exposure to UV light or by simply scratching.[95] The power of a microexplosion is 12 kJ g^{-1} and the energy released is 4.2 kJ g^{-1}. In addition to atomic emission spectroscopy and elemental analysis the microexplosions can be used in microelectromechanical systems, as energy sources for electronic systems and in self-destroying computer security networks.

Photonic crystals. Photonic crystals are formed from dielectric or semiconductor particles of size comparable with the wavelength of a photon (hundreds of nanometres for the visible region). Therefore, in this case one deals with the diffraction processes and conditions similar to those for scattering of X-rays by the atomic crystal lattice. This in turn causes manifestation of coherent effects in the scattering and absorption of emitted radiation. These effects are rather sensitive to the energy and direction of propagation of photons. For instance, photonic crystals have a periodically varied reflection coefficient, which makes it possible to change the optical properties of materials. One-dimensional structures are used as interference filters; how-

ever, two- and three-dimensional crystals are of greater interest. The dispersion curves obtained for photon scattering by two-dimensional phononic crystals assembled from nanocylindres are similar to the electron dispersion curves. By analogy with such notions as electron valence, forbidden and band conductivity, the dielectric band, photonic gap and air gap were introduced.[96] Removal of a row of cylinders in the photon crystal causes the appearance of an energy level in the photonic gap similar to a p- or n-level in the electron energy gap. By removing a cylinder and thus creating a void or by changing the cylinder size one can vary the photon frequency *via* a change in the nanocluster size (Fig. 36).

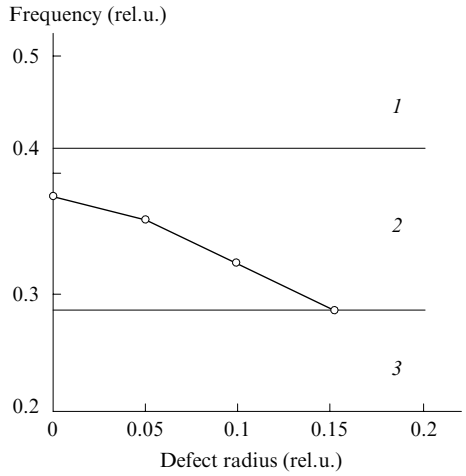


Figure 36. Frequency dependence of localised states within the photonic band gap.
Air band (*1*), photonic band gap (*2*) and dielectric band (*3*).

The energy and dispersion spectra of three-dimensional photonic crystals are also characterised by the presence of photonic gaps similar to the forbidden bands in the electron energy and dispersion spectra in atomic crystals. Taking into account this fact, one can suggest the existence of a photonic gap with the frequencies at which the propagation of a photon inside the crystal is impossible and the photon experiences elastic reflection from the nanocrystaline layer. This offers prospects for the synthesis of nanomaterials with variable optical properties for the use in light guides and tunable lasers and for the design of devices for integrated electronic networks based on optical integrated systems. Photons propagate in dielectrics at higher frequencies compared to electrons moving in conductors and can be much more informative. Fibre optical systems operate at THz frequencies (*cf.*, GHz frequency range for conventional electric current systems).

Photonic crystals with the photonic gap are fabricated by various methods. One of them involves self-organisation of spherical particles of a critical submicron size (hundreds of nanometres) in a colloid solution to give a face-centred lattice obeying the closest packing principle, which limits further growth of particles. This procedure was used to obtain an artificial opal with inclusions of monodisperse silica spheres. However, this crystal is characterised by unstable photonic gap, which is easily destroyed in the presence of various defects and imperfections. The artificial opal is used as a template for the preparation of semiconductor material. Namely, infiltration of the nanocrystalline opal with silicon followed by removal of the template results in nanocrystalline inverted opal (*cf.* nanosized reverse micelle structure) with an ordered void structure (Fig. 37).

According to calculations, a semiconductor with rather high reflection coefficient (>2.85) should have a photonic gap. This was experimentally found in a silicon photonic crystal.[98] In this connection it is of great interest to fabricate GaS-, InS- or GaP-based photonic crystals capable of emitting intense light or to create ordered voids in a diamond structure that, according to calculations, can have a wider photonic gap and be less dependent on the defects and disorder.

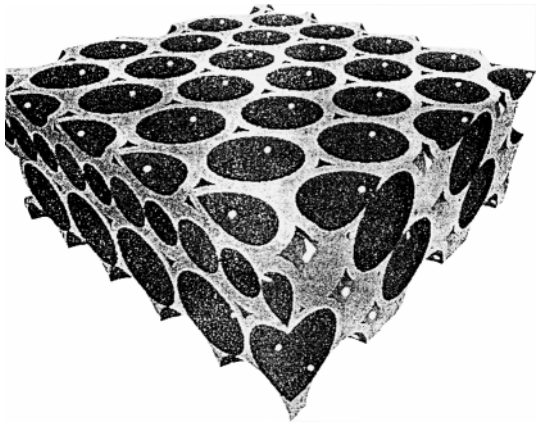


Figure 37. Cross-sectional view through an incompletely infiltrated opal nanocrystal. After etching out the SiO_2 spheres, the incomplete infiltration of silicon (shown in gray) results in additional triangular (or diamond-shaped) pores.[97]

5. Magnetoelectric and magnetic properties

a. Giant magnetoresistance effect

The giant magnetoresistance (GMR) effect represents a great decrease (to 1000%) in the resistance of the nanocluster material in a magnetic field. For comparison, the magnetoresistance of bulk samples changes only slightly under identical conditions (*e.g.*, the resistance of permalloy, 80% Ni – 20% Fe, increases only by 3%). The GMR effects were observed in studies of the magnetic properties of various metallic and oxide nanosystems. The mechanisms of GMR origination for nanocrystalline metals and metal oxides are different.

Nanocluster metallic materials exhibiting the GMR effect (magnetic clusters) are prepared by dissolving nanoclusters of one metal (*e.g.*, iron or cobalt) in the matrix of another metal possessing high conductivity (*e.g.*, copper or silver); the two components should be poorly soluble in each other. In a nanosystem comprising a conducting metallic matrix and magnetic clusters, the conduction electrons of the matrix are scattered by the magnetic moments of the clusters. The clusters are sufficiently small and can possess superparamagnetic properties. However, for the conduction electrons moving at the Fermi velocity, the magnetic moments of the clusters are blocked, because the magnetisation measuring times (~ 100 s) are much longer than the characteristic time taken by an electron to pass through the sample ($\sim 10^{-9}$ s). The electronic structure of the metallic matrix has marked effect on the magnetic properties of clusters.[99]

If electrons in metals are scattered prior to changing the directions of the spins, the relative orientation of the magnetic moments of the clusters affects the rate of scattering and conductivity. Once a magnetic field is applied to the sample, the direction of the magnetic moments changes, this causes their interaction with the conduction electron and, hence, a change in the conductivity. The magnitude of the GMR effect (and the GMR effect itself) is determined by the ratio of the electron free path to the distance between the neighbouring magnetic clusters, which depends on the concentration of the metal nanoclusters in the matrix. When the concentration is low and, correspondingly, the free path is long, an electron experiences numerous scattering events before it enters into interaction with the magnetic cluster. In this case the direction of the magnetic moment of the cluster has no effect on the electron scattering and no GMR effect is observed. At high concentration of the metal clusters, the mag-

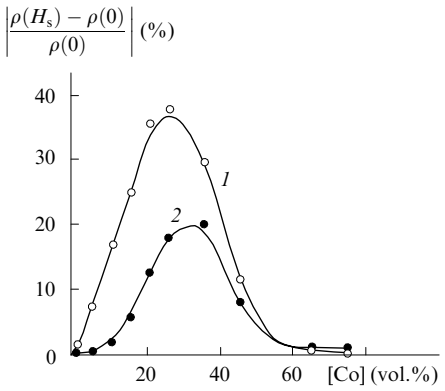


Figure 38. Change in magnetoresistance $|[\rho(H_s)-\rho(0)]/\rho(0)|$ of Co–Ag nanosystems with different cobalt concentrations at 5 (*1*) and 300 K (*2*).[99]

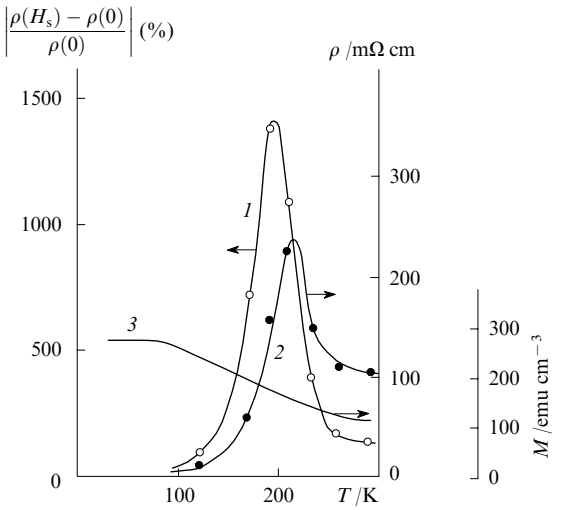


Figure 39. Parameters $|[\rho(H_s)-\rho(0)]/\rho(0)|$ (*1*), ρ (*2*) and M (*3*) of $La_{0.67}Ca_{0.33}MnO_x$ ceramics plotted *vs*. temperature.[100]

netic clusters interact with one another and are involved in the percolation processes, which eliminates the GMR effect.

An optimum situation is observed for the Co–Ag nanosystem.[99] As the cobalt concentration changes from 15% to 40%, the GMR effect is observed. The change in the relative GMR effect *vs*. the cobalt concentration in the sample at different temperatures are shown in Fig. 38. The maximum GMR effect was observed at a cobalt concentration of about 20%, which was associated with the critical size of cobalt clusters in the silver matrix.

The GMR effect increases as the temperature decreases. The mechanism of the effect can be explained using the two-current model, according to which electron scattering on the cluster magnetic moment in a disordered nanosystem is possible in two directions, (*e.g.*, up or down). In a nanosystem ordered by an external magnetic field, one direction, namely, that along the field, has a lower resistance than the other direction; this results in an overall decrease in the resistance by a value of $\Delta\rho$. The $\Delta\rho$ value correlates with the cluster size: $\Delta\rho \sim 1/d$. This indicates that the GMR effect is determined by the ratio of the surface area of the magnetic clusters to the volume of the clusters and that it is the cluster–matrix interface where the spin-dependent electron scattering occurs.

Small cobalt clusters possess the properties of superparamagnetic materials and the direction of the magnetic moment of a cluster can easily be changed in an external magnetic field or by the interaction with conduction electrons. However, this interaction can occur if the time of magnetic moment fluctuations exceeds the travel time of the conduction electrons. The minimum cluster size corresponding to the onset of the GMR effect can be evaluated from Eqn (29) for the superparamagnetic relaxation time. The cluster size estimates obtained assuming $\tau_{cr} \geqslant \tau_0$ and substituting $K = 10^6$ J mol^{-3} for cobalt are $\sim$4–8 nm at room temperature and $\sim$1 nm at 4.2 K.

In ceramic materials, the GMR effect is observed in a narrower temperature range.[100] The temperature dependences of changes in the magnetoresistance $[|\rho(H_s)-\rho(0)/\rho(0)|$ (%)], resistance (ρ) and magnetisation (M) for $La_{0.67}Ca_{0.33}MnO_x$ are shown in Fig. 39.

The maximum value of the GMR effect is $\sim$1300% at $T = 200$ K. In the region 100–200 K, a metal–semiconductor transition occurs and the magnetisation increases. The appearance of the GMR effect can also be explained by the influence of superparamagnetism in this temperature range. In the temperature interval where the GMR is observed, the Mössbauer spectra exhibit a superparamagnetic doublet which is due to the appearance of nanosized regions of iron-doping induced fluctuations of the magnetic moment of ceramics.[101] The characteristic time of thermal fluctuations of the magnetic moment is also determined using expression (29); the estimate of the critical nanocluster size corresponding to the onset of the GMR effect in ceramics is $\sim$2–4 nm at $K = 10^5$ J m^{-3}. A decrease in temperature leads to reduction of the GMR effect, extension of the fluctuation regions and disappearance of superparamagnetism. This effect can be treated as the percolation effect for metallic matrix. The existence of superparamagnetic fluctuations of the ceramic matrix was also confirmed by inelastic neutron scattering data.[102]

Based on this, one can assume that the GMR effect in the region of the semiconductor–metal transition of the ceramic material is due to the appearance of fluctuating magnetically ordered nanodomains. The nanodomain size increases as the temperature decreases; this is accompanied by an increase in the superparamagnetic relaxation time and in the time taken to attain the magnetically ordered ferromagnetic state. The temperature interval of the magnetic transition spans tens of degrees; the GMR effect observed in the same temperature range is due to the change in the scattering of conduction electrons caused by the change in the relaxation time of the magnetic moment, in the distance between fluctuating clusters and in the cluster size (no ferromagnetic nanoblocks at temperatures below the phase transition temperature and no metallic conductivity at high temperatures).

b. Quantum magnetic tunnelling

Quantum tunnelling transitions in cluster molecular crystals are accompanied by discrete changes in the magnetisation of nanoclusters and of the whole nanocrystal. This was observed for a cluster single crystal $[Mn_{12}(AcO)_{16}(H_2O)_4O_{12}]\cdot AcOH\cdot 4H_2O$ built of identical Mn_{12} clusters with acetate ligands.[103] This nanostructure is characterised by a stepwise character of the magnetisation curve (Fig. 40).

The hysteresis loop consists mainly of vertical and horizontal portions. In horizontal portions, the relaxation time of the magnetic moment exceeds the measurement time ($t_m \sim 600$ s); in the slope portions, the relaxation time is similar to the measurement time. This leads to a number of minima in the plot of the superparamagnetic relaxation time τ on external magnetic field, which are associated with the steps in the hysteresis loop. Experimentally found critical H_0 values corresponding to the steps in the hysteresis loop change from 0 to 2.64 T with an increment of

$$\Delta H = H_{n+1} - H_n = 0.44 \text{ T}.$$

Here, the relaxation time of the magnetic moment of the cluster changes in a stepwise manner. These effects can be explained with allowance for the electronic structure and tunnelling transitions between the electron energy levels of molecular cluster Mn_{12}. The cluster core has a tetragonal two-layer structure in which the

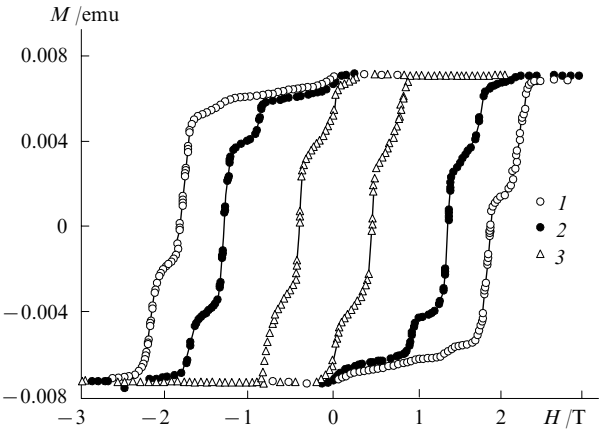


Figure 40. Magnetisation curves of Mn_{12} acetate cluster single crystal at different temperatures.[103]
Temperature /K: 1.77 (*1*), 2.10 (*2*), 2.64 (*3*).

Mn^{4+} atoms form the inner cubane cage Mn_4O_4 with the spin $S = 3/2$, and eight external Mn^{3+} atoms with the spin $S = 2$ form the outer layer. The ground ferrimagnetic state of the cluster with the collective spin $S = 10$ is stabilised by internal exchange interactions. The energy of axially symmetric crystallographic anisotropy

$$\Delta E = DS^2$$

causes the ground spin state to split into two levels with $S_z = \pm 10$ and a crystal field constant $D = 0.61$ T. For a thermally activated process at $kT \gg \Delta E$, off-resonance spin transitions occur with the probability and transition times characteristic of larger clusters. At low temperatures, quantum tunnelling of the projection of the magnetic moment is possible if the energy levels of the clusters with $M = S_n$ and $M = -S_n$ in an external magnetic field coincide. Calculations using the relation

$$\Delta H = \frac{D}{g\mu_B} = 0.44 \text{ T},$$

where g is the gyromagnetic ratio and μ_B is Bohr magneton give $D = 0.6$ T.

Thus, the relaxation of the magnetic moment of the cluster accelerates when tuning by the magnetic field results in coincidence of the energy levels of all clusters in the nanostructure. This effect corresponds to quantum tunneling in the whole nanostructure. Such clusters are treated as molecular magnets with a colossal writing density, which can be used for information storage and retrieval. Owing to multilevel tunneling, such nanodevices can be used in quantum computers in order to achieve a considerable increase in the storage capacity and performance.

c. Magnetic phase transitions

The magnetic phase transitions are classified depending on the type of changes in the magnetisation or in the character of magnetic ordering near the critical temperatures (Curie point for ferromagnetics or the Néel points for anti- and ferrimagnetics). Sharp (stepwise) and gradual changes in these characteristics correspond to the first- and second-order transitions, respectively. Changes in the unit cell volume or the thermal effect in the case of a first-order phase transition can be either significant or not. Most bulk magnets undergo second-order phase transitions, but a number of substances undergo a first-order phase transition on going from the magnetically ordered to the paramagnetic state and upon change in the type of magnetic ordering. Examples are provided by MnAs (ferromagnet → paramagnet), MnO, UO_2, Eu (antiferromagnet → paramagnet) and α-Fe_2O_3 (antiferromagnet → weak ferromagnet).[104]

When studying nanoclusters and nanostructures, the magnetic phase transitions become of particular importance due to manifestation of versatile new (compared to the case of bulk materials) factors affecting the character and mechanism of transitions (size effects, surface effect, intercluster and nanoclusters–matrix interactions, effect of magnetic fields, *etc.*). Specific features of magnetic transitions can be used as a new tool of studying the structure of nanosystems and design of novel nanomaterials and nanodevices.

Nanoclusters and nanomaterials also undergo the first- and second-order magnetic phase transitions. Similarly to most bulk magnets, the second-order magnetic phase transitions of metal and metal oxide clusters are characterised by the Langevin dependences of the magnetisation and by gradual disappearance of the magnetic order and spontaneous magnetisation near T_C or T_N. Nanoclusters of size less than 10 nm possess the properties of superparamagnets, which leads to efficient reduction of T_C or T_N.

Unlike bulk metal oxides characterised by second-order magnetic phase transitions, the corresponding oxide nanoclusters undergo the first-order transitions accompanied by abrupt loss of spontaneous magnetisation at a particular temperature or by transition to the paramagnetic rather than superparamagnetic state as the cluster size becomes less than a critical size.[36]

When observing and studying the first-order magnetic phase transitions of nanoclusters, the problem is first of all to distinguish them from the superparamagnetic behaviour. In most cases, a scatter of cluster size occurs. Additionally, nanosystems that do not form cluster crystals are characterised by scatter of intercluster interactions. These factors hamper the detection of the first-order magnetic phase transitions of nanoclusters and nanostructures by the magnetisation measurements that provide some averaged magnetic characteristics. In this connection, one should expect a high efficiency of spectroscopic methods (in particular, Mössbauer spectroscopy with characteristic times of 10^{-7}–10^{-10} s) that permit separate characterisation of the magnetic and non-magnetic fractions in the same sample.

Magnetic phase transitions manifest themselves differently in systems including isolated clusters (or clusters with weak intercluster interactions) and in nanostructures comprising clusters of size at most 100 nm with strong intercluster interactions. The reasons and mechanisms of the magnetic phase transitions in these cases are different. In this connection, it is appropriate to consider the first-order magnetic phase transitions in (i) nanosystems including isolated small nanoclusters of size less than 10 nm and (ii) nanostructures composed of larger clusters (up to 100 nm in size) characterised by strong intercluster interactions, in which magnetic transitions associated with co-operative change in the nanostructure can occur.

Nanosystems with isolated clusters. The magnetic ordering of a cluster is a co-operative phenomenon. For instance, iron atoms have a magnetic moment and possess paramagnetic properties at all temperatures. This holds for low concentrations of iron atoms present in non-magnetic (*e.g.*, polymer) matrices. A cluster comprising a few (at most ten) iron atoms is characterised by exchange interaction; however, no spontaneous magnetisation appears in this case owing to thermal fluctuations and fast spin–spin relaxation. The number of magnetic moments and, correspondingly, the cluster size should be large enough that the total exchange energy be higher than the energy of thermal fluctuations, which is of the order of kT. Using quantum-statistical methods, one can specify the energy level scheme for a cluster, calculate the total exchange energy and compare it with the energy of thermal fluctuations. This makes it possible to determine the critical cluster size corresponding to the onset of spontaneous magnetisation and magnetic ordering.

However, the character of exchange interactions and, hence, the critical cluster size will be affected by various factors, *e.g.*, the state of the cluster surface, intercluster interactions, cluster shape, *etc*. Therefore, carrying out accurate critical-size calculations is a rather complicated task. Meanwhile, the estimates of the quantum

confinement effects made in considering the electrical, optical, thermal and other properties can also be applied for the determination of the critical size of a magnetic cluster. Indeed, assuming that

$$\Delta p \Delta x = \Delta p d_{cr} \approx \hbar,$$

where p is the momentum, x is the coordinate and d_{cr} is the critical size (diameter) of the cluster, one has

$$\Delta p = \frac{\hbar}{d_{cr}},$$

and the uncertainty of the electron energy, exchange interaction or magnon due to quantum confinement effects is given by

$$\Delta\varepsilon \approx \frac{(\Delta p)^2}{2m} \approx \frac{\hbar}{2m}(d_{cr})^2.$$

Assume now that this value equals the energy of exchange interaction, which is mainly responsible for the onset of magnetic ordering, *i.e.*, $\Delta\varepsilon \approx kT_C$, where T_C is the Curie temperature of bulk material. Then, the critical size (in metres) can be determined from a simple relation

$$d_{cr} \sim 2 \times 10^{-8} T_C^{-1/2}. \quad (64)$$

For $T_C \sim 500 - 1000$ K, one gets $d_{cr} \approx 1$ nm. This is the critical size of a magnetic cluster. Smaller clusters lose the magnetic ordering and undergo a transition to a magnetically disordered (*e.g.*, paramagnetic) state at any temperature. This is also the minimum size of a superparamagnetic cluster (the upper bound is ~ 10 nm and depends on many parameters, *e.g.*, the energy of magnetic anisotropy, temperature, measurement time, *etc.*). Thus, all clusters of size $d < d_{cr}$ should be in the magnetically disordered state.

The critical cluster size can also be determined using the thermodynamic theory of magnetic phase transitions in nanoclusters.[105, 106] This theory predicts the first-order magnetic phase transitions of nanoclusters and the change in the character of the phase transition depending on the cluster size.

The first-order magnetic phase transitions can occur in bulk samples characterised by a change in the unit cell volume on transition from the magnetically ordered to a non-magnetic state, *i.e.*, in the materials, possessing magnetostriction and exhibiting hysteresis-type temperature dependences of the specific volume and magnetisation.[107]

The Curie (Néel) temperature depends on the change in the volume as follows:

$$T_C = T_0\left(1 + \beta\frac{V - V_0}{V_0}\right). \quad (65)$$

Here T_0 is the Curie temperature of the substance with uncompressed crystal lattice, β is the magnetostriction constant of the substance, V and V_0 are the molar volumes of the substance in the magnetically ordered (compressed) and in the non-magnetic (paramagnetic) states, respectively.

The first-order magnetic transitions of nanoclusters are realised using a dependence similar to expression (65).

The equation for the change in the Gibbs free energy density upon transition of the cluster from the magnetically ordered to the non-magnetic state is written with allowance for the change in the cluster volume as a result of magnetostriction, compressibility under pressure

$$P = \frac{2\alpha}{r}$$

due to the surface tension of the cluster of radius r

$$\Delta G = -\frac{1}{2}NkTm^2 + \frac{1}{2}\eta\left(\frac{V - V_0}{V_0}\right)^2 + \frac{2\alpha}{r}\frac{V - V_0}{V_0} + \frac{1}{2}NkT\left[\ln\left(1 - \frac{m^2}{4}\right) + m\ln\frac{1+m}{1-m}\right]. \quad (66)$$

Here N is the number of atoms with the spin 1/2, $m = M/M_S$ is the relative magnetisation, η is volume compressibility and α is the surface tension. The equation includes four terms. The first term corresponds to the exchange energy density, the second term reflects the energy of cluster deformation, the third term corresponds to the surface energy and the fourth one is the entropy term responsible for the Langevin type of the temperature dependence of magnetisation.

To obtain the parameters of a stable magnetic state of the cluster, one should minimise the Gibbs free energy with respect to the change in the volume and magnetisation on the magnetic phase transition. Having solved the system of equations

$$\frac{\partial\Delta G}{\partial V} = 0,$$

$$\frac{\partial\Delta G}{\partial m} = 0, \quad (67)$$

which determine the equilibrium state of the system, one gets

$$\frac{T}{T_{C0}} = m\left(\frac{1}{3}\gamma m^2 + 1\right)\left(\frac{1}{2}\ln\frac{1+m}{1-m}\right)^{-1} \quad (68)$$

where $\gamma = (3/2)NkT_0\eta\beta^2/(1-\eta\beta P)$ and the Curie temperature, *viz.*, $T_{C0} = T_0(1-\eta\beta P)$, is lower than T_0 due to the pressure produced by the surface tension of the cluster.

The calculated changes in the relative magnetisation at different γ values are plotted *vs.* temperature in Fig. 41. The parameter γ determines the character of the magnetic phase transition. The case $\gamma < 1$ corresponds to the second-order magnetic phase transitions, whereas the case $\gamma \geqslant 1$ corresponds to the first-order magnetic phase transitions of clusters accompanied by abrupt loss of magnetic ordering. The Z-shaped portion of the magnetisation curve corresponds to an increase in the Gibbs free energy, *i.e.*, to unstable magnetic structures. The abrupt change in the magnetisation for an actually observed first-order magnetic phase transition is shown by dashed line.

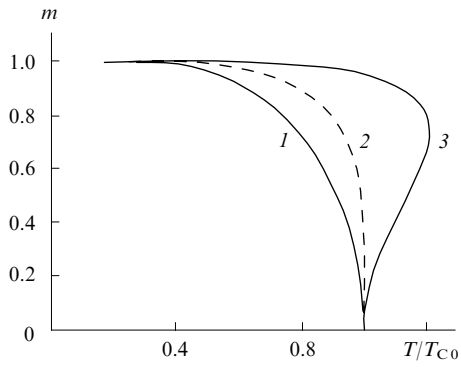


Figure 41. Relative cluster magnetisation plotted *vs.* temperature at different γ values.
$\gamma < 1$ (*1*), $\gamma = 1$ (*2*) and $\gamma > 1$ (*3*).

The critical cluster size corresponding to stepwise transition from the magnetically ordered to paramagnetic state can also be estimated from the γ value. For convenience, we will re-write the expression for γ as follows:

$$\gamma = \frac{T_{Cc}}{T_{C0}}, \tag{69}$$

where

$$T_{Cc} = \frac{3}{2} N k T_0^2 \eta \beta^2.$$

At $\gamma \geqslant 1$, clusters pass to the paramagnetic state upon a first-order magnetic phase transition if

$$r \leqslant r_{cr} = \frac{2\alpha\beta\eta}{1 - T_{Cc}/T_0}. \tag{70}$$

Large clusters ($r > r_{cr}$) will lose their magnetisation with an increase in temperature upon the second-order magnetic phase transitions.

To realise the first-order magnetic phase transitions, one should obtain clusters of substances that have a sufficiently high compressibility η. (Clusters with zero compressibility correspond to $r_{cr} = 0$ and second-order magnetic phase transitions.) The surface tension α is the key parameter that governs the occurrence or lack of the first-order magnetic phase transitions and variation of the critical cluster size [see Eqn (66)]. This model for phase transitions treats an isolated cluster characterised by the surface tension α at the cluster–vacuum interface. Any interaction between the cluster and the stabilising matrix or the neighbouring clusters leads to a decrease in α and r_{cr} and to disappearance of the first-order magnetic phase transitions. Therefore, studies of this type of phase transitions can serve as a tool for characterisation of intercluster and cluster–interface interactions.

In order to observe the first-order magnetic phase transitions, a nanosystem comprising ferrihydrite $Fe_5HO_8 \cdot 4\,H_2O$ nanoclusters formed in polysorb pores 13 to 75 nm in diameter was synthesised.[36, 105] This matrix-type nanosystem permits formation of isolated metal oxide clusters or accumulation of several clusters in the same pore. Polysorbs used were styrene and divinylbenzene copolymers without surface functional groups. The pore walls in such polysorbs have hydrophobic properties, which significantly weakens the interaction of ferrihydrite clusters with the matrix and leads to an increase in r_{cr}. Intercluster interactions and the number of clusters in the pore were changed by varying the concentration of iron atoms. To increase the sensitivity of Mössbauer spectrometers, experiments were carried out using ^{57}Fe-enriched iron-containing clusters synthesised in pores by soaking polysorbs with alcoholic solutions of $^{57}FeCl_3 \cdot 6\,H_2O$ with the iron concentrations of 1.2×10^{-2} and 1.2×10^{-3} mol litre^{-1} and subsequent treatment with air/gaseous ammonia mixture. An increase in the polysorb pore size from 13 to 75 nm was followed by an increase in the size of the clusters formed in the pores.

The Mössbauer spectra of ferrihydrite clusters in polysorb pores ($c = 1.2 \times 10^{-3}$ mol litre^{-1}) at different temperatures are shown in Fig. 42. At all temperatures, the spectra consist of a narrow-line magnetic HFS and a central doublet. As the temperature increases, the HFS is partially converted to the paramagnetic doublet without passing through the forms corresponding to superparamagnetic broadening and to line shift leading to a considerable decrease in the magnetic field at the core. The results obtained suggest that the first-order magnetic phase transitions occur in ferrihydrite clusters in the temperature range 4.2–6 K.

Analysis of the Mössbauer spectra [105] allows one to reveal the effects of the interactions between clusters and the pore wall and the intercluster interactions on the character of magnetic phase transitions. First of all it should be noted that the Mössbauer spectra of (i) synthetic and natural ferrihydrites of cluster size 2–5 nm (this corresponds to magnetically ordered structures) and (ii) ferrihydrite clusters formed in polysorb pores are different. The former group of spectra exhibits a magnetic HFS at 4.2 K and broad HFS components ($\sim$1.5–2 mm s^{-1}, see Ref. 108), while the latter group of spectra is characterised by much narrower lines

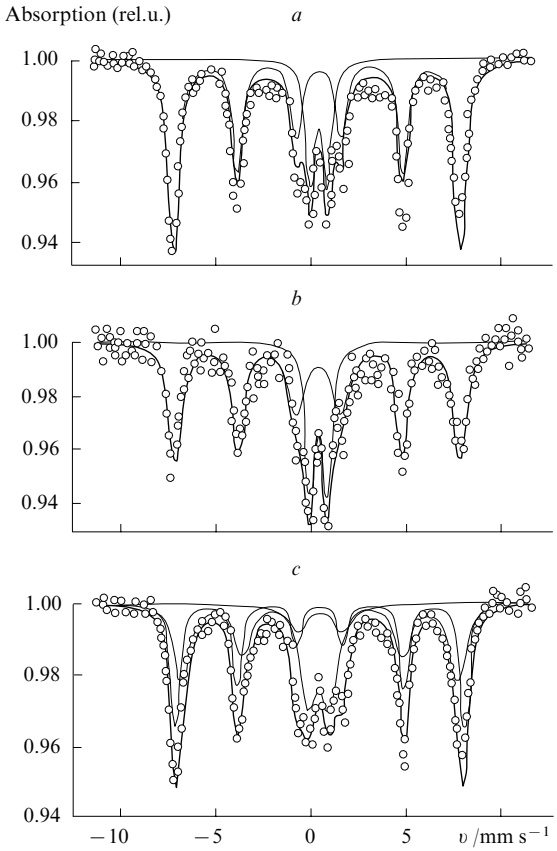


Figure 42. Mössbauer spectra of ferrihydrite clusters in polysorbs with pore sizes of 13 (*a*, *b*) and 20 nm (*c*).[105]
$c = 1.2 \times 10^{-3}$ mol litre^{-1} at 4.2 (*a*, *c*) and 10 K (*b*).

($\sim$0.6 mm s^{-1}). This difference is due to isolation of ferrihydrite clusters in copolymer pores and indicates weak intercluster and cluster–pore walls interactions compared to similar interactions in polycrystalline ferrihydrite. Indeed, the iron concentration of 1.2×10^{-3} mol litre^{-1} corresponds to nearly one 1–2-nm ferrihydrite cluster per pore of volume 10^{-22}–10^{-23} m^3 and here the magnetic properties of the cluster depend on the interaction between the cluster and the matrix surface. Thus, a first-order magnetic phase transition occurs at 4.2–6.0 K; clusters that are smaller than the critical cluster abruptly lose spontaneous magnetisation and go to the paramagnetic state.

As the temperature increases to 10 K, the relative proportion of the HFS in the Mössbauer spectrum decreases due to superparamagnetic relaxation. At a constant concentration of iron atoms ($c = 1.2 \times 10^{-2}$ mol litre^{-1}), an increase in the pore size to 20 nm is accompanied by an increase in the cluster size, which causes an increase in the proportion of the HFS (see Fig. 42 *c*), a decrease in the probability of the first-order magnetic phase transitions and strenthening of the interaction between clusters and the pore surface. A tenfold increase in the ^{57}Fe concentration at the same pore size is followed by nucleation of several clusters in the same pore (up to 5–8 clusters of size $\sim$ 2 nm), strengthening of intercluster interactions and, as a consequence, by the overall decrease in r_{cr} values corresponding to the first-order magnetic phase transitions.[105] Here, this makes it possible to estimate the size of ferrihydrite clusters involved in superparamagnetic relaxation. Using relation (29) and $\tau_0 = 1 \times 10^{-9}$ s, $\tau_{cr} \sim 189 \times 10^{-9}$ s, $T = 10$ K and $K = 1.7 \times 10^5$ J m^{-3}, the upper limit for clusters with iron concentration of 1.2×10^{-2} mol litre^{-1} was estimated at $\sim$ 2.2 nm.

Thus, these nanosystems permit observation of the first- and second-order (superparamagnetism) magnetic phase transitions

for clusters of size ~ 2 nm. The magnetic phase transitions were detected in the temperature range 4.2 – 6 K.

An increase in the pore size to 75 nm at an iron concentration of 1.2×10^{-2} mol litre^{-1} causes fundamental changes in the spectral pattern. This nanosystem shows the second-order magnetic phase transitions and clusters behave as superparamagnets. Calculations of superparamagnetic relaxation give an estimate $r \sim 2.5$ nm for both iron concentrations, because the average cluster size in the pore is determined by the average pore size. An increase in the iron concentration in a pore leads to multiple cluster formation, strengthening of intercluster interactions, a decrease in the critical cluster size and suppression of the first-order magnetic phase transitions.

It is interesting to compare the experimental estimates of r_{cr} obtained using the Mössbauer spectra, concentrations of the iron atoms in pores and relationships (68) – (70). Calculations for small clusters carried out assuming the critical first-order magnetic phase transition temperatures of $\sim 4.2 - 6$ K, the second-order magnetic phase transition temperature of $\sim 20 - 30$ K, the molar volume of 14.4×10^{-29} m^3, the inverse compressibility of $\sim 1.5 \times 10^{11}$ Pa, and the cluster surface tension of ~ 1 J m^{-2} led to $r_{cr} \sim 1$ nm, which is in agreement with the experimental estimates $r_{cr} \sim 1.5 - 2$ nm. Indications of the first-order magnetic phase transitions were observed for small clusters of other iron oxides (see, *e.g.*, Ref. 36), but this was not observed for metal clusters (Fe, Co, Ni), probably due to lower compressibility of these particles.

The pressure is an important factor determining the appearance or disappearance of the first-order magnetic phase transitions. According to the thermodynamic model for magnetic phase transitions of nanoclusters [see Eqns (68) – (70)], the critical transition temperature reduces as the external pressure increases:

$$T_{C0} = T_0(1 - \beta\eta P). \quad (71)$$

A simple method of producing an excess pressure in a confined volume is to freeze water. The volume of ice is 8% larger than the volume of water and can produce a pressure of up to a few GPa in pores of nanometre size. Investigations of the effects of hydration, freezing of nanostructures and the action of pressure on clusters upon freezing of water in nanopores involved two series of experiments with the systems including iron oxyhydroxide nanoclusters in pores of an ion-exchange resin (sulfo cation exchange resin) and in iron-accumulating protein (ferritin) in the dry and hydrated states.[109]

The major difference in the Mössbauer spectra of iron hydroxide clusters in the hydrated and dry samples manifests itself in the temperature range of 8.5 – 15 K. Comparison of the spectra of the dry samples of sulfo cation exchange resin containing iron oxyhydroxide clusters at 13 K and the spectra of the hydrated samples at 10 K showed that these spectra are identical, which suggests the temperature shift of the magnetic phase transition upon hydration. The transition is completely reversible. The spectrum of hydrated ferritin containing iron oxide core (similar to sulfo cation exchange resin) exhibits an increase in the proportion of the paramagnetic doublet compared to the spectrum of the dry sample. By comparing the spectra, it is possible to determine the magnitude of the temperature shift of the magnetic phase transition under pressure $\Delta T = 3 - 4$ K.

Nanostructures. The first-order magnetic phase transitions induced by intercluster stresses and defects can occur in nanosystems containing nanoclusters of size 20 – 50 nm. Such nanostructures are formed in solid-phase chemical reactions, *e.g.*, cluster sintering; they are characterised by rather strong intercluster interactions. A nanostructure including α-Fe_2O_3 and γ-Fe_2O_3 clusters exhibits not only the first- and second-order magnetic phase transitions, but also a weak ferromagnetic – antiferromagnetic phase transition and a novel type of magnetic phase transition, accompanied by the formation of twin nanostructures.[110]

The first-order magnetic phase transitions similar to the transitions in the 1 – 3-nm ferrihydrite clusters (see Ref. 105) were observed in the α-Fe_2O_3 – γ-Fe_2O_3 nanostructure formed in the initial stage of cluster sintering by the solid-phase chemical reaction.[110] The AFM images of this nanostructure are shown in Fig. 22.

First-order magnetic phase transitions. As mentioned above, Mössbauer spectroscopy is the most efficient method of investigation of the first-order magnetic phase transitions in clusters. The Mössbauer spectra of the α-Fe_2O_3 – γ-Fe_2O_3 nanostructure at different temperatures are shown in Fig. 23. As the temperature increases, the magnetic phase transitions from the ordered magnetic state to the paramagnetic (superparamagnetic) state of the nanostructure are observed, the former state being characterised by a magnetic HFS. At 77 K, the spectra exhibit two magnetic HFSs corresponding to α-Fe_2O_3 ($\Delta E_Q = -0.29$ mm s^{-1}) and γ-Fe_2O_3 ($\Delta E_Q = 0$ mm s^{-1}). Raising the temperature up to $T = 120$ K causes the appearance of a quadrupole doublet with $\Delta E_Q = 0.78$ mm s^{-1} and the isomer shift $\delta = 0.42$ mm s^{-1} relative to the metallic iron HFS, but the overall spectral pattern remains unchanged. Starting with $T = 120$ K, these spectra are transformed into spectra with one magnetic HFS ($\Delta E_Q = 0$ mm s^{-1}).

The Mössbauer spectra in the temperature range 120 – 300 K are characterised by reversible transformations of the magnetic HFS into a paramagnetic doublet without noticeable shift or broadening of the lines characteristic of the second-order magnetic phase transitions (or superparamagnetism). This is an indication of the first-order magnetic phase transitions (magnetisation of the nanomaterial disappears abruptly). These transitions occur at the critical temperatures $T_{C0} = 120 - 300$ K, which are lower than T_0 temperatures for bulk samples of α-Fe_2O_3 and γ-Fe_2O_3 (856 and 965 K, respectively). The lack of superparamagnetism for such large clusters becomes clear from the estimate using relation (29). Taking the magnetic anisotropy constant to be $K \approx 10^5$ J m^{-3} and $\tau_0 = 10^{-9} - 10^{-10}$ s, the relaxation time τ is several orders of magnitude longer than the measurement time (period of Larmor precession for ^{57}Fe nucleus is $\sim 10^{-8}$ s). Therefore, superparamagnetism has no effect on the magnetic properties of these nanostructures and cannot cause a reduction of T_{C0}.

In the nanostructures of α-Fe_2O_3 and γ-Fe_2O_3 the magnetisation and magnetic ordering disappear due to the first-order magnetic phase transition (abruptly), namely, the magnetic induction decreases from ~ 50 T to 0. It should be noted that the critical size, r_{cr}, of isolated ferrihydrite clusters is about 1.5 nm; smaller clusters undergo a stepwise transition to the paramagnetic state. There is also a narrow temperature range (4.2 – 10 K) characteristic of the first-order phase transitions. These effects were associated with the effect of surface tension.

For clusters of size 20 – 50 nm the pressure due to the surface tension should be an order of magnitude lower; additionally, a strong intercluster interaction causes α to decrease. Therefore, there also should be some other reasons for the first-order magnetic phase transitions and reduction of T_{C0} in this nanostructure (corresponding to $\gamma \geqslant 1$, see Ref. 105). Clearly, these reasons are associated with the influence of defects on the properties of the nanostructure [see Eqn (28)]. It is assumed that iron oxide clusters of size 20 – 50 nm provide a maximum defect density. For larger clusters, the effect of the surface as a source of defects is insignificant, whereas for smaller clusters the surface pressure is large enough to displace defects from the cluster. So, small clusters are defect-free.[111]

Following this model, there should exist a maximum defect density at which clusters of critical size (tens of nanometres) are formed in the nanosystem. If the cluster sizes are less than the critical size, first-order magnetic phase transitions occur in the nanosystem; otherwise, the second-order magnetic phase transitions characteristic of bulk materials occur.

The extremal character of the dependence of defect concentration on the cluster size [see Eqn (47)] also affects the temperature dependences of the magnetisation of a nanocluster structure comprising clusters of different size. One can assume a linear dependence of the critical temperature on the defect concentration in the cluster

$$T_C = T_{C0}(1 + \beta c_v), \tag{72}$$

where $\beta < 0$, c_v is the defect concentration in the cluster.

Taking into account the magnetic intercluster interaction, the thermodynamic potential of the nanosystem 'magnetic clusters – medium – defects' can be represented by the sum including the surface energy and the change in the chemical potential upon the change in the cluster size and in the defect density in the cluster,

$$G = \Delta\mu n_v + \alpha s n_v - 0.5\, N_v k T_{C0}(1 + \beta c_v)m^2 + \tag{73}$$

$$+ NkT\left(\frac{1}{2}\ln\frac{1-m^2}{4} + m\ln\frac{1+m}{1-m}\right),$$

where $\Delta\mu = \mu_0 + kT\ln(N_s n_v/N_v n_s)$ is the chemical potential difference between the defects inside the cluster and on the cluster surface; N_v is number of atoms in the cluster; N_s is number of atoms in the intercluster medium per cluster; n_v is number of defects in the cluster; n_s is number of defects in the intercluster medium per cluster; α is the surface tension of the cluster in the intercluster medium; s is cluster surface area; $m = M/M_0$ is the relative magnetisation of the cluster and N is the number of spins in the cluster. The temperature dependences of the relative magnetisation calculated for iron oxide nanoclusters of different size with energy minimisation are shown in Fig. 43.[111]

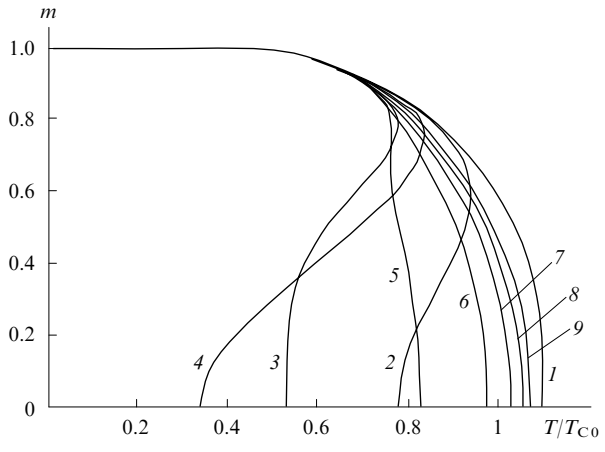


Figure 43. Relative magnetisation (m) of iron oxide plotted *vs.* T/T_{C0} at different r/a: 6 (*1*), 12 (*2*), 25 (*3*), 50 (*4*), 100 (*5*), 200 (*6*), 300 (*7*), 400 (*8*) and 500 (*9*).[111]

The temperature dependence of the magnetisation is consistent with the published data.[111] For the oxide clusters, it predicts the existence of a critical size of 30 – 40 nm, which corresponds to the maximum defect density in the cluster. If a cluster size is larger (smaller) than the critical size range indicated, the character of the magnetic phase transitions changes from the first-order to the second-order magnetic transitions.

Collective magnetic phase transitions with the formation of twin nanostructures. Now we will consider Fig. 23 in more detail. At low temperatures ($T < 120$ K), both phases, α-Fe_2O_3 and γ-Fe_2O_3 exist in the nanostructure. At temperatures above 120 K, in addition to a Morin transition (transition from antiferromagnetic to a weakly ferromagnetic structure; in bulk iron oxides occurs at 256 K, see Refs 104, 112) the α-Fe_2O_3 and γ-Fe_2O_3 phases undergo transformation into a common phase similar to the α-Fe_2O_3 phase in ΔE_Q, the structural symmetry of the α-Fe_2O_3 and γ-Fe_2O_3 phases being retained (according to X-ray analysis data). The temperature dependences of the isomer shift show an abrupt change δ at 120 K. As a result, δ for the α-phase decreases while that for the γ-phase increases jumpwise to an average value of 0.45 mm s^{-1}. These data also indicate collective transformations of the γ- and α-phases into an α-like phase with retention of cubic spinel symmetry. This transition can be explained by the formation of a twin structure. Twinning is known to occur upon crystallisation, mechanical deformation, seed sintering, fast thermal expansion or compression, and heating of deformed crystals.[113, 114]

Nanostructures formed under shear stress and high pressure. Exposure of bulk materials to shear stress under high pressure leads to nanostructuring and a decrease in the nanocrystallite size to 5 – 10 nm. Simultaneously, plastic deformation leads to generation of numerous defects that affect the magnetic properties of nanostructures, in particular, the character and critical parameters of magnetic phase transitions. When unloaded, nanocomposites comprising α-Fe_2O_3 and γ-Fe_2O_3 nanoclusters retain the stresses and defects; they are characterised by the first-order magnetic phase transitions and a decrease in T_{C0} due to an increase in the defect density. Nanostructuring of bulk samples should also induce shifts of the critical points and change the character of magnetic phase transitions from the first-order to the second order ones or *vice versa*.

Here we will consider magnetic phase transitions in two nanosystems based on the α-Fe_2O_3 and γ-Fe_2O_3 (I) and metallic europium (II) nanoclusters. The first nanosystem included α-Fe_2O_3 and γ-Fe_2O_3 nanoclusters of size 20 – 50 nm (I.1) and identical α-Fe_2O_3 and γ-Fe_2O_3 nanoclusters with addition of 50% monomeric acrylamide (I.2). The second nanosystem included metallic europium nanoparticles (II.1), metallic europium with addition of 1% of α-Fe_2O_3 and γ-Fe_2O_3 nanoclusters of size 20 – 50 nm (II.2) and metallic europium with addition of 10% of adamantane (II.3).[111, 115]

A high-pressure apparatus of Bridgeman anvil type allowed one to produce pressures of up to 5 GPa with the simultaneous accumulation of the total shear stress with an increment of 10° during 5 s. A pressure of 2 GPa was applied and the turn angles of the anvil varied from 120 to 240°.

Exposure of system (I.2) to shear stress under a pressure of up to 2 GPa causes polymerisation of acrylamide. The shear deformations in the unloaded polymer remain unchanged, which precludes recrystallisation of α-Fe_2O_3 and γ-Fe_2O_3 and recovery of the initial phase equilibrium. The action of shear stress under high pressure led to an increase in the proportion of the non-magnetic component in this system, but the most remarkable result was obtained for the nanosystem (II.2). The ^{57}Fe Mössbauer spectrum of nanostructure (II.2) at 300 K after shear stress under pressure (Fig. 44) exhibits almost complete loss of magnetic ordering in the α-Fe_2O_3 and γ-Fe_2O_3 clusters, which indicates a decrease in the average nanocrystallite size and reduction of the Curie or Néel temperatures below room temperature.

Mössbauer spectroscopy data for the nanosystems based on metallic europium show the reverse, namely, an increase in the transition temperature for europium.

The ^{151}Eu Mössbauer spectra of nanostructures (II.1), (II.2) and (II.3) at 90 K measured after exposure to shear stress under high pressure are shown in Fig. 45.

The spectrum of nanostructure (II.1) includes not only the metallic component corresponding to four lines in the HFS, but also the europium dioxide and europium oxide lines (Fig. 45 *a*). The spectrum of nanostructure (II.2) consists of three components, a broad line of metallic europium and the EuO and Eu_2O_3 lines (Fig. 45 *b*). The spectrum of nanostructure (II.3) exhibits three components corresponding to lines of the magnetic HFS of metallic europium in the magnetically ordered state, a very broad line of metallic europium and a line of EuO (Fig. 45 *c*).

Analysis of the experimental results suggests the following.

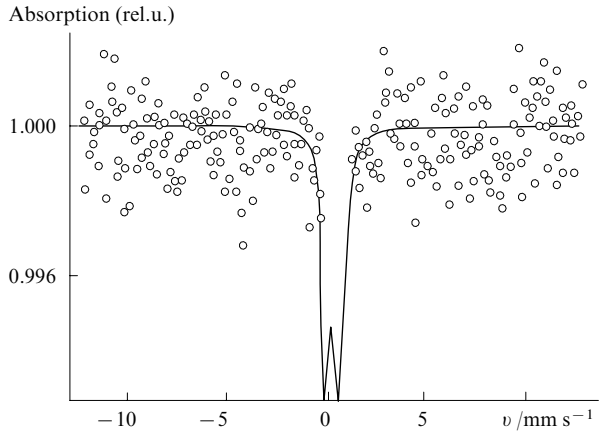


Figure 44. ^{57}Fe Mössbauer spectrum of nanostructure II.2 at room temperature upon a pressure with the turn of anvils.

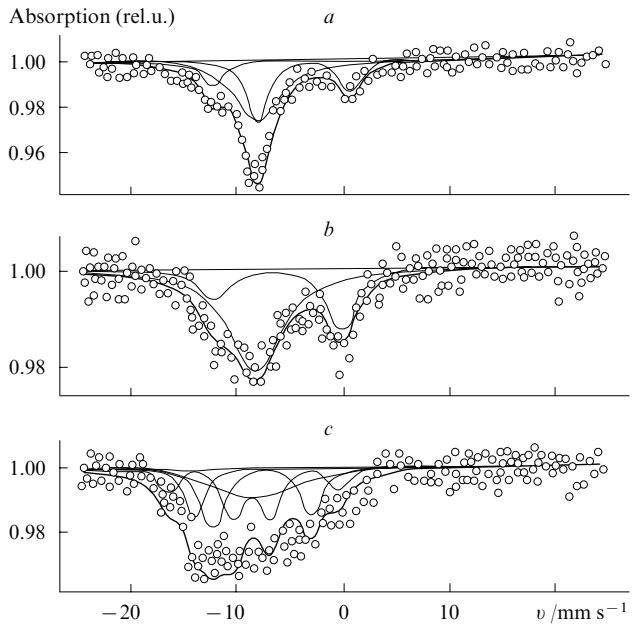


Figure 45. ^{151}Eu Mössbauer spectra of nanostructures II.1 (*a*), II.2 (*b*), and II.3 (*c*) at 90 K upon a pressure of 2 GPa with the turn angle of anvils of 120°.

1. The first-order magnetic phase transitions (jumpwise disappearance of the magnetisation of the nanostructure at certain critical temperature) are observed in nanostructures (I.1), (I.2), (II.2) subjected to shear stress under high pressure. As the measurement temperature increases from 77 to 300 K, the spectra of the nanosystems studied show a transition of iron oxide nanoclusters from the magnetic state characterised by a magnetic HFS to the paramagnetic state without line broadening and shift due to the existence of the critical cluster size.

2. The critical temperatures of magnetic phase transitions (T_C or T_N) in nanostructures (I.1), (I.2) and (II.2) are much lower than the magnetic phase transition temperatures of bulk samples. The critical temperatures decrease even more appreciably upon adding acrylamide or metallic europium.

3. In contrast to nanosystem (I.1), a characteristic feature of nanosystem (II.1) is the second-order magnetic phase transition. This follows from the fact that above the critical transition temperature ($\sim$80 K, see Ref. 116) the Mössbauer spectrum exhibits a superposition of the narrow line of non-magnetic europium and the broad line with unresolved magnetic HFS of the magnetically ordered europium. Thus, the magnetic phase transition temperature T_N of nanostructured europium is about 100 K higher than T_N of bulk metal.

4. Adding 1% of α-Fe_2O_3 and γ-Fe_2O_3 nanoclusters [nanosystem (II.2)] or 10% of adamantane [nanosystem (II.3)] to metallic europium causes further increase in T_N, especially pronounced for nanosystem (II.3).

These features are characteristic of the nanostructures comprised of relatively large nanoclusters in which the high density of defects formed upon exposure to shear stress under high pressure should retain. The results obtained make it possible to employ the defect density distribution in the nanostructure, which passes through a maximum at cluster sizes of 30–50 nm, for characterisation of the magnetic properties of these nanostructures. The critical defect densities should correspond to the critical cluster sizes upon the change in the character of the magnetic phase transition from the first-order to the second-order transition and *vice versa*.

A model for magnetic phase transitions in defect nanostructured systems[115] provides an explanation for all the effects considered above for the oxide and metallic nanosystems.

First-order magnetic phase transitions (Z-shaped curves) should be observed for iron oxide clusters of size 20–50 nm. At temperatures above T_C, the magnetisation of such clusters disappears jumpwise. The T_C value also depends on the size of the clusters present in the system. If the cluster size exceeds the maximum critical value ($> r_{cr}^{max}$), the second-order magnetic phase transition characteristic of bulk samples occurs and T_C increases. Reduction of the cluster size ($< r_{cr}^{min}$) also causes the second-order magnetic phase transitions to occur due to the decrease in the defect concentration.

The character of magnetic phase transitions and the T_C value are affected by the intercluster magnetic interactions. However, the changes in the intercluster distance affect the temperature dependence of magnetisation to a lesser extent compared to the changes in the cluster size. For instance, a maximum increase in T_C with a decrease in the intercluster distance from R to the lattice constant a is $\sim$6%.[115] This is accompanied by the change in the character of the magnetic phase transition from the first-order to the second-order one.

Nanostructuring of nanosystems (I.1) and (I.2) by exposure to shear stress under pressure leads to reduction of the average cluster size and the average interclster distance. For nanosystem (I.1), the effect of the decrease in the cluster size on T_C is counterbalanced by the effect of compaction, which causes strengthening of the magnetic intercluster interaction. Nanosystems (I.2) or (II.2) are characterised by reduction of T_C and an increase in the contribution of the first-order magnetic phase transition. This is particularly pronounced for nanostructure (II.2) in which the magnetic ordering in all iron oxide nanoclusters is destroyed at room temperature. Therefore, an increase in the intercluster distances leads to weakening of magnetic interactions, extension of the jumpwise magnetic phase transitions and an increase in the probability of the first-order magnetic phase transitions.

Exposure of nanosystem (II.1) to shear stress under pressure leads to nanostructuring of the material. At temperatures below T_N, the starting metal has a domain structure with a domain size of up to tens of nanometres.[104] Above T_N ($\sim$80 K), bulk metallic europium undergoes a first-order magnetic phase transition accompanied by sharp loss of magnetic ordering. The structure of metallic europium in the magnetically ordered state can be considered as consisting of nanocluster 'domains' packed in the crystal lattice of metallic europium. The size of these magnetic nanocluster 'domains' close to 20–30 nm provides the maximum defect density and, hence, the maximum density of strain, which induces the first-order magnetic phase transitions in metallic europium.

The aforesaid can be substantiated by high magnetostriction coefficients of rare-earth metals. The shear stress under pressure

causes a decrease in the size of the cluster 'domains' and they become smaller than the critical value. This leads to a decrease in the defect concentration and elimination of strain in the nanosystem. As a result, the first-order magnetic phase transition is destroyed and, as a consequence, the magnetically ordered state is extended to the region of higher temperatures. This leads to an increase in T_N of metallic europium. The addition of 1% of iron oxide clusters makes this effect more pronounced due to higher strain in the iron oxides (compared to metallic europium) responsible for the decrease in the size of the nanoclusters composing the nanostructure. The effect is more pronounced upon filling the europium matrix with adamantane molecular clusters, which retain the strain in the nanostructure after the pressure is removed. Additionally, it seems likely that the introduction of iron oxide clusters and adamantane molecules as additives favours uniform nanostructuring on exposure to shear stress under pressure. Thus, nanostructuring of substances can either decrease or increase the T_C (T_N) temperatures of nanomaterials.

* * *

Summing up, nanoclusters and nanostructures exhibit specific features related to their stability and structure, which can be treated as the onset of discreteness of matter on the nanolevel. This manifests itself in the formation of nanoclusters and nanostructures and in consideration of the mechanical, thermal, electrical, optical and magnetic properties. The discreteness is characterised by the 'magic' numbers of atoms and the critical sizes of nanoclusters, which are related to the stability and preferred formation of nanoparticles of particular sizes and to manifestation of certain specific properties of nanomaterials, *e.g.*, changes in the melting temperature, heat capacity, one-electron conductivity, onset of laser emission, appearance of the first-order magnetic phase transitions, *etc*.

This work has been written with the financial support from the Russian Foundation for Basic Research (Project No. 06-03-32006).

References

1. C N R Rao, A Muller, A K Cheetham (Eds) *The Chemistry of Nanomaterials. Properties and Applications* Vols 1, 2 (Weinheim: Wiley-VCH, 2004)
2. Ch P Pool Jr, F J Owens *Introduction to Nanotechnology* (Hoboken: Wiley, 2003)
3. A D Pomogailo, A S Rozenberg, I E Uflyand *Nanochastitsy Metallov v Polimerakh* (Nanoparticles of Metals in Polymers) (Moscow: Khimiya, 2000)
4. G B Sergeev *Nanokhimiya* (Nanochemistry) (Moscow: Moscow State University, 2003)
5. R A Andrievski, A V Ragulya *Nanostrukturnye Materialy* (Nanostructural Materials) (Moscow: Akademiya, 2005)
6. I P Suzdalev *Nanotekhnologiya. Fizikokhimiya Nanoklasterov, Nanostruktur i Nanomaterialov* (Nanotechnology. Physicochemistry of Nanoclusters, Nanostructures and Nanomaterials) (Moscow: KomKniga, 2005)
7. H Haberland, in *Clusters of Atoms and Molecules* Vol. 1 (Ed. H Haberland) (Berlin, Heidelberg: Springer, 1994) p. 213
8. A W Adams *Physical Chemistry of Surface* (New York: Wiley, 1976)
9. C Brechignac, in *Clusters of Atoms and Molecules* Vol. 1 (Ed. H Haberland) (Berlin, Heidelberg: Springer, 1994) p. 255
10. W Ekardt *Phys. Rev. B* **29** 1558 (1984)
11. W D Knight, K Clemenger, N A de Heer,W A Saunders, M Y Chou, M L Cohen *Phys. Rev. Lett.* **52** 2141 (1984)
12. O Echt, in *Physics and Chemistry of Small Clusters* (Eds P Jena, B K Rao, S N Khanna) (New York: Plenum, 1987) p. 623
13. K E Schriver, J L Persson, E C Honea, R L Whetten *Phys. Rev. Lett.* **64** 2539 (1990)
14. M F Jarrold, in *Clusters of Atoms and Molecules* Vol. 1 (Ed. H Haberland) (Berlin, Heidelberg: Springer, 1994) p. 288
15. K Rademann, B Kaiser, U Even, F Hensel *Phys. Rev. Lett.* **59** 2319 (1987)
16. G M Pastor, J Dorantes-Davila, K H Bennemann *Chem. Phys. Lett.* **148** 459 (1988)
17. E E B Cambell, in *Clusters of Atoms and Molecules* Vol. 1 (Ed. H Haberland) (Berlin, Heidelberg: Springer, 1994) p. 331
18. E Dornenburg, H Hinterberger *Z. Naturforsch. A* **4** 765 (1950)
19. N Furstenau, F Hillenkamp *Int. J. Mass Spectrom. Ion Processes.* **37** 135 (1981)
20. S W McElvany, B I Dunlap, A O'Keefe *J. Chem. Phys.* **86** 715 (1989)
21. I Plesser, Z Vagar, R Naaman *Phys. Rev. Lett.* **56** 1559 (1986)
22. J Bernholc, J C Phillips *J. Chem. Phys.* **85** 3258 (1986)
23. S Yang, K J Taylor, M J Craycraft, J Conceicao, C L Pettiette, O Chesnovsky, R E Smalley *Chem. Phys. Lett.* **144** 431 (1988)
24. G E Scuseria *Science* **271** 942 (1996)
25. T Guo, R E Smalley, G E Scuseria *J. Chem. Phys.* **99** 352 (1993)
26. H W Kroto, J R Heath, S C O'Brien, R F Curl, R E Smalley *Nature (London)* **318** 162 (1985)
27. H W Kroto *Science* **242** 1139 (1988)
28. W R Creasy *J. Chem. Phys.* **92** 7223 (1990)
29. W Kratschmer, L D Lamb, K Fostiropoulus, D R Huffman *Nature (London)* **318** 354 (1990)
30. G Ulmer, E E B Campbell, R Khunle, H G Busman, I V Hertel *Chem. Phys. Lett.* **182** 114 (1991)
31. P P Radi, M T Hsu, J Brodbelt-Lustig, M Rincon, M T Bower *J. Chem. Phys.* **92** 4817 (1990)
32. E E B Campbell, G Ulmer, H G Busman, I V Hertel *Chem. Phys. Lett.* **175** 505 (1990)
33. S C O'Brien, J R Heath, R F Curl, R E Smalley *J. Chem. Phys.* **88** 220 (1988)
34. O V Boltalina, I N Ioffe, L N Sidorov, G Seifert, K Veitze *J. Am. Chem. Soc.* **122** 9745 (2000)
35. J A Barker *Rare Gas Solids* Vol. 1 (London: Academic Press, 1977)
36. I P Suzdalev, P I Suzdalev *Usp. Khim.* **70** 203 (2001) [*Russ. Chem. Rev.* **70** 177 (2001)]
37. B D Summ, N I Ivanova *Usp. Khim.* **69** 995 (2000) [*Russ. Chem. Rev.* **69** 911 (2000)]
38. A I Rusanov *Mitselloobrazovanie v Vodnykh Rastvorakh Poverkhnostno-aktivnykh Veshchestv* (Micelle Formation in Aqueous Solution of Surfactants) (St Petersburg: Khimiya, 1992)
39. R L Whetten, J T Khoury, M M Alvarez, S Murthy, I Vezmar, Z L Wang, P W Stephens, C L Cleveland, W D Luedtke, U Landman *Adv. Mater.* **8** 428 (1996)
40. C Petit, M P Pileni *J. Phys. Chem.* **92** 2282 (1988)
41. M P Pileni, T Gulik-Krzywicki, J Tanori, A Filankembo, J C Dedjeu *Langmuir* **14** 7359 (1998)
42. V V Hardikar, E Matijevic *J. Colloid Interface Sci.* **221** 133 (2000)
43. S Ramakrishnan, in *The Chemistry of Nanomaterials. Properties and Applications* Vol. 2 (Eds C N Rao, A Muller, A K Cheetham) (Weinheim: Wiley-VCH, 2004) p. 494
44. I F Efremov *Periodicheskie Struktury* (Periodical Structures) (Leningrad: Khimiya, 1971)
45. L Motte, F Billondet, E Lacaze, J Douin, M P Pileni *J. Phys. Chem. B* **101** 138 (1997)
46. J S Beck, J C Vartuli, W J Roth, M E Leonbovitcz, C T Cresge, K D Shmitt, C T W Chu, D H Olson, E W Sheppard, S B McCullen, J B Higgins, J L Shlenker *J. Am. Chem. Soc.* **114** 10834 (1992)
47. Y Wei, D L Jin, T Z Ding, W H Shih, X H Liu, S Z D Cheng, Q Fu *Adv. Mater.* **10** 313 (1998)
48. A K Raychaudhuri, in *The Chemistry of Nanomaterials. Properties and Applications* Vol. 2 (Eds C N Rao, A Muller, A K Cheetham) (Weinheim: Wiley-VCH, 2004) p. 693
49. F Keller, M S Hunter, D L Robinson *J. Electrochem. Soc.* **100** 411 (1953)
50. K C C Kharas, L F Dahl, in *Evolution of Size Effects in Chemical Dynamics* (Eds I Prigogin, S A Rice) (New York: Wiley, 1988)
51. P Chini *J. Organomet. Chem.* **200** 1985 (1980)
52. B K Teo, N J A Sloan *Inorg. Chem.* **24** 4545 (1985)

53. M N Vargaftik, N Yu Kozitsina, N V Cherkashina, R I Rudyi, D I Kochubei, B N Novgorodov, I I Moiseev *Kinet. Katal.* **39** 806 (1998) [a]
54. A Müller, S Roy *Usp. Khim.* **71** 1107 (2002) [*Russ. Chem. Rev.* **71** 981 (2002)]
55. S S Talismanov, I L Eremenko *Usp. Khim.* **72** 627 (2003) [*Russ. Chem. Rev.* **72** 555 (2003)]
56. A Müller, P Kogerler *Coord. Chem. Rev.* **182** 3 (1999)
57. A Müller, E Beckmann, H Bogge, M Schmidtmann, A Dress *Angew. Chem., Int. Ed.* **41**1162 (2002)
58. A Müller, H Reuter, S Dillinger *Angew. Chem., Int. Ed. Engl.* **34** 2328 (1995)
59. Yu D Tretyakov *Usp. Khim.* **72** 731 (2003) [*Russ. Chem. Rev.* **72** 651 (2003)]
60. Ya G Geguzin *Fizika Spekaniya* (The Physics of Sintering) (Moscow: Nauka, 1984)
61. W D Kingery, H K Bowen, D R Ulmann, in *Introduction to Ceramics* (New York: Wiley, 1976) p. 183
62. B F Ormont *Dokl. Akad. Nauk SSSR* **124** 132 (1959) [b]
63. I R Grigor'ev, U S Meilikhov (Eds) *Fizicheskie Velichiny. Spravochnik* (Physical Values. Handbook) (Moscow: Energoatomizdat, 1991)
64. I P Suzdalev, A M Afanas'ev, A S Plachinda, V I Gol'danskii, E F Makarov *Zh. Eksp. Teor. Fiz.* **55** 1752 (1974) [c]
65. I P Suzdalev, I V Kurinov, E Yu Tsymbal, V V Matveev *J. Phys. Chem. Sol.* **55** 127 (1994)
66. J M D Coey, D Khalafalla *Phys. Status Solidi A* **11** 2290 (1972)
67. I P Suzdalev, V N Buravtsev, A V Volynskaya, Yu V Maksimov, V V Matveev, V K Imshennik, S V Novichikhin *Khim. Fiz.* **14** 114 (1995) [d]
68. I P Suzdalev, N I Shklovskaya *Colloids Surf., A* **108** 315 (1996)
69. Ph Buffat, J P Borel *Rhys. Rev., Sect A* **13** 22 (1976)
70. Y Osima, K Takaynagi *Z. Phys. D: At., Mol. Clusters* **27** 287 (1993)
71. A N Goldstain, C M Echer, A P Alivisatos *Science* **256** 1425 (1992)
72. S Gartenhaus, C Schwartz *Phys. Rev.* **108** 482 (1957)
73. R S Berry, in *Clusters of Atoms and Molecules* Vol. 1 (Ed. H Haberland) (Berlin, Heiderberg: Springer, 1994) p. 187
74. S Bosiger, S Leutwyler *Phys. Rev. Lett.* **59** 1895 (1987)
75. I P Suzdalev, V N Buravtsev, Yu V Maksimov *Izv. Akad. Nauk, Ser. Fiz.* **67** 1025 (2003) [e]
76. H E Schaefer, R Wurschum, R Birringer, H Gleiter *Mater. Sci.* **15**–**18** 955 (1987)
77. Yu V Maksimov, I P Suzdalev, M Ya Kushnerev, R A Arents *Fiz. Met. Metalloved.* **37** 267 (1974) [f]
78. E O Hall *Proc. Phys. Soc. London* **174** 25 (1951)
79. N J Petch *J. Iron Steel Inst.* **174** 25 (1953)
80. R L Coble *J. Appl. Phys.* **34** 1679 (1963)
81. R W Siegel, G E Fougere *Nanosrtuct. Mater.* **6** 205 (1995)
82. O D Sherby, O A Ruano, in *Superplastic Forming of Structural Alloys* (Eds C E Patton, C H Hamilton) (New York: The Metall. Soc. of AIME, 1982) p. 241
83. G Schmid *J. Chem. Soc., Dalton Trans.* 1077 (1998)
84. C Martin *Science* **266** 1466 (1994)
85. G Hornyak, M Kroll, R Pugin, G Sawitowski, G Schmidt, J O Bovin, G Karsson, H Hoffmeister, S Hopfe *Chem.–Eur. J.* **3** 1951 (1997)
86. G Mie *Ann. Phys.* **25** 377 (1908)
87. U Kreibig, M Vollmer *Optical Properties of Metal Clusters* (Berlin: Springer, 1995)
88. K P Charle, W Schulze, in *Clusters of Atoms and Molecules* Vol. 2 (Ed. H Haberland) (Berlin: Springer, 1994) p. 263
89. M V Artemyev, U Woggon, H Jaschinski *J. Phys. Chem. B* **104** 11617 (1999)
90. V L Colvin, M C Schlamp, A P Alivisatos *Nature (London)* **370** 354 (1994)
91. S Hotchandani, I Bedja, R W Fessenden, P V Kamat *Langmuir* **10** 17 (1994)
92. A P Alivisatos *Science* **271** 933 (1996)
93. J M Schmelzer, J M Buriak, in *The Chemistry of Nanomaterials. Properties and Applications* Vol. 2 (Eds C N R Rao, A Muller, A K Cheetham) (Weinheim: Wiley-VCH, 2004) p. 523
94. F V Mikulec, J D Kirtland, M J Sailor *Adv. Mater.* **14** 38 (2002)
95. D Kovalev, V Y Timoshenko, N Künzner *Phys. Rev. Lett.* **87** 068301 (2001)
96. J D Joannopoulos, P R Villeneuve, S Fan *Nature (London)* **386** 143 (1997)
97. K Busch, S John *Phys. Rev.* **58** 3896 (1998)
98. Yu A Vlasov, X Zh Bo, J C Sturm, D J Norris *Nature (London)* **414** 289 (2001)
99. C L Chien *Annu. Rev. Mat. Sci.* **25** 129 (1995)
100. S Jin, T H Tiefel, M McCormack, R A Fastnacht, R Ramesh, R Chen *Science* **264** 413 (1994)
101. M Pissas, G Kallias, E Devlin, A Simopoulos, D Niarchos *J. Appl. Phys.* **81** 5770 (1997)
102. J W Lynn, R W Erwin, J A Borchers, Q Huang, A Santoro, J L Peng, Z Y Li *Phys. Rev. Lett.* **76** 4046 (1996)
103. L Thomas, F Lionti, R Ballou, D Gatteschi, R Sessoli, B Barbara *Nature (London)* **383** 145 (1996)
104. S V Vonsovskii *Magnetizm* (Magnetism) (Moscow: Nauka, 1971)
105. I P Suzdalev, V N Buravtsev, V K Imshennik, Yu V Maksimov, V V Matveev, S V Novichikhin, A X Trautwein, H Winkler *Z. Phys. D; At., Mol. Clusters* **37** 55 (1996)
106. I P Suzdalev, A Kh Trautvain *Khim. Fiz.* **15** 96 (1996) [d]
107. C B Bean, D S Rodbell *Phys. Rev.* **126** 104 (1962)
108. E Murad, J H Johnston *Modern Inorganic Chemistry. Mössbauer Spectroscopy Applied to Inorganic Chemistry* Vol. 2 (New York: Plenum Press, 1987)
109. I P Suzdalev, A S Plachinda, V N Buravtsev, Yu V Maksimov, S I Reiman, V I Khromov, D A Dmitriev *Khim. Fiz.* **17** 104 (1998) [d]
110. I P Suzdalev, Yu V Maksimov, S V Novichikhin, V N Buravtsev, V K Imshennik, V V Matveev *Khim. Fiz.* **19** 105 (2000) [d]
111. I P Suzdalev, V N Buravtsev, Yu V Maksimov, A A Zharov, V K Imshennik, S V Novichikhin, V V Matveev *Izv. Akad. Nauk, Ser. Khim.* 1848 (2003) [g]
112. I E Dzyaloshinskii *Zh. Eksp. Teor. Fiz.* **33** 1454 (1957) [c]
113. G Schulze *Metallphysic* (Berlin: Akademie-Verlag, 1967)
114. J P Hirth, J Lothe *Theory of Dislocations* (New York: McGraw-Hill, 1968)
115. I P Suzdalev, V N Buravtsev, Yu V Maksimov, A A Zharov, V K Imshennik, S V Novichikhin, V V Matveev *J. Nanopart. Res.* **5** 485 (2003)
116. K Taylor, M Darby *Physics of Rare Earth Solids* (London: Chapman and Hall, 1972)

[a] — *Kinet. Catal. (Engl. Transl.)*
[b] — *Dokl. Chem. (Engl. Transl.)*
[c] — *J. Exp. Theor. Phys. (Engl. Transl.)*
[d] — *Chem. Phys. Rep. (Engl. Transl.)*
[e] — *Bull. Russ. Acad. Sci., Phys. (Engl. Transl.)*
[f] — *Phys. Met. Metallogr. (Engl. Transl.)*
[g] — *Russ. Chem. Bull., Int. Ed. (Engl. Transl.)*